NASA Contractor Report 163094

FLOW VISUALIZATION STUDY OF THE HiMAT RPRV

Dale J. Lorincz

July 1980

NASA

NASA Contractor Report 163094

FLOW VISUALIZATION STUDY OF THE HiMAT RPRV

Dale J. Lorincz
Northrop Corporation
Hawthorne, California

Prepared for
Dryden Flight Research Center

National Aeronautics and
Space Administration
1980

CONTENTS

FLOW VISUALIZATION STUDY OF THE HiMAT RPRV

Dale J. Lorincz
Northrop Corporation, Aircraft Division
Hawthorne, California

SUMMARY

Water tunnel studies have been performed to qualitatively define the flow field of the HiMAT RPRV. Particular emphasis was placed on defining the vortex flows generated at high angles of attack. The flow visualization tests were conducted in the Northrop water tunnel using a 1/15-scale model of the HiMAT RPRV. Flow visualization photographs were obtained over an angle of attack range of from 5° to 40° at sideslip angles of 0° and 5°.

The HiMAT model was investigated in detail to determine the vortex flow field development, vortex path, and vortex breakdown characteristics as a function of angle of attack and sideslip. Vortex flows were found to develop on the canard, on the wing, and on the upper surface of the forebody. The mapping of the wing vortex flow determined the changes that occurred in the wing leading-edge vortex when the canard was added. The presence of the canard caused the wing vortex to form further outboard and delayed the breakdown of the wing vortex to higher angles of attack. An increase in leading-edge camber for the maneuver configuration delayed the formation and the breakdown of the wing and canard vortices. In sideslip, the canard increased the lateral stability, seen in wind tunnel data, at the higher angles of attack by delaying the stall on the windward side.

Additional tests were performed to determine the sensitivity of the canard vortex flow field to variations in inlet mass flow ratio and canard flap deflection angle. When the inlets were blocked completely, the flow angle at the canard apex was increased causing the canard vortex to form and burst sooner. An upward deflection of the canard flap forced an early breakdown of the canard vortex.

Asymmetries in the vortex system generated by the forebody were observed in the water tunnel at zero sideslip and high angles of attack. The orientation of the forebody vortex system in sideslip was found to influence the directional stability of the HiMAT at the higher angles of attack. The addition of the canards reduced the destabilizing influence of the forebody vortices in sideslip. A nose boom was added to the forebody and was found to reduce the angle of onset of vortex asymmetry. The turbulent wake shed from the nose boom was seen to disturb the orientation and structure of the forebody vortices.

INTRODUCTION

The remotely piloted research vehicles (RPRV) which were developed under the highly maneuverable aircraft technology (HiMAT) program have recently begun flight testing at NASA's Dryden Flight Research Center. The HiMAT RPRV incorporates several high-maneuverability technologies into a single design to achieve high transonic maneuverability. These technologies include close-coupled canards, winglets, a variable camber system, and relaxed static stability (References 1 and 2). The use of a canard in close proximity to a wing has been found to provide several benefits for increased maneuver performance. The canard-induced downwash on the wing can delay separation at moderate angles of attack and thereby reduce the camber and twist that is required to maintain attached flow on the wing. At higher angles of attack, a favorable interaction occurs for the close-coupled canard-wing which results in increased vortex lift (References 3,4, and 5). The potential of a canard configuration to increase trimmed lift and reduce trimmed drag has also been investigated. A leading-edge variable camber system was used on the HiMAT to minimize the drag due to lift over a wide range of angles of attack. The favorable interference between the canard and the wing of the HiMAT and the effects of the variable leading-edge camber have been studied in wind tunnel force tests and by theoretical analysis. A more complete understanding of the flow fields on the canards, the wing and the fuselage forebody of the HiMAT and how they affect its aerodynamic characteristics can be obtained through flow visualization.

Studies done at Northrop using a water tunnel have provided excellent visualization of vortex flows on wings and fuselage forebodies. The water tunnel has been used to qualitatively define the vortex flow fields on many aircraft

configurations. All testing for this study was done in the Northrop diagnostic water tunnel which has a test section of 0.41 by 0.61 meters (16 x 24 in.). Changes in angle of attack, sideslip, and model configuration can be made quickly and inexpensively using small scale models. The flow visualization results discussed in this report were obtained using a 1/15-scale model of the HiMAT RPRV. The angle of attack was varied from 5° to 40° at sideslip angles of 0° and 5°.

The primary purpose of these tests was to define the vortex flow fields generated above the wing, the canard, and on the forebody. The changes in the vortex flows with changes in angle of attack and sideslip were determined. The flow visualization studies included tests with both the cruise and the maneuver leading-edge camber on the wing and canard, and with the canard removed. The effect of the nose boom on the forebody vortex pair was investigated. The inlet mass flow rate was varied to determine the sensitivity of the vortex flows to this change. Wherever possible, the water tunnel results are compared to wind tunnel data from the Rockwell NAAL low-speed wind tunnel on a 0.22-scale HiMAT model.

SYMBOLS

b	wing span
$\bar{c}$	wing mean aerodynamic chord
C_L	lift coefficient
C_ℓ	rolling moment coefficient
C_{ℓ_β}	lateral stability parameter, $\frac{\partial C_\ell}{\partial \beta}$
C_m	pitching moment coefficient
C_{m_α}	pitching moment due to angle of attack, $\frac{\partial C_m}{\partial \alpha}$
C_n	yawing moment coefficient
C_{n_β}	directional stability parameter, $\frac{\partial C_n}{\partial \beta}$
C_Y	side force coefficient
C_{Y_β}	side force due to sideslip, $\frac{\partial C_Y}{\partial \beta}$
FS	fuselage station
M	Mach number
$\dot{m}_I$	mass flow to inlet

$\dot{m}_\infty$ capture mass flow

α angle of attack

β angle of sideslip

δ_f canard trailing-edge flap deflection

Λ_{LE} leading-edge sweep angle

EXPERIMENTAL METHODS

Water Tunnel Facility

The Northrop water tunnel is a closed return tunnel used for high quality flow visualization of complex three-dimensional flow fields. The water tunnel is shown schematically in Figure 1. The test section is 0.41 m (16 in.) by 0.61 m (24 in.) by 1.83 m (6 ft.) long and has walls made of transparent plexiglass. The test section is oriented in the vertical direction, which facilitates viewing the model from any angle. A model is shown installed in the test section in Figure 2. The model is accessed through the top of the tunnel by means of suspension cables connected to the model support system.

The model support system consists of a sting and sideslip arc which is capable of pitch angles from -10° to 70°, concurrent with a sideslip range of -20° to 20°. The sideslip angle is fixed prior to the model installation. The pitch angle is then manually adjusted from the side of the test section.

Test Procedure

The flow visualization in the water tunnel is obtained by injection of colored food dyes having the same density as water. The density of water is 800 times that of air, which gives the dye excellent light reflecting characteristics relative to using smoke in air. The dye is introduced into the flow field through small orifices and dye tubes distributed along the body of the model. The dye can also be introduced through a dye probe which can be accurately positioned at any point in the test section, by means of a traversing mechanism.

Inlet flows are simulated in the water tunnel by applying suction to a tube connected to the rear of the model's exhaust nozzle. The tube is run to a water flow meter outside the tunnel. The flow meter is used to accurately measure and set an inlet flow rate.

The water tunnel is operated at a test section velocity of 0.1 meters/second which has been found to produce the best flow visualization results. This velocity corresponds to a Reynolds number of 1×10^5/meter.

VORTEX FLOW FIELDS

Prior to development of the Northrop water tunnel, the question of whether vortex flow fields in air could be properly simulated in water with sufficient accuracy was considered. It is well known that if cavitation is avoided and compressibility effects are negligible, then the fluid motions of water and air at the same Reynolds number are dynamically similar. For the identical model scale and velocity, the Reynolds number in the water tunnel would be higher by a factor of 15 over that in air. However, because of practical limitations in speed and model scale, water tunnel tests are generally run at Reynolds' numbers well below those of wind tunnels.

For thin, swept wings, boundary layer separation occurs along the sharp leading edge. The sheet of distributed vorticity that is shed rolls up into a spiral vortex with a concentrated core. A laminar separation will occur at the sharp leading edge of the wing at the Reynolds numbers that are encountered in flight and in the water tunnel. The vortex generation is therefore not sensitive to Reynolds number and the vortex formed in the water tunnel is representative of flight (References 6, 7, and 8).

Once the leading-edge vortex flow has formed, its stability can be affected by external conditions. At high angle of attack, the vortex core can undergo a sudden expansion, which is referred to as vortex breakdown or burst. Above the stalled portion of a wing and at the wing trailing edge, there is a large adverse pressure gradient. This negative velocity gradient will reduce the axial velocity within the core of the vortex. The vortex will then burst with a rapid expansion to a larger, slower

rotating flow. The breakdown of the vortex core depends on the magnitude of the rotational and axial velocities, the external pressure gradient, and degree of flow divergence. The external pressure gradient is felt to be the dominant parameter. Therefore, when a leading-edge vortex encounters a large enough adverse pressure gradient above a wing it will break down in a similar manner in the water tunnel as in the wind tunnel and in flight.

The rolled-up vortex sheet induces large suction pressures on the upper surface of the wing which produce additional lift. An increase in the rotational velocity of the vortex will induce lower pressures on the surface and increase the vortex lift. At the same time, an increase in rotational velocity decreases the stability of the vortex, making it more likely to burst. A moderate increase in the axial velocity of a vortex will increase the stability of the vortex and delay any breakdown.

The vortex burst locations above the upper surface of thin, swept wings in the water tunnel are in good agreement with the results at higher Reynolds numbers in wind tunnels and in flight at moderate to high angles of attack because the external pressure gradient is the dominant effect. Surface flows at low angles of attack that are not yet vortex dominated can be more sensitive to Reynolds number effects. Early laminar separation in the water tunnel on leading-edge flaps can result in a smaller delay of vortex breakdown compared to wind tunnel results.

The asymmetric shedding of the vortex pair which forms on an aircraft forebody at zero sideslip and high angles of attack is associated in part with an inviscid hydrodynamic instability. The water tunnel studies generally show a slightly higher angle of onset of the forebody vortex asymmetry then do wind tunnel measurements of the asymmetric side force. The orientation of the forebody vortex system in sideslip has been found to correspond with the directional stability characteristics at high angles of attack of several fighter configurations. A side force is produced toward the forebody vortex which remains closest to the surface in sideslip.

MODEL DESCRIPTION

The water tunnel flow visualization studies were conducted with a 1/15-scale model of the HIMAT RPRV. A three-view drawing of the model is shown in Figure 3. The model was built by NASA Langley and loaned to Northrop for use during the water tunnel tests. The canard had a leading-edge sweep of 55° and dihedral of 20°. The inboard portion of the wing had a leading-edge sweep of 53°. Outboard of the wing mid-semispan the leading-edge sweep was reduced to 45°. The model configuration tested was with the landing gear up and all control surfaces on the wing and vertical tails at zero deflection. The canard was fitted with a trailing-edge flap that could be deflected from 0° to -20° trailing-edge up.

The model was built with a flow-through duct from the inlet to the exhaust nozzle. To provide the desired inlet mass flow rate, a suction tube was connected to the metal tube which extended aft from the nozzle exit. The metal tube also served as the sting to support the model in the tunnel. The inlet mass flow ratio was set to simulate the inlet conditions at a freestream Mach number of 0.4. This mass flow ratio at zero angle of attack is $\dot{m}_I/\dot{m}_\infty = 1.21$. The mass flow is pulled in from an area larger than the capture area of the inlet.

A mechanical deflection of the leading edge would be employed on a full-scale fighter to provide continuously variable leading-edge camber. On the water tunnel model, interchangeable leading edges where used on the wing to make the deflection of the leading edge from the cruise to the maneuver configuration. The model was fitted with two different sets of canards to permit a change in the leading-edge camber of the canard from the cruise to the maneuver configuration. No changes to the wing or the canard, other than the leading edge deflection to increase camber, were made for the maneuver configuration. Under maneuver conditions in flight, the aeroelastic tailoring of the wing and canard allow them to assume a spanwise twist variation which produces additional twist (washout) at the tip. The wing and canard on the water tunnel model do not have this additional structural twist and retain the cruise twist distribution.

In order to visualize the flow field, the model was equipped with dye injection orifices. Great care was taken in locating the dye orifices to insure that dye introduced into the external flow would be entrained into the vortices. A traversing dye probe was used to survey the model to find the exact location for each orifice. On the forebody, the orifices were distributed along the windward side and were installed flush with the surface. For the vortex flows of the wings and canards, dye tubes were run externally on the underside of the surface to a point just aft and outboard of the apex.

A grid was laid out on the wings and canards of the model to aid in documenting the path of the vortices and for measuring the location of the vortex breakdown. The grid begins at fuselage station 50 for the full-scale RPRV, which is just aft of the apex of the canard. The grid has divisions of 25.4 cm (10 in.) full scale or 1.69 cm (0.67 in.) apart on the model. Lines were drawn in the chordwise direction at mid-semispan of the canard and at mid-semispan of the wing.

RESULTS AND DISCUSSION

The experimental results that were obtained from the water tunnel flow visualization studies consist of a set of photographs documenting the flow field of the HiMAT RPRV. Selected results are referred to in the text and are given at the end of this report. Comparisons are made of the progression of the vortex burst point for the various configurations of the canard and wing that were tested. Whenever possible, comparisons are made between the water tunnel flow visualization results and the force and moment data obtained in the Rockwell NAAL low-speed wind tunnel using a 0.22-scale model.

Cruise Wing-Canard Flow Field

The flow field of the wing and the canard in the cruise configuration at zero sideslip is presented in Figure 4. The dye orifices at the leading edges of the wing and the canard are located such that the dye from them would be entrained into the vortices. At 10° angle of attack, however, the flow is attached on the upper surfaces. The dye being ejected at the apex of the wing and the canard

is within the boundary layer. Figure 4 shows that there is some spanwise spreading of the surface flow, especially on the wing.

A vortex begins to form on the wing at 12° angle of attack. The wing vortex is rather weak and diffuse and can be seen in Figure 4 to lie outboard of the mid-semispan line. A diffuse vortex is also beginning to form above the upper surface of the canard. The flow is separated along the leading edge of the canard, beginning outboard of mid-semispan of the canard. The canard vortex is difficult to detect in the dye because it is weak at this angle of attack.

With an increase in angle of attack to 15°, a well defined wing and canard vortex are formed as shown in Figure 4. The flow is now separated all along the leading edge of the canard and rolls up into a concentrated vortex. A weak secondary vortex has formed between the canard leading edge and the core of the leading-edge vortex. Inboard and downstream of the leading-edge vortex there is a flow reattachment. In Figure 4, at 15° angle of attack the flow inboard of the canard vortex is moving in the streamwise direction.

In contrast with the canard at 15° angle of attack, the flow over the wing does not separate along all of the leading edge. Over the inner portion of the wing the flow remains attached. The wing leading-edge vortex starts outboard on the wing at a point that is in line with the vertical tail. The location of this starting point of the wing vortex depends on how strong the downwash induced by the canard vortex is over the wing root region (Reference 3). The canard vortex induces a large downwash on the central part of the wing and an upwash on the outer region. The downwash on the wing is highest at the apex (Reference 1) and prevents the wing leading-edge vortex from forming at the apex of the wing. The upwash induced on the outer region of the wing favors the formation of the wing vortex.

The vortex which forms outboard of the apex of the wing at 15° angle of attack is seen to breakdown outboard of the mid-semispan line. The sudden expansion of the vortex core changes the well organized vortex flow structure into more diffuse vorticity. The burst point of the canard vortex is near the trailing edge of the canard at 15°.

The wing vortex exhibited increased rotational velocity with increasing angle of attack to 18°, while the burst point remains outboard of the mid-semispan line. The starting point of the wing vortex is now inboard of the vertical tail as the spanwise extent of the attached flow on the inner region of the wing is reduced. The canard vortex at 18° angle of attack bursts ahead of the trailing edge and further inboard.

When increasing the angle of attack to 20° and 25°, the burst point of the canard vortex continues to occur further forward and inboard. As the breakdown point of the canard vortex moves inboard, the spanwise extent of the large induced downwash behind the canard is expected to move inboard as well. With an increase in the angle of attack of the wing to 20° and 25°, the starting point of the wing vortex is moving further inboard. At the same time the vortex burst on the wing moves closer to the wing apex.

By 30° angle of attack, the starting point of the wing vortex is inboard of the dye orifice location and may be at the apex of the wing. The wing vortex bursts considerably closer to the wing apex and the wing is close to being stalled. The canard vortex still forms at the apex of the canards, but it bursts soon after. At 35° angle of attack, Figure 4, both the canard and the wing are stalled. A low velocity, turbulent wake extends across the span of both the wing and the canard.

Maneuver Wing-Canard Flow Field

The wing-canard flow field of the maneuver configuration at zero sideslip is presented in Figure 5 in both plan and profile views. The increased leading-edge camber of the maneuver wing and canard is designed to better align the leading edge with the local flow direction. This is done to reduce the high negative pressure peak at the leading edge which causes separation and the formation of a leading-edge vortex. Using a wing geometry that suppresses the formation of the leading-edge vortex has been shown to result in reductions in the drag due to lift (Reference 9).

The flow direction on the surface of the maneuver wing at 10° angle of attack is more streamwise than that seen on the cruise wing in Figure 4. It should be noted when comparing the maneuver to the cruise wing that an additional dye port was added at the root of the wing that remains undeflected for maneuver

configuration. Some dye on the lower surface of the canard passes through the gap between the canard and the fuselage and can be seen on the upper surface. The gap provides clearance between the fuselage and the canard flap when the flap is deflected. There is no indication of a vortex forming on either the wing or the canard at 12° angle of attack. There is some separation and reversed flow in the wing tip region. The reversed direction of this flow can be seen in the profile view of the wing in Figure 5(b).

Comparing the photograph in Figure 4 of the cruise configuration at 15° angle of attack with that of the maneuver configuration in Figure 5, it is clear that the increased leading-edge camber has delayed the formation of the leading-edge vortex on both the canard and wing. The vortex that begins to form on the canard at 15° angle of attack is similar to that seen on the cruise canard at 12°. The vortex which starts to form on the maneuver wing at 15° is outboard of the mid-semispan and located further aft than on the cruise wing. The flow remains attached on the deflected leading edge and separation does not occur until aft of the leading-edge camber.

The vortex which forms on the wing at 18° angle of attack is much weaker and very diffuse compared to that seen on the cruise wing at this angle. The vortex is not rolling up from separation along the straight, sharp leading edge of the cruise wing but rather from the rounded knee at the end of the leading-edge camber. The sweep angle of the core of the vortex on the maneuver wing is less than that on the cruise wing. This reflects the lesser sweep of the hinge line of the leading-edge deflection compared to the wing leading-edge sweep. On the canard at 18° angle of attack, a leading-edge vortex has formed outboard of the root of the canard. Near the canard root, the increased camber delays the leading-edge separation compared to the cruise canard.

The leading-edge camber on the maneuver canard is still delaying the development of the vortex near the root at 20° angle of attack. In the profile view of Figure 5(b) it can be seen that the flow over the canard root is attached to the surface and that when the separation occurs the vortex clearly forms above the surface of the canard. On the maneuver wing at 20° angle of attack, the breakdown of the vortex is further aft than on the cruise wing. With increasing angle of attack, the flow separation point on the outer portion of the wing moves forward from the end of the camber to the leading edge. This can be seen in the

profile views of Figure 5(b) where the point of flow separation moves forward with increasing angle of attack.

The vortex on the maneuver wing, Figure 5, continues to roll up further aft of the leading edge than the vortex on the cruise wing at 25° angle of attack. The starting point of the maneuver canard vortex finally reaches the apex of the canard at 25°. The increased leading-edge camber of the maneuver configuration produces a significant delay in the vortex breakdown on both the canard and the wing at 25° angle of attack.

At 30° angle of attack, the origin of the maneuver wing vortex has moved inboard toward the apex of the wing. The vortex burst occurs further aft on the maneuver wing compared to the cruise wing. The maneuver canard vortex appears to be stronger than the cruise canard vortex at 30° and it bursts further aft from the apex. By 35° angle of attack the maneuver wing is stalled as is the case for the cruise wing. On the maneuver canard, however, a vortex is still formed but it bursts very near the apex.

Figure 6 presents the progression of the burst point of both the cruise and maneuver wing vortices. The location of the vortex breakdown is measured in the profile view along a line normal to the surface. As mentioned before, the increased leading-edge camber of the maneuver wing reduces the pressure peak at the leading edge and so delays the formation of the leading-edge vortex. The leading-edge camber also delays the vortex breakdown to higher angles of attack once the vortex has formed. This effect is present over the entire angle of attack range. The breakdown of the wing vortex at a given fuselage station was delayed by from 2° to 4° as seen in Figure 6.

The effect of leading-edge camber on the breakdown of the canard vortex is shown in Figure 7. As on the wing, the maneuver shape delays the burst of the vortex to higher angles of attack. At the lower range of angles of attack, this delay is only 1° but it increases for angles of attack above 22°. The maneuver configuration of the canard has increased camber over the inboard 60% of the span with very little camber added outboard of 60% (Reference 2). The influence of the camber is not strongly felt until the origin of the vortex and its burst point have moved to the inboard region of the maneuver canard. On the maneuver wing the camber was increased across the entire span of the wing. Part of

the delay of the vortex breakdown on the maneuver wing may be due to the delay in the breakdown of the vortex on the maneuver canard.

The influence of Reynolds number on the vortex breakdown position has been investigated at Northrop and by others. In the Northrop studies (Reference 6), the angle of attack at which vortex breakdown occurred at the trailing edge was observed on delta wings having leading-edge sweep angles of 55° to 85°. Figure 8, which is taken from Reference 6, shows that the results obtained in the Northrop water tunnels fall within the range of angles of attack observed by others. The data shown include results from other water tunnels as well as wind tunnels and covers the Reynolds number range of 10^4 to 10^6, based on root chord. Note that the variation in the data due to Reynolds number is no greater than the variation associated with different facilities and different flow visualization techniques at the same Reynolds number. All of the data follow the same trend of increasing angle of attack for vortex breakdown at the trailing edge as the leading-edge sweep angle is increased. On a delta wing of 55° leading-edge sweep, the vortex breakdown at the trailing edge occurs at approximately 13° angle of attack. The HiMAT canard has a leading-edge sweep of 55°, and the vortex on the cruise canard bursts at the trailing edge at 12° angle of attack. On wings of lower sweep, the vortex will burst before reaching the trailing edge.

At positive angles of attack, the wake of the canard passes above the wing. The HiMAT is a high canard configuration and the 20° of dihedral raises the canard wake further above the wing. The vertical tails are widely spaced laterally on the HiMAT and are canted outboard by 15° but are still inboard of the tips of the canard. At low angles of attack a tip vortex is formed on the maneuver canard. At 5° angle of attack this tip flow is seen in Figure 9, to impinge on the top of the vertical tail. When the angle of attack is increased to 8°, the tip flow passes above the vertical tail. The profile views of the flow field at higher angles of attack are given in Figure 5(b). The wake from the tip of the canard passes above the vertical tail. The wake from the more inboard area of the canard passes between the vertical tails. By 18° angle of attack, the entire wake of the canard appears to pass above the top of the vertical tails.

Effect of Canard on Wing

The flow field of the maneuver wing alone, without the maneuver canard, at zero sideslip is presented in Figure 10. There is attached flow on the upper surface of the wing at 10° angle of attack, and the dye being ejected remains within the boundary layer. The dye shows less spanwise spreading than is seen on the maneuver wing in the presence of the maneuver canard in Figure 5. With an increase in angle of attack to 12°, the surface flow on the wing alone moves more spanwise than before, but it is still much less than in the flow field of the wing with the canard in Figure 5.

A vortex has formed on the wing by 14° and can be seen at 15° angle of attack in Figure 10. The vortex is formed aft of the leading-edge camber on the maneuver wing. The flow remains attached on the deflected leading edge and separation does not occur until aft of the leading-edge camber.

In comparing the wing alone, Figure 10, to the maneuver wing-canard configuration of Figure 5, the wing vortex is seen to move further inboard when the canard is removed. On the wing alone, the vortex starts inboard at the wing root and breaks down just inboard of mid-semispan. On the wing in the presence of the canard, the starting point of the wing vortex is at the mid-semispan and the vortex burst occurs further outboard. The presence of the canard shifts the wing vortex from inboard of mid-semispan to completely outboard of the mid-semispan station.

The canard induced downwash on the central part of the wing prevents the wing leading-edge vortex from forming at the apex of the wing. The canard vortex can induce a sidewash on the wing, as well as an upwash and downwash. Since the sidewash is from the lower half of the canard vortex, it will be directed spanwise, outboard. The spanwise flow is much less when the canard is removed, Figure 10, compared to when the canard is in place, Figure 5. The canard induced sidewash on the wing increases the effective sweep angle of the leading edge of the wing. An increase in effective wing sweep increases the stability of the wing vortex which delays its breakdown to a higher angle of attack.

When the angle of attack is increased to 18° and then to 20°, the burst point of the wing vortex continues to move forward while more of the outboard wing panel becomes stalled. The addition of the maneuver canard, Figure 5, noticeably delays the vortex burst on the wing while it shifts the wing vortex further outboard. The attached flow downstream and inboard of the wing vortex will extend over a larger area on the wing-canard configuration than on the wing alone.

At 25° angle of attack, the wing alone is nearly stalled. A wing vortex forms at the wing apex but bursts soon after, Figure 10. The addition of the maneuver canard, Figure 5, causes a stronger vortex to be formed and it extends further outboard than on the wing alone. The vortex on the wing alone bursts considerably closer to the wing apex than when in the presence of the canard. The flow field on the wing with the canard is better organized than the flow field on the wing alone, which was very unsteady.

By 30° angle of attack, the wing alone has stalled, Figure 10, as the wing vortex is completely broken down. Although the leading-edge vortex on the canard bursts near the apex at 30°, the presence of the canard can still delay the burst of the wing vortex. The wing in the presence of the canard is seen in Figure 5 to be stalled by 35°, as the canard vortex bursts very close to the canard apex.

The addition of the maneuver canard is seen to have a favorable interference effect on the flow field of the wing. This effect is due to the downwash of the canard which decreases the effective angle of attack over the inner region of the wing. This enables the wing vortex flow to exist up to much higher angles of attack than for the wing alone.

The effect of the maneuver canard on the vortex breakdown on the maneuver wing is presented in Figure 11. The presence of the canard delays the breakdown of the wing vortex at a given fuselage station to a higher angle of attack. The delay in the vortex burst due to the addition of the canard becomes larger with increasing angle of attack of the wing. The wing stall and complete breakdown of the wing vortex is delayed from 25° angle of attack for the wing alone to 33° for the maneuver wing-canard configuration.

Figure 12 presents the lift coefficients as functions of angle of attack for the cruise wing-canard configuration and for the cruise wing alone. These curves were obtained from data on a 0.22-scale model tested in the Rockwell NAAL low-speed wind tunnel. The curves show that the addition of the canard area increased the lift coefficients of the total configuration at all angles of attack. These lift coefficients are based on a constant wing reference area. At the lower angles of attack, there is only a slight increase in lift despite the 30% increase in lifting surface area. The downwash from the canard tends to reduce the lift on the wing, as was measured on the configurations of References 4 and 5.

At the higher angles of attack, the wing alone stalls first and so produces a lower lift than the wing in the presence of the canard for which the stall is delayed. From the water tunnel tests, this increase in the lift is seen to be due to the delay in the breakdown of the wing vortex in the presence of the canard. The rate of lift increase for the cruise wing-canard configuration is reduced when the wing becomes completely stalled at 29°. Good agreement is obtained between the observed angle of attack for vortex breakdown at the apex of the canard of 34° and the angle of attack at which the maximum lift for the total configuration occurs.

Figure 13 presents pitching moments as functions of angle of attack for the cruise wing-canard configuration and for the cruise wing alone. The curves show that by adding the canard, the aerodynamic center is moved forward somewhat at low angles of attack with a large forward shift at moderate to high angles of attack. The cruise wing alone has a less stable rate of change of pitching moment with angle of attack above about 10° angle of attack. This occurs as first the wing tip regions become stalled and then the wing leading-edge vortex forms.

The nonlinear pitching moment characteristics of the canard configuration are associated with the development of the vortex lift and the stall of the wing tips. The leading-edge vortices cause large suction peaks beneath themselves on the canard and the wing. At the same time, a loss in lift is occurring at the wing tips, outboard of the vortex, as the stall reaches the wing leading edge. The HiMAT has its center of gravity toward the front of the wing and small stalled areas in the wing tip region will increase the pitch-up tendency because of the long moment arm involved. As

seen in Figure 4, the vortices are forming at 12° angle of attack on both the cruise wing and canard as the flow separates at the leading edge over the outboard regions of both surfaces. Figure 13 shows that the nose-up pitching moments increase rapidly for angles of attack greater than 10°. With increasing angle of attack the vortex burst moves forward and inboard on both the wing and the canard. This change in the flow field reduces the lift over the aft portion of the wing and canard while the lift is maintained on the forward portion. This will increase the pitch-up tendency with increasing angle of attack until the wing and canard are close to stall.

It can be seen in Figure 13 that above about 10° angle of attack, the rate of change of the pitching moment with angle of attack, C_{m_α}, is high unstable. It does not become stable until above 25° angle of attack. The unstable break could be large enough to overpower the available pitch control. The use of the canard flap was proposed to increase the stability by minimizing this unstable break (Reference 2). The canard flap is deflected with increasing angle of attack until it reaches 20° trailing-edge up for angles of attack of 16° and higher. This upward deflection of the canard trailing-edge flap reduces the lift on the canard, thereby reducing the nose-up pitching moment, and so providing the required control margin as discussed in Reference 2.

In the water tunnel, the canard flap was tested at a constant deflection of 20° trailing edge up for the entire angle-of-attack range tested. The flow field of the maneuver wing-canard with this flap deflection is presented in Figure 14. Comparing the photographs in Figure 14 with those in Figure 5 of the maneuver wing-canard without the flap deflection, it is evident that there are no major changes in the flow field. The starting point of the wing vortex is shifted slightly inboard in Figure 14 which indicates that the downwash behind the canard is reduced by the upward canard flap deflection. The wing vortex is more diffuse and bursts further forward at 25° and 30° angle of attack with the flap deflected. The upward canard flap deflection has a direct effect on the canard vortex forcing an early vortex breakdown. The progression of the burst point of the maneuver canard vortex with and without the 20° trailing-edge up flap deflection is presented in Figure 15. The progression of the vortex burst with angle of attack is very similar for both. With the flap deflected, the vortex burst at a given fuselage station occurs approximately 1° sooner than with no flap deflection.

Engine out operation was simulated in the water tunnel by shutting off the suction to the inlet. The flow field of the maneuver wing-canard with no inlet mass flow is presented in Figure 16. The canard vortex is seen to be forming sooner at 12° angle of attack and is well defined by 15°. With the inlet flow on, the canard vortex was seen in Figure 5 to be forming at 15° and still not tightly rolled up at 18° angle of attack. At the higher angles of attack, the burst of the canard vortex is further forward with the inlet flow off.

The flow field of the maneuver canard with the inlet flow off is similar to that of the cruise canard shown in Figure 4. This indicates that the local angle of attack at the canard is increased with the inlet flow off. In Figure 5(b) it can be seen that the apex of the canard is just forward of the inlet lip. With the inlet suction turned off, a portion of the freestream flow is no longer turned toward the inlet but instead continues at a constant, larger angle of attack toward the inboard region of the canard. This increased angle of attack counteracts some of the leading-edge camber which geometrically reduces the angle of attack on the inner portion of the maneuver canard.

The lack of flow through the inlet has less of an effect on the wing flow field. This can be seen by comparing Figure 16 with Figure 5 of the maneuver wing-canard with flow through the inlet. At the higher angles of attack of 25° and 30°, the wing vortex is more diffuse and bursts further forward with the inlet flow off. It appears that the small changes in the wing flow field are due to the changes that occur on the canard.

Wing-Canard Flow Field in Sideslip

The sensitivity of the wing-canard flow field to an angle of sideslip was studied. The model was set at 5° sideslip angle and the angle of attack was varied from 10° to 35°. Photographs of the cruise wing-canard flow field at 5° sideslip are presented in Figure 17.

At 12° angle of attack, the canard leading-edge vortices are well formed, as is the leeward wing vortex. On the windward side, the flow remains attached on the wing. In a sideslip attitude, the windward wing and canard are at an effectively lower sweep angle. With the effective sweep reduced on the windward side, a higher angle of attack is required for the wing vortex to form. By 18° angle of attack, the windward wing vortex has formed.

Comparing the canard and wing at 5° sideslip in Figure 17 with those at zero sideslip and 18° or 20° angle of attack in Figure 4, shows that the vortex burst on the windward side occurs further forward than at zero sideslip while on the leeward side, the vortex burst is delayed to further downstream. The leeward wing and canard are at an effectively higher sweep angle in sideslip. This higher sweep increases the axial velocity of the vortex at the expense of the rotational velocity which was seen to be reduced. This increases the vortex stability, while reducing the vortex strength. With their increased stability, the leeward wing and canard vortices burst further downstream. The decrease in vortex strength will reduce the vortex lift on the leeward side compared to the vortex lift on the wing and canard at zero sideslip. This was observed in the pressure measurements made on a delta wing in Reference 10.

On the windward side, the leading-edge sweep angle is effectively reduced. This decreases the stability of the wing and canard vortices, causing them to burst further forward. The rotational velocity of the windward vortices was observed to be increased. This increases the vortex strength and will increase the vortex lift on the windward side (Reference 10). The velocity component normal to the quarter chord of both the wing and the canard is greater on the windward side, which will also increase the lift.

The canard dihedral of 20° will increase the angle of attack of the windward canard in sideslip while reducing the angle of attack on the leeward side. The increase in angle of attack will increase the lift on the windward canard and will cause the windward canard vortex to burst further forward. The dihedral will have the opposite effect on the leeward canard.

The increased lift on the windward wing and canard contribute to a stable rolling moment in sideslip. The breakdown of the windward vortices moves forward and inboard faster than on the leeward side, which will begin to reduce the stable rolling moment. At 30° angle of attack, the windward wing and canard are close to stall while a vortex is still present on the leeward canard. This early stall of the windward side will reduce the stable rolling moment even further.

At 25° angle of attack, Figure 17 shows that the burst of the windward wing vortex has moved inboard of the windward vertical tail. Aft of the burst,

the flow is seen to be moving outboard. The dye is being pulled into the region of low velocity and reversed flow in the stalled portion of the windward wing. The flow angle is no longer toward the fuselage as was the case at low angles of attack with the freestream flow. This "adverse" sidewash at high angles of attack, along with a reduction in the dynamic pressure at the vertical tail, has been observed on other swept-wing fighters (Reference 11).

The behavior of the maneuver configuration in sideslip, shown in Figure 18, is similar to that seen on the cruise configuration. The decrease in leading-edge sweep angle and the effect of the canard dihedral will again act on the windward side to increase the lift and shift the vortex burst point further forward. The increased leading-edge camber with the reduced sweep delays the formation of the windward wing and canard vortices to above 15° angle of attack. The stability in roll could be expected to be greater for the maneuver configuration because the leading-edge camber delays the vortex bursting to a higher angle of attack. At 30° angle of attack, neither the windward wing nor the canard are completely stalled, and at 35° a vortex is still formed on the windward canard.

The lateral stability of the cruise configuration is presented in Figure 19. The cruise configuration without the central vertical tails, ventral fins, or canards is seen in Figure 19 to be stable, having a negative value of C_{ℓ_β}, from 0° to 28° angle of attack. At zero angle of attack a stable contribution to the rolling moment is produced by the upper surface winglets. The side force produced by the upper surface winglets acts through a vertical moment arm to produce a stable rolling moment. Between 0° and 14° angle of attack, there is increasing stability caused by the windward wing, having a higher rate of lift production than the leeward wing. Above 14° angle of attack, the lateral stability begins to decrease. This occurs as on the windward wing the wing tip region stalls and the wing leading-edge vortex begins to form.

The net effect of adding the twin vertical tails and ventral fins is shown in Figure 19 to be an increase in lateral stability at low angles of attack. The vertical tails produce a stable rolling moment in sideslip, while the ventral fins produce a destabilizing rolling moment about the body axis. The maximum stability again occurs at 14° angle of attack and the stability again decreases above

that angle. That the angle of attack is unchanged from the wing alone configuration indicates that the vertical tails and ventral fins had minimal influence on the wing flow field. The wing flow field can, however, affect the vertical tails. The wings will shield the vertical tails from the freestream flow with increasing angle of attack. As the stall on the windward wing progresses inboard, the windward vertical tail becomes immersed in the low-velocity wake and will encounter some adverse sidewash. This will reduce the side force on the windward vertical tail and so reduce the stable rolling moment. The windward cruise wing alone is completely stalled by 24° angle of attack. The ventral fins will continue to produce a destabilizing rolling moment at high angles of attack. The addition of the vertical tails and ventral fins to the cruise wing results in a loss of effective dihedral at 24° angle of attack and the instability increases with increasing angle of attack.

As discussed previously, the canard with its 20° of dihedral will generate a stable rolling moment in sideslip. The addition of the canard is shown in Figure 19 to increase the effective dihedral at all positive angles of attack. The canard has a higher sweep than the wing and will therefore stall later and maintain its dihedral effect to higher angles of attack. Also, the favorable interference between the canard and the wing was seen in the water tunnel to delay the stall on the wing. Figure 17 shows the windward cruise wing and canard to be close to stall at 30° angle of attack whereas the cruise wing alone stalls by 24° angle of attack. This delay of the stall on the windward side maintains the effective dihedral up through 28° angle of attack.

The vortex flow on the canard may also influence the flow field at the vertical tails and so alter their contribution to the effective dihedral and direction stability. The canard vortices in Figure 17 have burst near the canard trailing edge and prior to reaching the verticals. Once the burst occurs, the concentrated core of the vortex is eliminated, and the rotational velocities are reduced (Reference 12). The wake from the burst canard vortices in sideslip is seen in Figure 20 to pass near the top half of the vertical tail at 12° angle of attack and to be above the vertical tail by 18° angle of attack. Any sidewash induced on the vertical tails by the burst canard vortex will be from the lower half of the vortex and will therefore be directed outboard. In a sideslip attitude, the induced sidewash from the windward canard vortex on the windward vertical

tail would be destabilizing. On the leeward side, the induced sidewash would increase the stable side force on the leeward vertical tail and thereby increase the lateral-directional stability. At the 5° sideslip condition of Figure 20, the vertical tail on the windward side moves away from the burst canard vortex, which will diminish its destabilizing influence. The vertical tail on the leeward side moves closer to the burst canard vortex, which should contribute to the stability. The results of References 13 and 14 indicate that for close-coupled canard configurations with the vertical tails placed between the wingtip and the canard tip, there will be a favorable interference with the canard flow field in sideslip. This will increase the directional stability and to a lesser extent the effective dihedral.

The directional stability, C_{n_β}, and the side force due to sideslip, C_{Y_β}, are presented in Figure 21 for the cruise configuration with and without the canard. These data include the contribution of the upper surface winglets which were found in Reference 1 to increase the directional stability derivative of the HiMAT by 0.001 at zero angle of attack. The winglets should remain effective throughout the flight regime for both configurations as one of them is always exposed to the freestream flow. The addition of the canard gives a negative contribution to C_{Y_β}. This force toward the leeward side acts ahead of the center of gravity of the HiMAT and produces a large destabilizing yawing moment as is evident in the reduction of the directional stability over the range of angles of attack. The start of the reduction in the directional stability is delayed from 12° for the wing alone to 16° with the canard present. The vertical tails are located where they should encounter favorable interference from the canard, and so reduce the negative increment from the canard itself. The directional stability contribution of the leeward vertical tail would be increased by any induced sidewash from the canard. The windward vertical moves out of the destabilizing sidewash of the burst canard vortex. The stabilizing contribution from the windward vertical tail will be maintained to a higher angle of attack with the canard on because of the delay of the stall of the windward wing.

Forebody Flow Field Characteristics

The flow field of the forebody of the HiMAT at zero sideslip and selected angles of attack is presented in both plan and profile views in Figure 22. At 20° angle of attack, a vortex pair begins to roll up aft of the canopy. The dye being injected from the underside of the fuselage is seen to move upward around the sides of the forebody, then turn aft, and separate from the surface. As the boundary layer flow separates from the sharply sloping rear surface of the canopy, there is initially some rotation in the wake before it becomes turbulent. With increasing angle of attack, the crossflow over the forebody sweeps the boundary layer to the upper surface where it separates and rolls up into a symmetric vortex pair. The rotating helical pattern of the vortex is seen in Figure 22 at 25° angle of attack. The vortices are symmetrical and extend to the wing trailing edge without bursting. In the profile view at 25°, the crossflow angle near the canopy is seen to become progressively less until it runs parallel to the fuselage. The boundary layer separates along this line and becomes the feeding sheet to the forebody vortex.

At 28° angle of attack, the forebody vortices turn outboard and burst before reaching the trailing edge of the wing. Increasing the angle of attack to 30° and then 35°, causes the forebody vortices to turn further outboard and to burst further forward. In Figure 5 it can be seen that the maneuver wing is completely stalled by 35° angle of attack. Above the stalled wing is a large increasing or adverse pressure gradient which will decelerate the axial velocity within the core of the vortex. The vortex will then burst with a rapid expansion to a larger, slower rotating, turbulent flow.

With increasing angle of attack, the rotational velocity of the vortex and so its strength is increased. Also at the higher angles of attack, the vortex pair above the forebody develops a slight asymmetry. At 35° angle of attack and zero sideslip, the asymmetric vortex pattern is seen in the profile view of Figure 22. The left side vortex has shifted upward, away from the surface. The vortex on the right side remains close to the body. The vortex asymmetry becomes more pronounced at 40° angle of attack. The height of the left side vortex above the surface and above the right vortex is increased, and a shift

to the right in the lateral position of the vortex pair can be seen in the plan view of Figure 22.

The resultant force generated by the forebody will be rotated to one side as a result of the shift in the position of the forebody vortices (Reference 11). The vortex which remains closest to the surface of the forebody will exert a larger suction pressure than the one that has moved upward. The reduced influence of the high vortex and the induced suction of the low vortex will change the circumferential pressure distribution over the entire forebody and so produce a net side force toward that side of the forebody on which the vortex is closest (Reference 15). This side force on the forebody will cause asymmetric yawing moments at zero sideslip and high angles of attack.

The flow field around the forebody at 5° of sideslip for selected angles of attack from 20° to 40° is presented in Figure 23. At angles of attack from 20° to 30°, a shift in the position of the vortex pair is evident when compared to the symmetrical pattern seen at zero sideslip in Figure 22. In the profile view of the leeward side, the leeward vortex has shifted to a position lower down on the side of the fuselage relative to its position at zero sideslip. The windward vortex is now higher above the surface of the forebody than the leeward vortex. The boundary layer separation line is shifted to a position lower on the leeward side and higher on the windward side, which indicates a shift in the stagnation line on the lower surface. In the plan view, it can be seen that the lateral shift of the vortex pair is much less than their displacement in height in sideslip. The windward vortex is positioned higher up on the side of the fuselage and closer to the fuselage centerline. The leeward vortex is shifted closer to the side of the fuselage.

With an angle of attack of 35° at 5° sideslip, the arrangement of the vortices is similar to that at lower angles of attack but with the strength of both vortices increased. The windward vortex remains higher above the surface. At zero sideslip and 35° angle of attack, the asymmetric vortex pair was in an orientation that is opposite of that seen in sideslip. At 40° angle of attack, the height of the windward vortex aft of the canopy is greatly increased. In the plan view, the windward vortex is seen to pass above the lower, leeward vortex, which curves toward the centerline and breaks down.

During flight testing of the HiMAT RPRV, a large instrumentation nose boom is used. The nose boom carries flight test instrumentation to determine airspeed, altitude, angle of attack and sideslip. The installation of the nose boom modifies the nose shape and effectively increases the forebody fineness ratio. The length of the forebody is increased where the nose boom is faired smoothly into the nose, while the width of the forebody at the apex of the canards is unchanged.

Figure 24 illustrates the effect of the nose boom on the forebody at zero sideslip. At the lower angles of attack, little change in the flow field is observed. For angles of attack of 28° and higher, a change in the forebody flow field is evident when compared to the forebody without the nose boom in Figure 22. The forebody vortex pair is more diffuse, with greater turbulence, and there is some mixing between the two vortices. Through the use of a traversing dye probe, it was possible to see that the boom sheds a periodic wake which passes near enough to the forebody vortex pair to cause a disturbance. The alternating vortices moving downstream from the boom are responsible for the alternating pattern seen in the plan view at 35° angle of attack. This alternating mixing between the forebody vortices occurs at the same frequency as the vortex shedding from the nose boom.

In the presence of the nose boom, an asymmetric pattern in the forebody vortices is seen at 30° angle of attack. The right side vortex is shifted upward, away from the surface. Without the nose boom, the forebody vortex asymmetry was first seen at 35° angle of attack in Figure 22. Using the traversing dye probe, it was found that the roll up of the forebody vortices begins on the nose boom itself, near its base. The turbulent wake from the boom begins above where the forebody vortices are formed. The addition of the nose boom lowered the angle of onset of vortex asymmetry from 35° angle of attack for boom off to 30° for boom on. This is similar to the effect of increasing the forebody fineness ratio as was shown for tangent ogives in Reference 16. Results of a previous study showed that a long nose boom on a relatively short forebody would increase the effective fineness ratio and so reduce the onset angle of vortex asymmetry in both water tunnel and wind tunnel tests (Reference 17).

At 35° angle of attack, the orientation of the asymmetric forebody vortices is reversed from that seen at 30° angle of attack, with the left vortex now being higher above the surface. By 40° angle of attack, the orientation of the vortex pair has changed again. There is now little asymmetry in the lateral position of the vortex pair and the vortices are at identical heights above the surface as seen in the profile view. The addition of a nose boom to the forebody of the Northrop F-5F is shown in Reference 18 to have a similar effect, causing the asymmetric yawing moments at zero sideslip to undergo changes in direction with increasing angle of attack.

Figure 25 illustrates the effect of the nose boom on the forebody at 5° of sideslip. The periodic wake from the nose boom was again disrupting the forebody vortices at 30° angle of attack. Up to 35° angle of attack, the arrangement of the vortex pair is similar to that seen without the nose boom in Figure 23. The windward vortex remains higher above the surface while the leeward is close to the surface on both configurations.

When the angle of attack is increased to 35° at 5° of sideslip, the vortex orientation is completely reversed. The windward vortex is now closest to the surface while the leeward vortex is shifted upward. This vortex orientation is similar to the asymmetry seen at zero sideslip at 35° angle of attack in Figure 24. By 40° angle of attack, the vortices have returned to the pattern seen in sideslip without the nose boom at 40° in Figure 23.

Figure 26 presents the flow field of the forebody with the maneuver canard removed for zero sideslip. With the canard removed, a well defined vortex pair is formed aft of the canopy at 18° angle of attack. With the canard on, Figure 24, the flow aft of the canopy at 18° was a turbulent wake with some rotational motion beginning at 20° angle of attack. With the canard off, the crossflow near the rear of the canopy is no longer blocked off. This crossflow becomes the feeding sheet to the vortex which forms as the flow separates at the rear of the canopy.

By 25° angle of attack, the vortex pair is forming symmetrically above the canopy and extends to the wing trailing edge before bursting. The periodic wake from the nose boom is disrupting the forebody vortices at 30° angle of attack. Also at 30° an asymmetry in the forebody vortices has developed. The right side vortex is shifted slightly upward from the surface. This asymmetry is in

the same direction as seen with the canard on in Figure 24 but it is not as pronounced. At 35° angle of attack, the orientation of the asymmetric forebody vortices is reversed from that seen at 30° angle of attack, with the left vortex now being higher. This asymmetry in the forebody flow is in the same direction as when the canards were in place. At 40° angle of attack, the forebody vortex asymmetry has reversed orientation again, with the right vortex being higher above the surface. With the canard on, no vortex asymmetry was observed at 40° other than the periodic fluctuations due to the wake from the nose boom.

The flow field around the forebody at 5° of sideslip with the canard removed is presented in Figure 27. In the plan view, a shift in the vortex pair toward the leeward side is evident when compared to the symmetrical pattern seen at zero sideslip in Figure 26. The windward vortex is shifted to a position higher up on the side of the fuselage and closer to the fuselage centerline. The leeward vortex is positioned closer to the side of the fuselage. This shift of the forebody vortices in sideslip is larger than that seen with the canard on in Figure 25. In the profile view of Figure 27, the windward vortex rolls up aft of the canopy at 18° and 20° angle of attack and is higher above the surface of the fuselage than the leeward vortex. With the canard on, the vortices are just beginning to form at 18° and 20° angle of attack in sideslip. When the angle of attack is increased to 25° angle of attack and above with the canard off, the orientation of the vortices is seen to be similar to that at the lower angles. The windward vortex remains furthest from the surface while the leeward vortex remains close to the fuselage over a considerable length. The wake from the nose boom at high angles of attack appears to affect the windward vortex more than the leeward vortex. The windward vortex is also more turbulent with the canard off than with the canard on. This could be due to the fact that with the canard off the windward vortex moves closer to the fuselage centerline and more in line with the wake from the probe. The windward vortex is always higher than the leeward vortex and is therefore closer to the nose boom wake.

At low angles of attack, the forebody is directionally destabilizing because of its side area ahead of the center of gravity. At higher angles of attack, the forebody vortex pair which forms will affect the directional stability of the aircraft. This results primarily from the vortices producing a side force on the forebody rather than an interaction with the vertical tails (Reference 19). Whether this effect is directionally stabilizing or not depends on the vortex

strength and the orientation of the vortices and boundary layer separation lines around the forebody. It was found in the water tunnel that on the HiMAT RPRV in sideslip the leeward vortex is closest to the surface and near the side of the body while the windward vortex is higher above the surface and nearer the fuselage centerline. This vortex orientation in sideslip will change the circumferential pressure distribution over the forebody and so produce a net side force. The net side force is to the leeward side because the leeward vortex is the closest to the surface. Since the side force acts on the leeward side it will tend to pull the forebody further out of alignment with the freestream. This is an unstable yawing moment which will reduce the directional stability.

The directional stability for the cruise configuration without the nose boom is shown in Figure 28. The wake from the nose boom was seen in the water tunnel to begin affecting the forebody flow field at between 25° and 30° angle of attack. The nose boom should have little effect on the stability characteristics of the HiMAT before 30° angle of attack, and the data in Figure 28 are felt to be representative of the configuration tested in the water tunnel. At higher angles of attack, the addition of a nose boom was found in Reference 19 to be destabilizing on other fighter aircraft.

The configuration without the central vertical tails, ventral fins or canard is seen in Figure 28 to have near neutral directional stability up to 18° angle of attack. The destabilizing yawing moment from the fuselage area ahead of the center of gravity is balanced by the stabilizing input of the winglets. This configuration becomes increasingly unstable above 18° angle of attack. This loss in stability is attributed to the forebody vortices. The forebody vortices are seen in Figure 27 to have formed aft of the canopy by 18° angle of attack and to be in an orientation that will produce a destabilizing yawing moment. As the angle of attack is increased, the vortices are formed above the canopy and extend forward to the nose. This greatly increases the area over which the destabilizing side force is produced and increases the moment arm for the yawing moments. The strength of both vortices is increased at the higher angles while the height of the windward vortex above the surface increases. The large loss in directional stability from 24° to 28° angle of attack occurs at the same time as a large negative change in C_{Y_β} in Figure 28. This indicates that the destabilizing yawing moments in sideslip are produced by a side force acting on an area forward of the center of gravity.

The addition of the twin vertical tails and ventral fins contributes a substantial increase in directional stability over the entire angle of attack range shown in Figure 28. This is accomplished by a negative shift in the level of C_{Y_β}. The negative change in C_{Y_β} between 24° and 28° angle of attack from the side force produced by the forebody vortices is still present after the vertical tails are added. A decrease in directional stability does occur from 24° to 28° angle of attack, but the size of the drop is reduced by the increasing, stable contribution of the vertical tails and the ventral fins.

The addition of the canards causes a reduction in the directional stability. The canard surfaces, which are ahead of the center of gravity, give a negative contribution to C_{Y_β} for the lower angles of attack. For angles of attack between 24° and 28°, the canards reduce the destabilizing side force generated by the forebody vortices in sideslip. The addition of the canards to the forebody has several direct effects on the forebody vortex flow field which reduce the vortex induced side forces. The canards block some of the crossflow and delay the formation of the forebody vortex pair to a higher angle of attack. With the canards in place, the lateral shift of the forebody vortices in sideslip is reduced. Adding the canards also reduces the side area over which the forebody vortices could act to produce a side force and destabilizing yawing moment.

Engine out operation was simulated in the water tunnel by shutting off the suction to the inlet. The forebody flow field with no mass flow through the inlet is presented in Figure 29. Comparisons can be made with Figure 24 where the inlet mass flow ratio was set at the standard condition of $\dot{m}_I / \dot{m}_\infty = 1.21$. The other forebody flow field studies were conducted with this inlet flow rate. It was seen in Figure 16 that the local angle of attack at the apex of the canard is increased with the inlet flow off. The forebody vortex pair is seen to be rolling up at 20° angle of attack with the inlet flow off. With the inlet flow on, the flow aft of the canopy is more turbulent. There is no apparent effect of inlet flow rate on the onset of the vortex asymmetry on the forebody or in the orientation of the vortex asymmetry at the higher angles of attack.

CONCLUDING REMARKS

Flow visualization studies were conducted in the Northrop water tunnel to provide qualitative definition of the vortex flow fields occurring on the HiMAT RPRV. Details of the wing, canard, and forebody vortex flow fields were obtained for up to 40° angle of attack and 5° sideslip. The documentation covered the vortex flow field development, vortex path, and vortex breakdown characteristics. The addition of the canard was found to improve the flow field of the wing. The influence of the vortex flow fields in sideslip on the lateral/directional characteristics of the HiMAT was determined. A summary of the flow visualization results is given below and conclusions are made where appropriate.

1. Both a wing leading-edge vortex and a canard leading-edge vortex were formed on the HiMAT in the cruise configuration. The burst points of the wing and the canard vortex moved forward and inboard with increasing angle of attack. The addition of the canard caused the wing vortex to be formed further outboard than on the wing alone. The presence of the canard delayed the breakdown of the wing vortex to a higher angle of attack. The canard induced a downwash and a sidewash on the inboard portion of the wing which reduced the local angle of attack and increased the effective wing sweep, respectively.

2. The increase in the lift, above that from the canard's additional area, is due to the delay in the breakdown of the wing vortex in the presence of the canard, and the higher stall angle of attack of the canard itself. The pitch-up tendency of the HiMAT is associated with the development of the vortex lift on the wing and canard and the stall of the wingtips.

3. The increase in leading-edge camber of the maneuver configuration delayed both the formation and the breakdown of the wing and canard vortices to higher angles of attack. The vortex formed on the maneuver wing was more diffuse than the one found on the cruise wing.

4. With the inlet flow stopped, the formation and the breakdown of the canard vortex occurred at lower angles of attack. This was caused by an increase in the local angle of attack near the canard apex. The upward deflection of the canard flap forced an early breakdown of the canard vortex at all angles of attack.

5. The addition of the canard was seen to increase the effective dihedral. The difference in strength between the vortices in sideslip, with the windward vortices increasing in strength, contributes to a stable rolling moment. The canard was found to maintain a moderate level of lateral stability at the higher angles of attack by delaying the stall on the windward side. The vertical tails encounter favorable interference from the canard wake in sideslip which would reduce the overall adverse directional stability contribution from the canard.

6. The forebody vortices were observed to roll up first aft of the canopy. When the angle of attack was increased, the vortices were formed above the canopy and extended forward to the nose. Asymmetries were observed in the forebody vortices for angles of attack of 35° and greater.

7. The variations in directional stability with the canard off at the higher angles of attack were found to be influenced by the orientation of the forebody vortex system in sideslip. The forebody produces a vortex pattern in sideslip that would generate a destabilizing yawing moment throughout the high angle-of-attack range. The addition of the canard reduces the destabilizing influence of the forebody vortices in sideslip.

8. The addition of the large nose boom to the short forebody of the HiMAT was found to effectively increase its fineness ratio. This reduced the angle of onset of vortex asymmetry at zero sideslip to 30° angle of attack. The turbulent wake shed from the nose boom was seen to cause switching in the positions of the vortices with increasing angle of attack. The wake from the nose boom alters the forebody vortex orientations in sideslip and disturbs the structure of the forebody vortices.

REFERENCES

1. Gingrich, P.B., Child, R.D., and Panageas, G.N., "Aerodynamic Configuration Development of the Highly Maneuverable Aircraft Technology Remotely Piloted Research Vehicle," NASA CR-143841, March 1977.

2. Brown, L.E., Roe, M., and Wilder, C.D., "The HiMAT RPRV System," AIAA Paper 78-1457, August 1978.

3. Behrbohm, H., "Basic Low Speed Aerodynamics of the Short-Coupled Canard Configuration of Small Aspect Ratio," SAAB TN 60, Saab Aircraft Co., July 1965.

4. Gloss, B.B., and McKinney, L.W., "Canard Wing Lift Interference Related to Maneuvering Aircraft at Subsonic Speeds," NASA TM X-2897, December 1973.

5. Gloss, B.B., "The Effect of Canard Leading Edge Sweep and Dihedral Angle on the Longitudinal and Lateral Aerodynamic Characteristics of a Close-Coupled Canard-Wing Configuration," NASA TN D-7814, 1975.

6. Erickson, G., "Water Tunnel Flow Visualization: Insight Into Complex Three-Dimensional Flow Fields," AIAA Paper 79-1530, 1979.

7. Poisson-Quinton, Ph. and Werlé, H., "Water Tunnel Visualization of Vortex Flow," Astronautics and Aeronautics, June 1967.

8. Werlé, H., "Hydrodynamic Flow Visualization," Annual Review of Fluid Mechanics, Volume 5, pp. 361-382, 1973.

9. Kulfan, R.M., "Wing Geometry Effects on Leading Edge Vortices," AIAA Paper 79-1872, August 1979.

10. Hummel, D., "Untersuchungen über das Aufplatzen der Wirbel an schlanken Delta-flügeln," Z. Flugwiss. 13, pp. 158-168, 1965.

11. Chambers, J.R. and Grafton, S.B., "Aerodynamic Characteristics of Airplanes at High Angles of Attack," NASA TM-74097, 1977.

12. Hayashi, Y. and Terusmi, N., "Flow Field in a Vortex with Breakdown Above Sharp Edged Delta Wings," Report NAL-TR-423, August 1975.

13. Huffman, J.K., "Effect of Vertical-Tail Location of the Aerodynamic Characteristics at Subsonic Speeds of a Close-Coupled Canard Configuration," NASA TN D-7947, 1975.

14. Henderson, W.P., "The Effect of Canard and Vertical Tails on the Aerodynamic Characteristics of a Model with a 59° Sweptback Wing at a Mach Number of 0.30," NASA TM X-3088, 1974.

15. Peake, D.J., Owen, F.K., and Johnson, D.A., "Control of Forebody Vortex Orientation to Alleviate Side Forces," AIAA Paper 80-0183, January 1980.

16. Keener, E.R., Chapman, G.T., and Kruse, R.L., "Effects of Mach Number and Afterbody Length on Onset of Asymmetric Forces on Bodies at Zero Sideslip and High Angles of Attack," AIAA Paper 76-66, 1976.

17. Lorincz, D.J., "Water Tunnel Flow Visualization Study of the F-15," NASA CR-144878, 1978.

18. Headly, J.W., "Analysis of Wind Tunnel Data Pertaining to High Angle-of-Attack Aerodynamics," AFFDL TR-78-94, Volume I, 1978.

19. Carr, P.C. and Gilbert, W.P., "Effects of Fuselage Forebody Geometry on Low-Speed Lateral-Directional Characteristics of Twin-Tail Fighter Model at High Angles of Attack," NASA TP-1592, 1979.

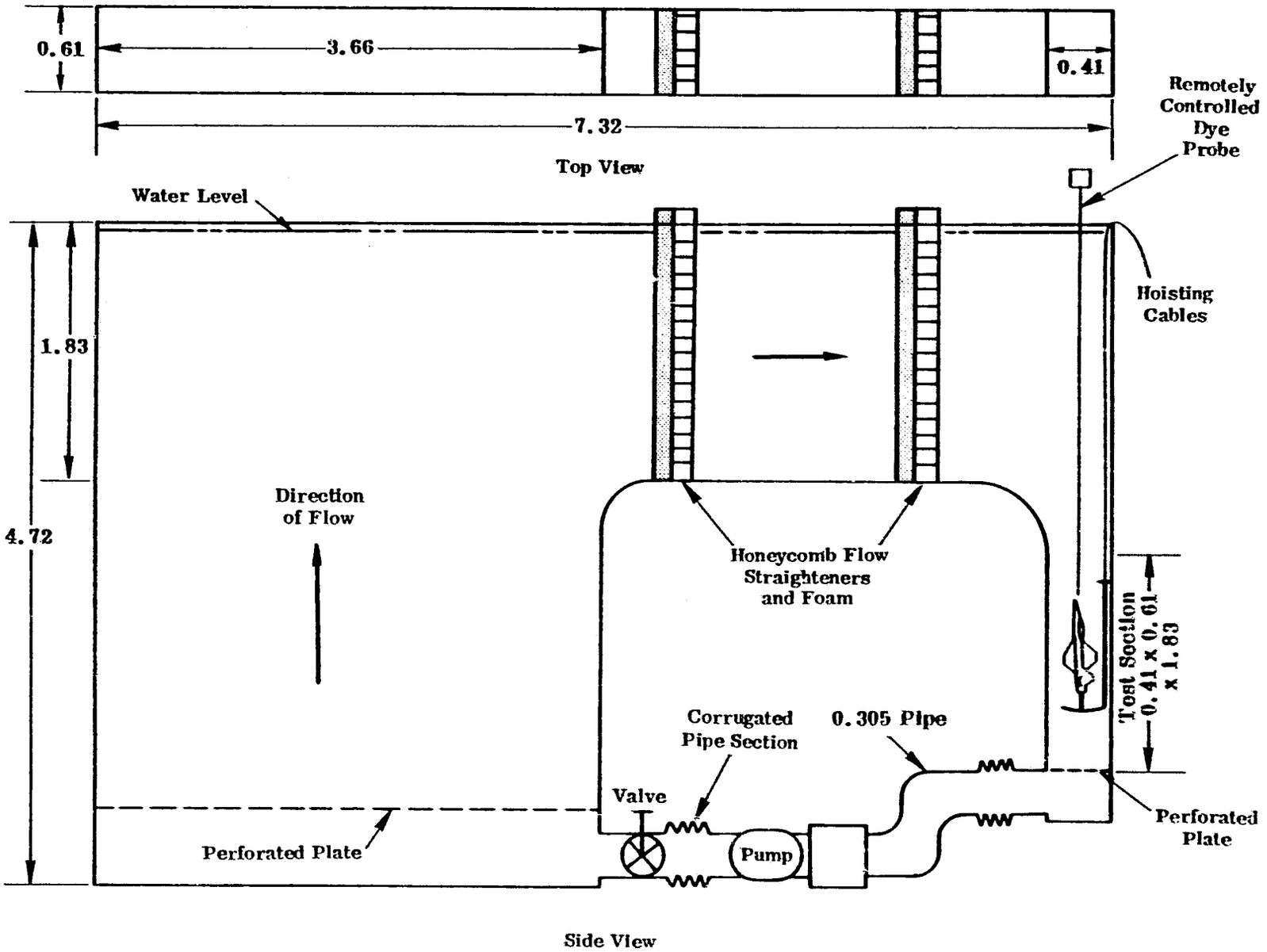

FIGURE 1. NORTHROP DIAGNOSTIC WATER TUNNEL (ALL DIMENSIONS IN M)

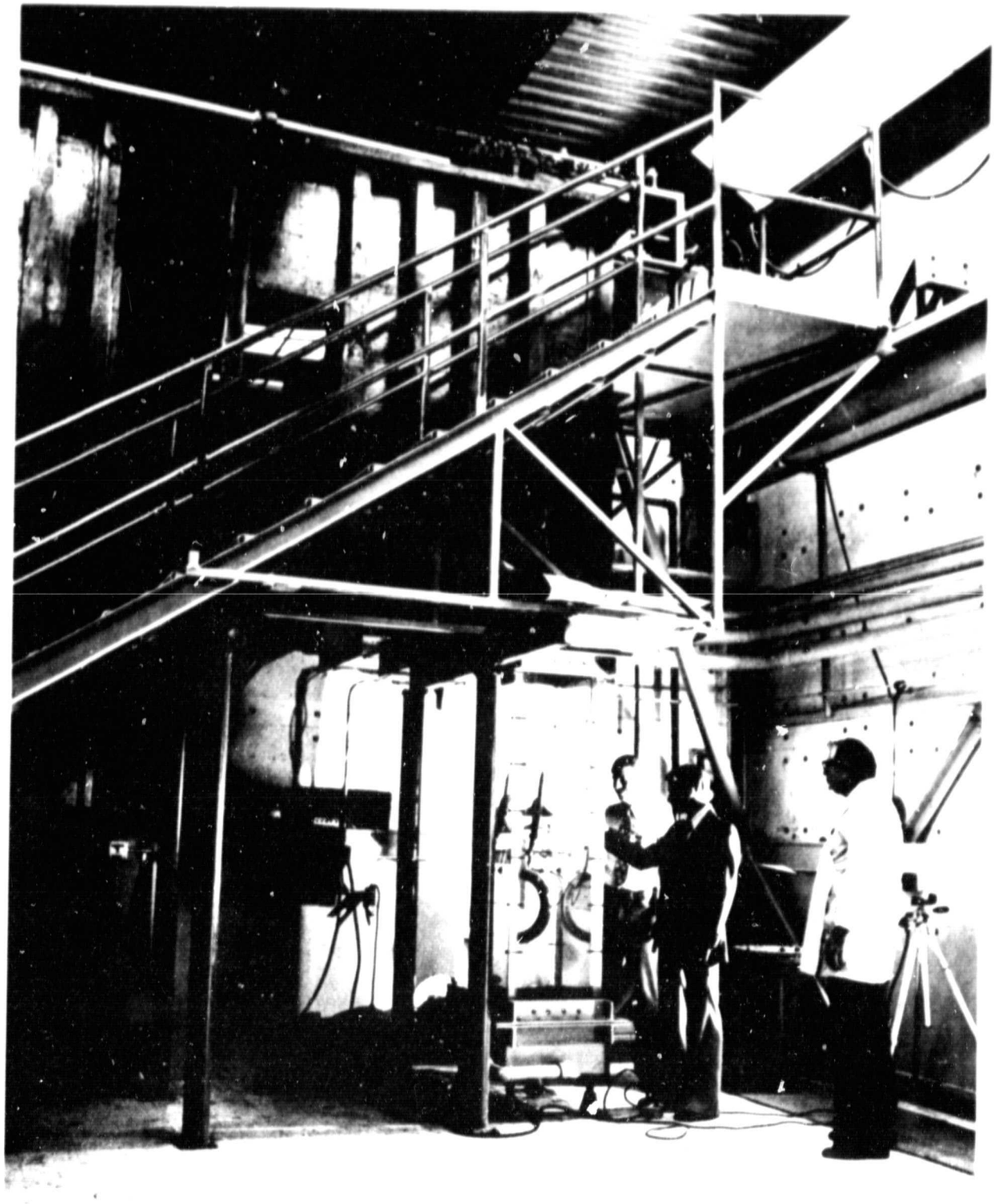

79-03669-7

FIGURE 2. MODEL INSTALLED IN WATER TUNNEL

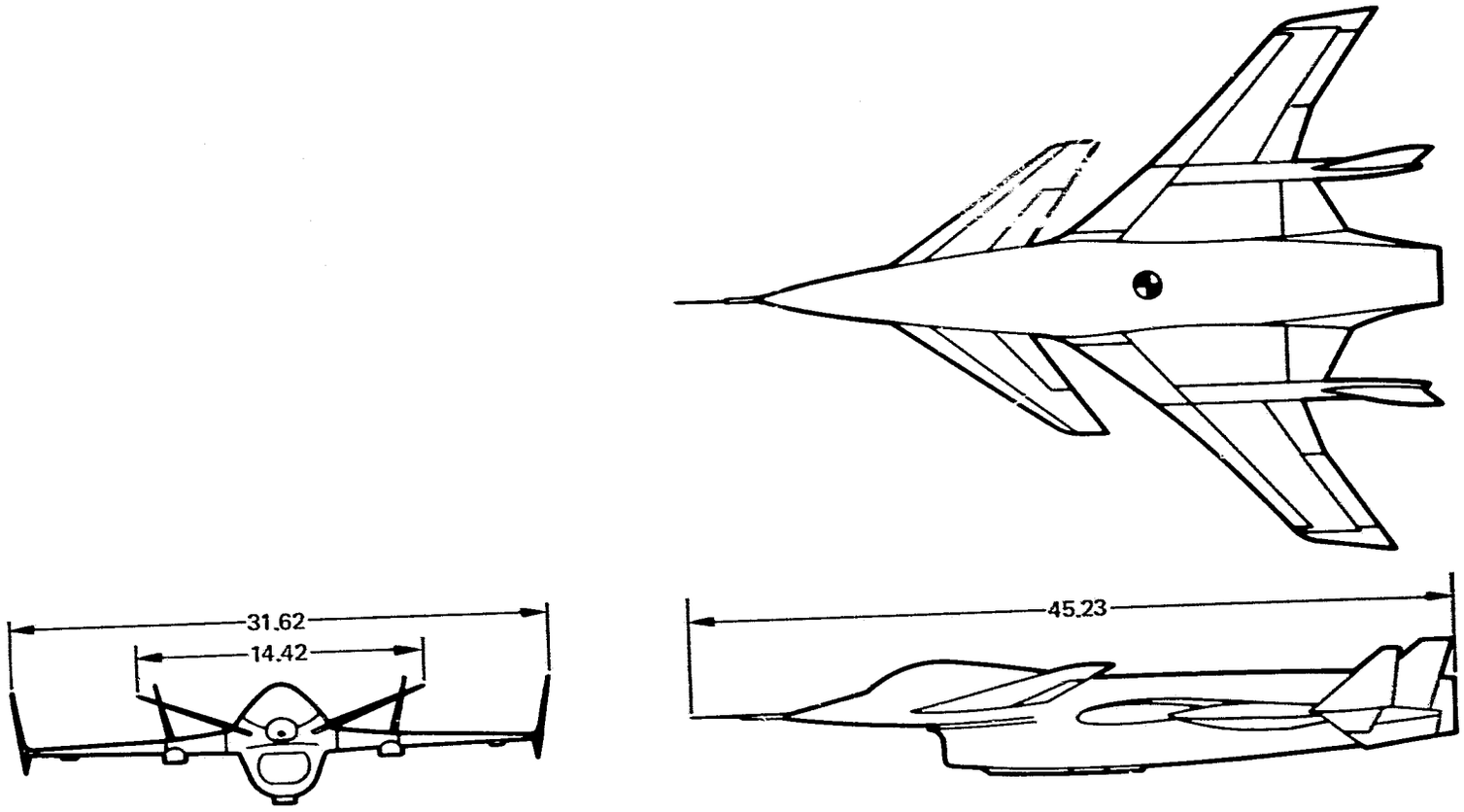

FIGURE 3. 1/15-SCALE HIMAT RPRV THREE VIEW DRAWING
(ALL DIMENSIONS IN CM)

$\alpha = 10^{o}$

$\alpha = 12^{o}$

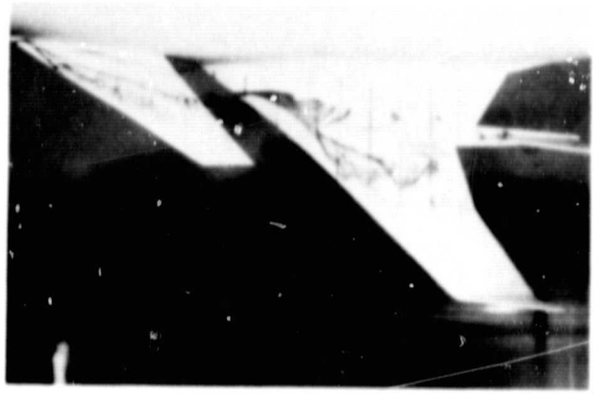

$\alpha = 15^{o}$

$\alpha = 18^{o}$

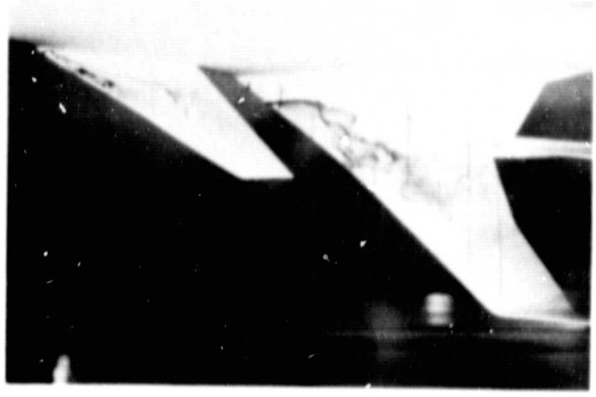

$\alpha = 20^{o}$

$\alpha = 25^{o}$

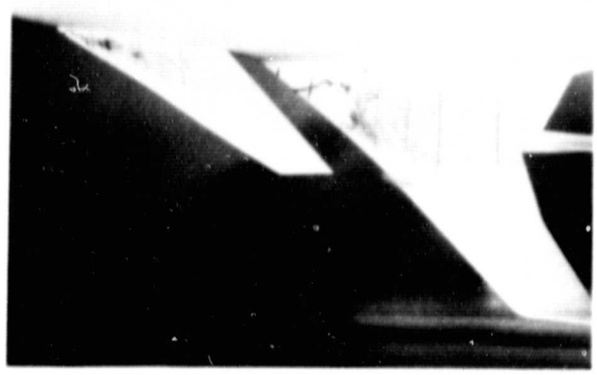

$\alpha = 30^{o}$

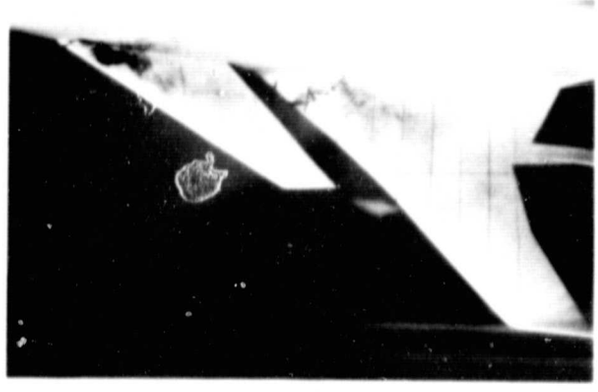

$\alpha = 35^{o}$

FIGURE 4. CRUISE WING-CANARD FLOW FIELD FOR $\beta = 0^{o}$

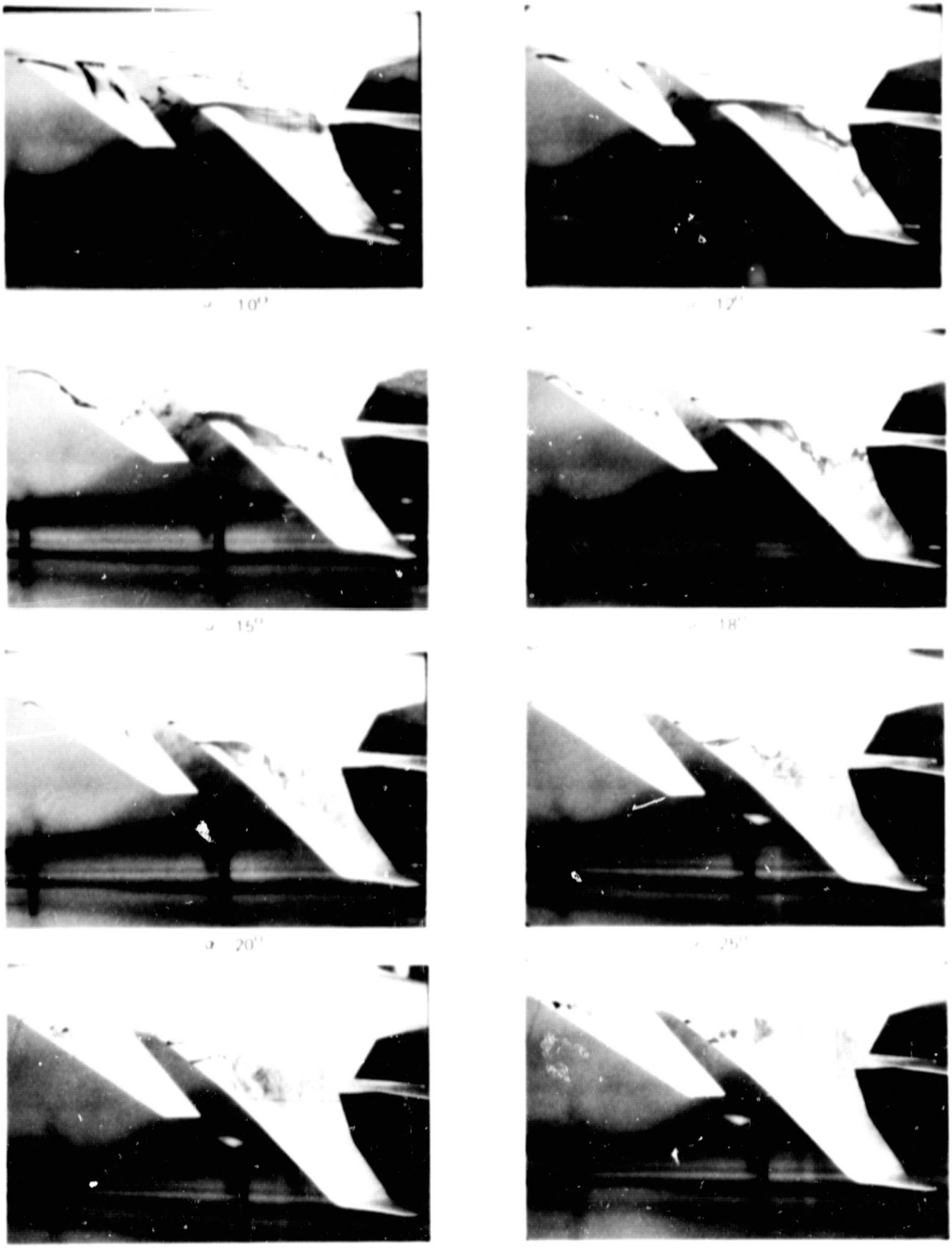

FIGURE 5 MANEUVER WING-CANARD FLOW FIELD FOR $\beta = 0^{\circ}$

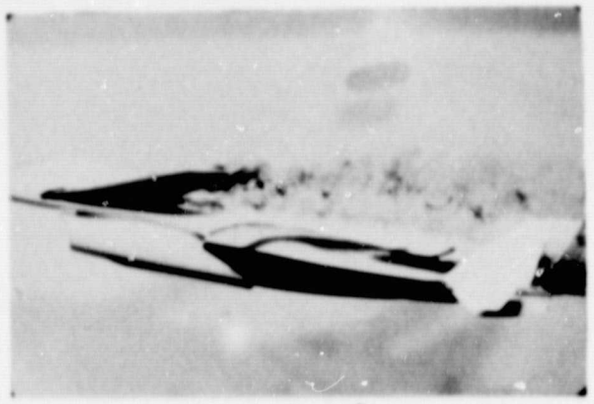

$\alpha = 10^{\circ}$

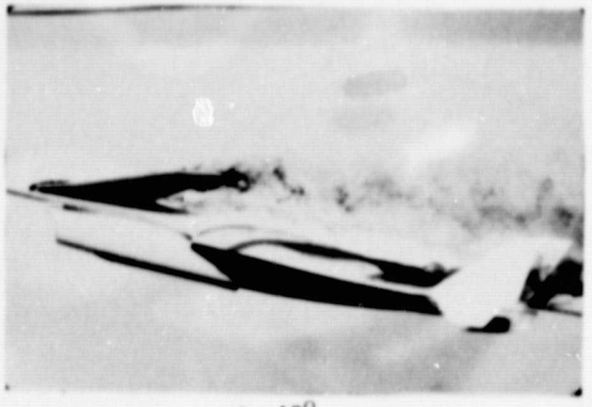

$\alpha = 12^{\circ}$

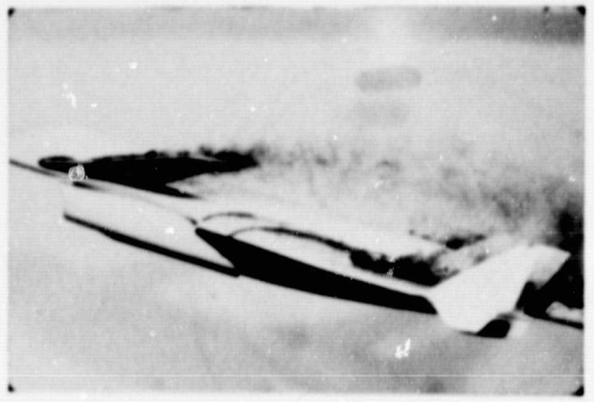

$\alpha = 15^{\circ}$

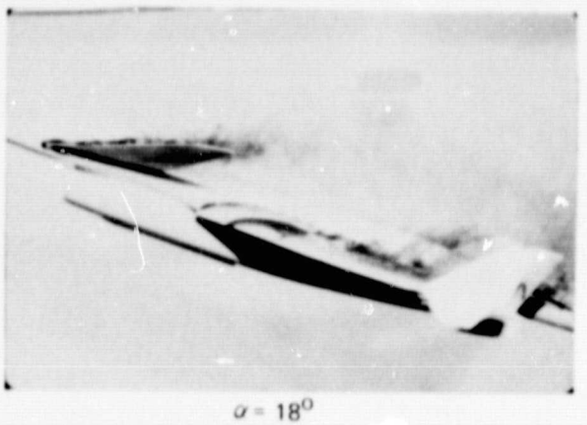

$\alpha = 18^{\circ}$

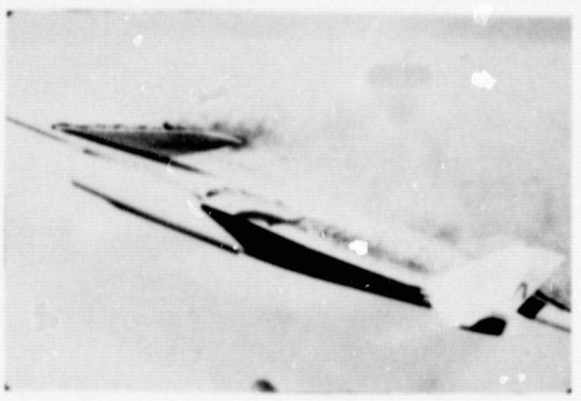

$\alpha = 20^{\circ}$

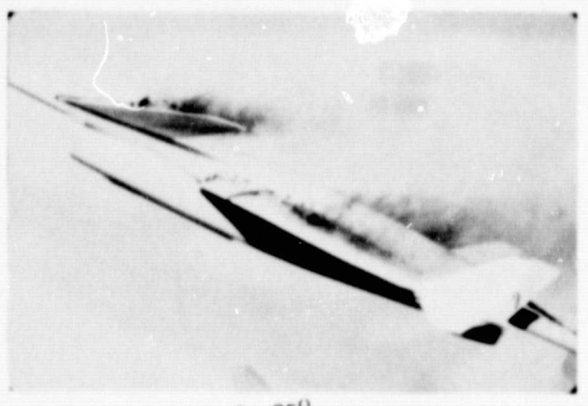

$\alpha = 25^{\circ}$

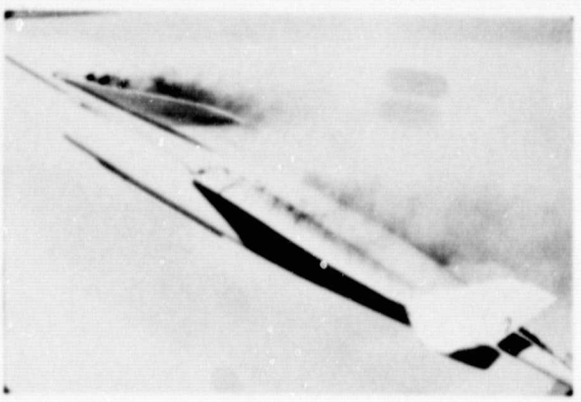

$\alpha = 30^{\circ}$

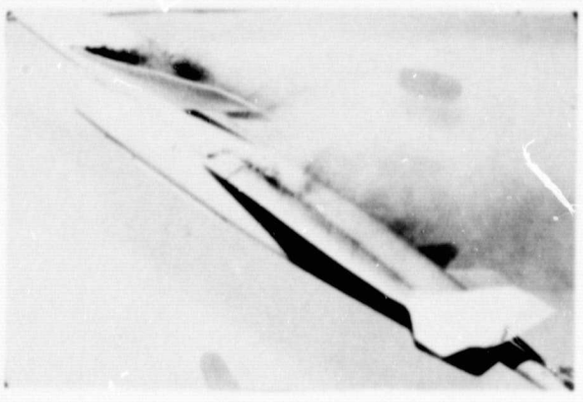

$\alpha = 35^{\circ}$

(B) PROFILE VIEW

FIGURE 5. CONCLUDED

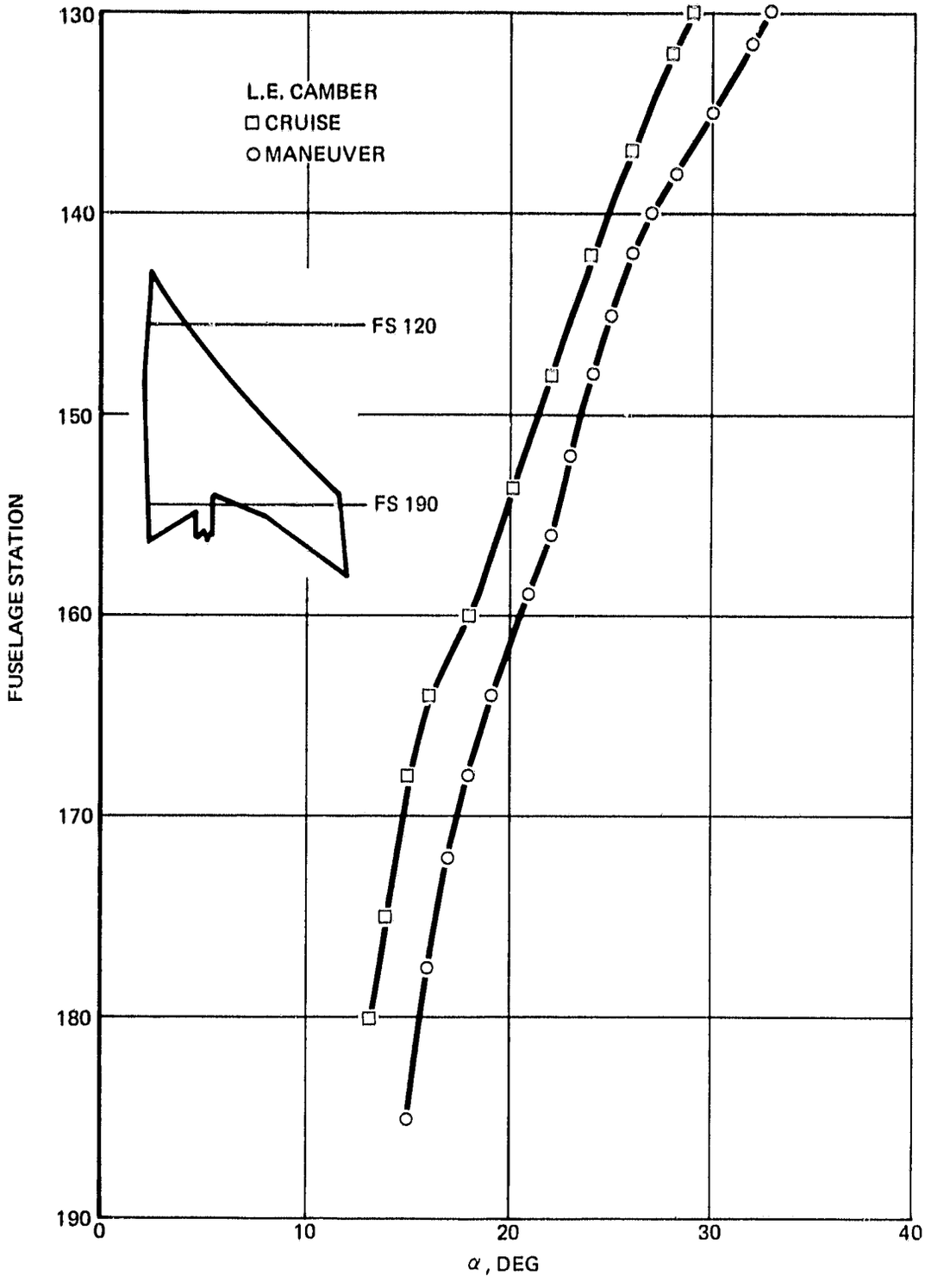

FIGURE 6. EFFECT OF LEADING-EDGE CAMBER ON VORTEX BREAKDOWN OF HIMAT WING

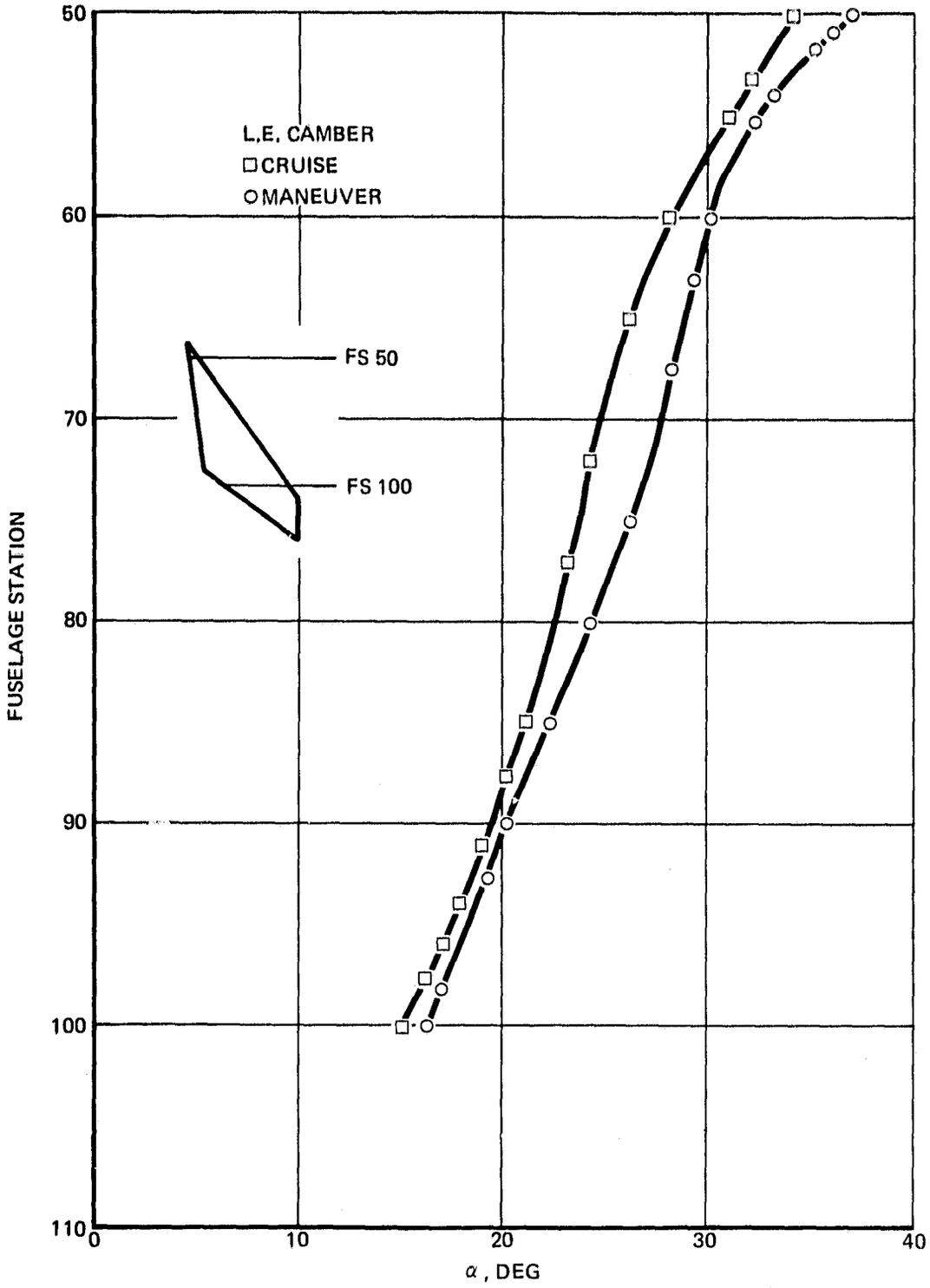

FIGURE 7. EFFECT OF LEADING-EDGE CAMBER ON VORTEX BREAKDOWN OF HIMAT CANARD

		Facility (Method)	Reynolds No.
○	Northrop 16 x 24 in.	Water Tunnel (Dye)	$2.0(10^4)$
●	Northrop 6 x 6 in.	Water Tunnel (Dye)	$1.5(10^4)$
□	Wentz	Wind Tunnel (Schlieren)	10^6 (approx.)
◇	Poisson-Quinton & Erlich	Water Tank (Dye; aluminum Particles)	$2(10^4)$ (approx.)
△	Chigier	Wind Tunnel (Laser anemometer)	$2(10^6)$ (approx.)
▽	Earnshaw and Lawford	Wind Tunnel (Tuft probe)	(10^6) (approx.)
▲	Hummel and Srinivasan	Wind Tunnel (Smoke)	(10^6) (approx.)
☆	Lowson	Water Tunnel (Dye)	$3(10^4)$

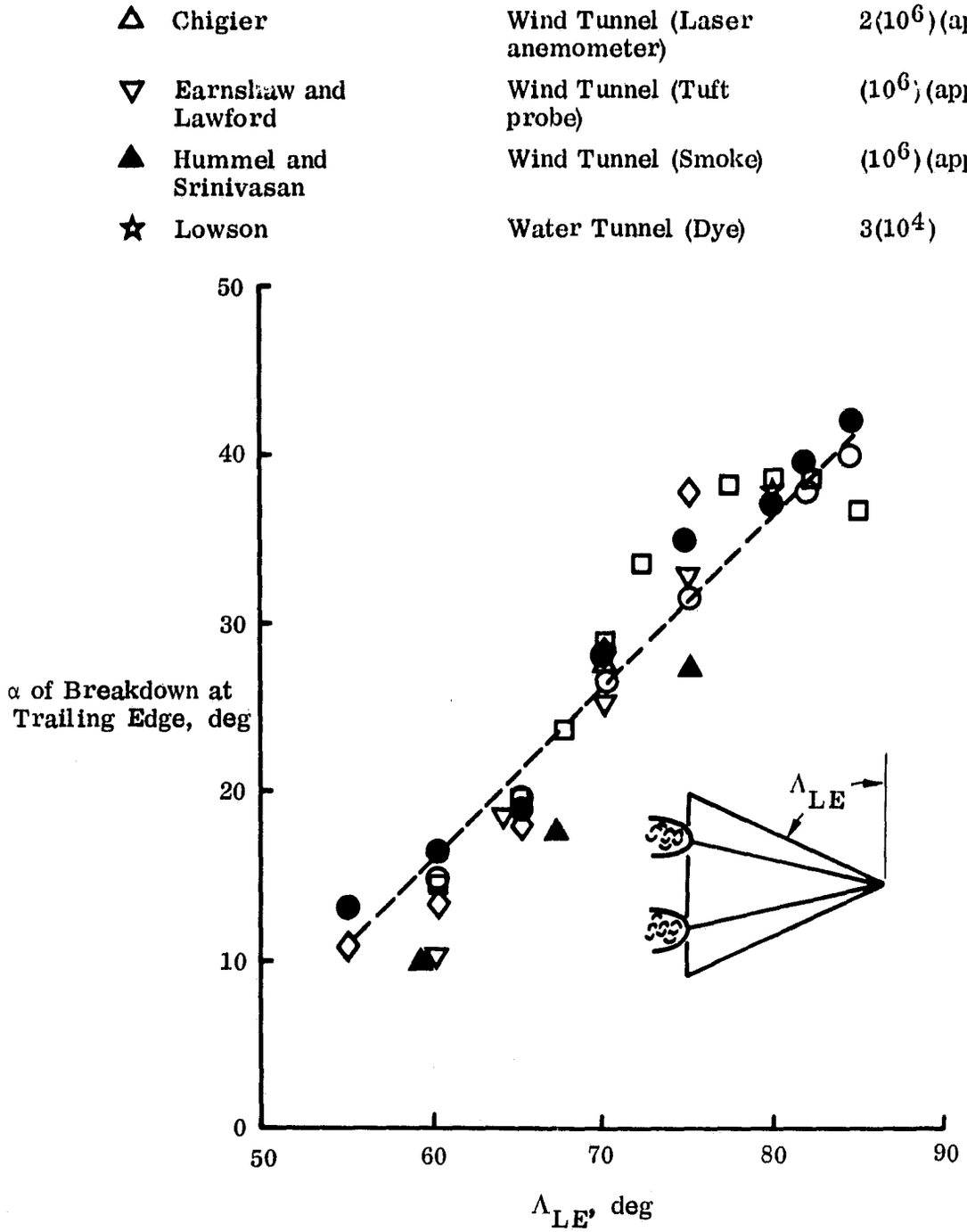

FIGURE 8. EFFECT OF LEADING-EDGE SWEEP ON THE ANGLE OF ATTACK OF VORTEX BREAKDOWN AT THE TRAILING EDGE OF DELTA WINGS (DATA FROM REFERENCE 6)

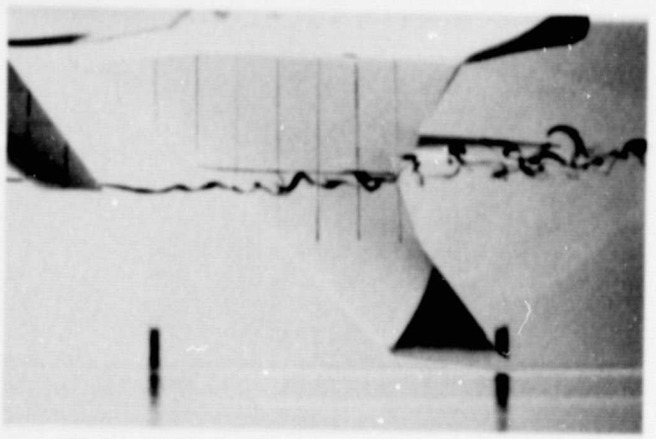

$\alpha = 5^{o}$

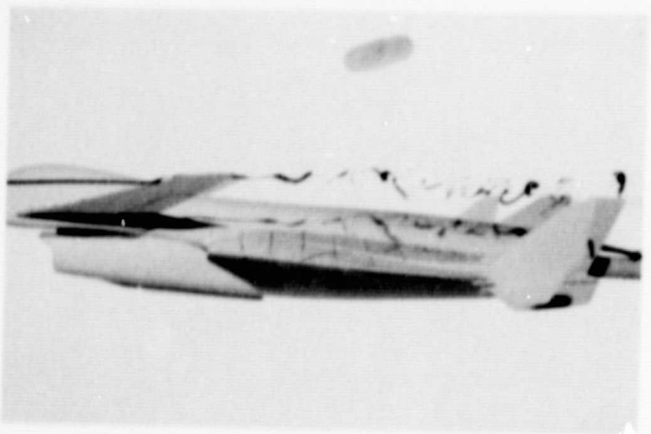

$\alpha = 5^{o}$

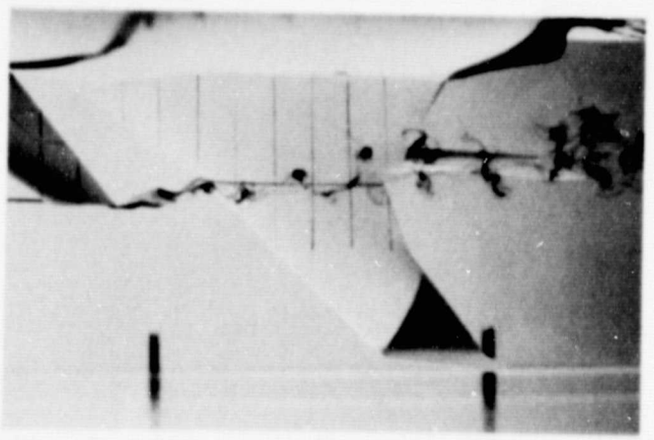

$\alpha = 8^{o}$

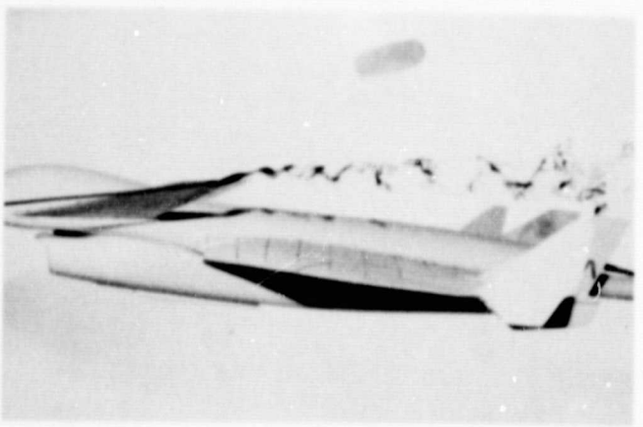

$\alpha = 8^{o}$

FIGURE 9. MANEUVER CANARD/VERTICAL TAIL INTERACTION AT $\beta = 0^{o}$

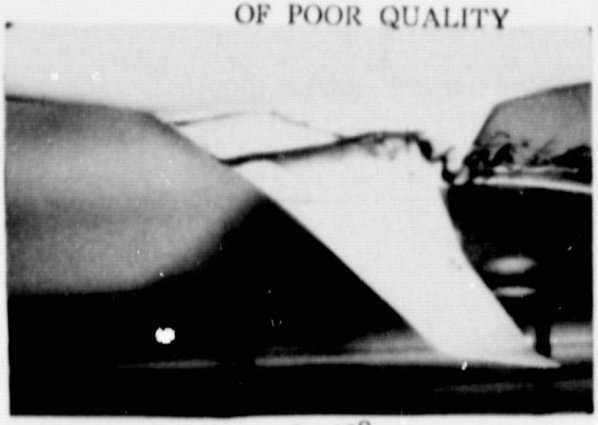

$\alpha = 10^{o}$

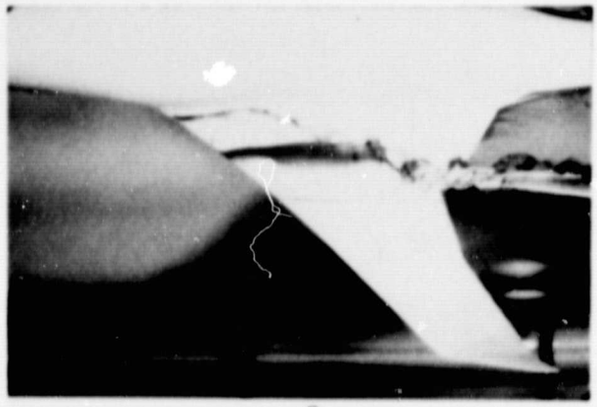

$\alpha = 12^{o}$

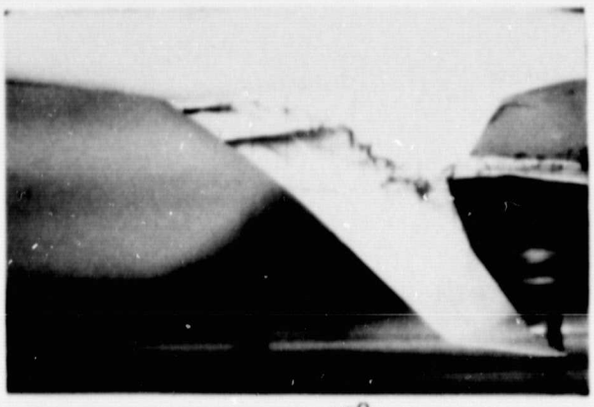

$\alpha = 15^{o}$

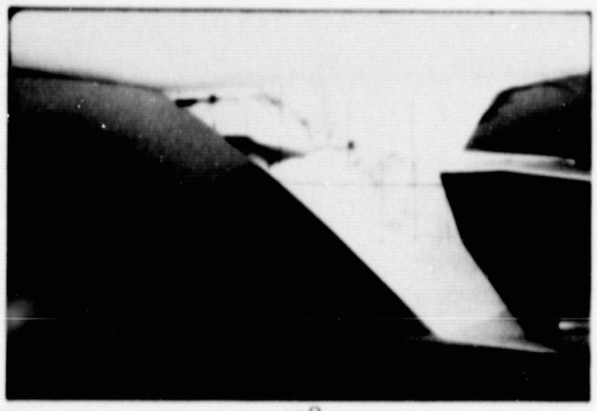

$\alpha = 18^{o}$

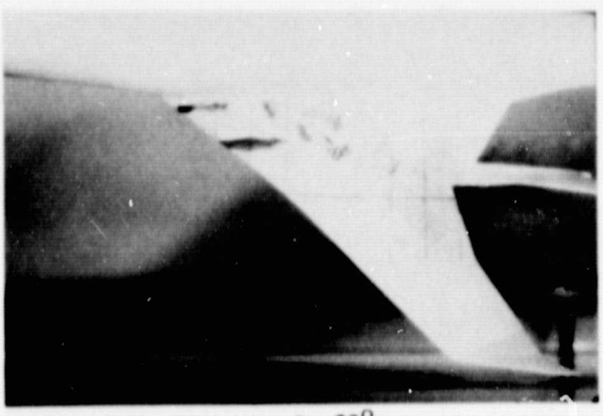

$\alpha = 20^{o}$

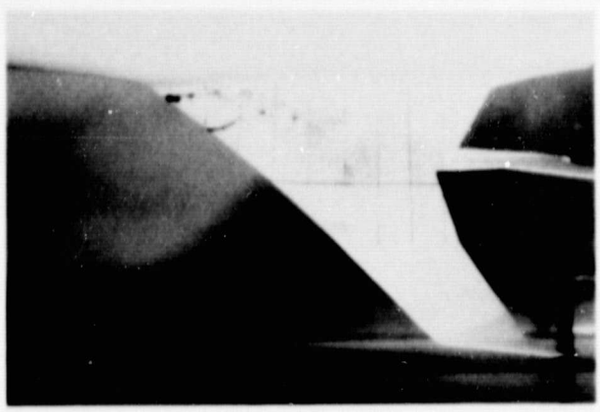

$\alpha = 25^{o}$

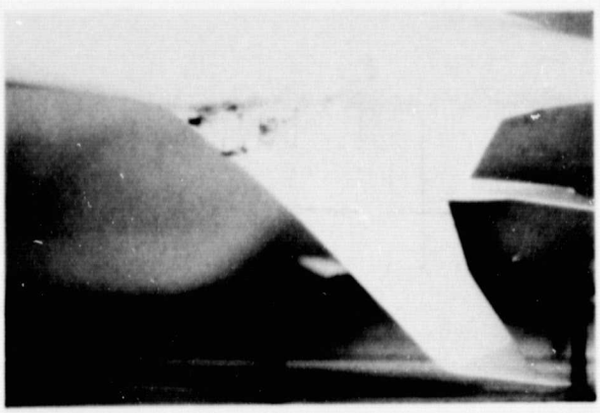

$\alpha = 30^{o}$

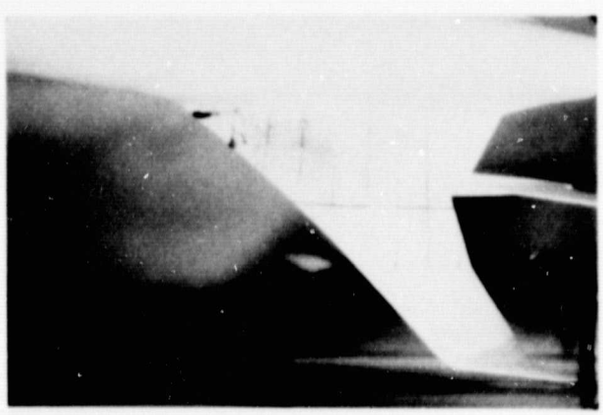

$\alpha = 35^{o}$

FIGURE 10. MANEUVER WING ALONE FLOW FIELD FOR $\beta = 0^{o}$

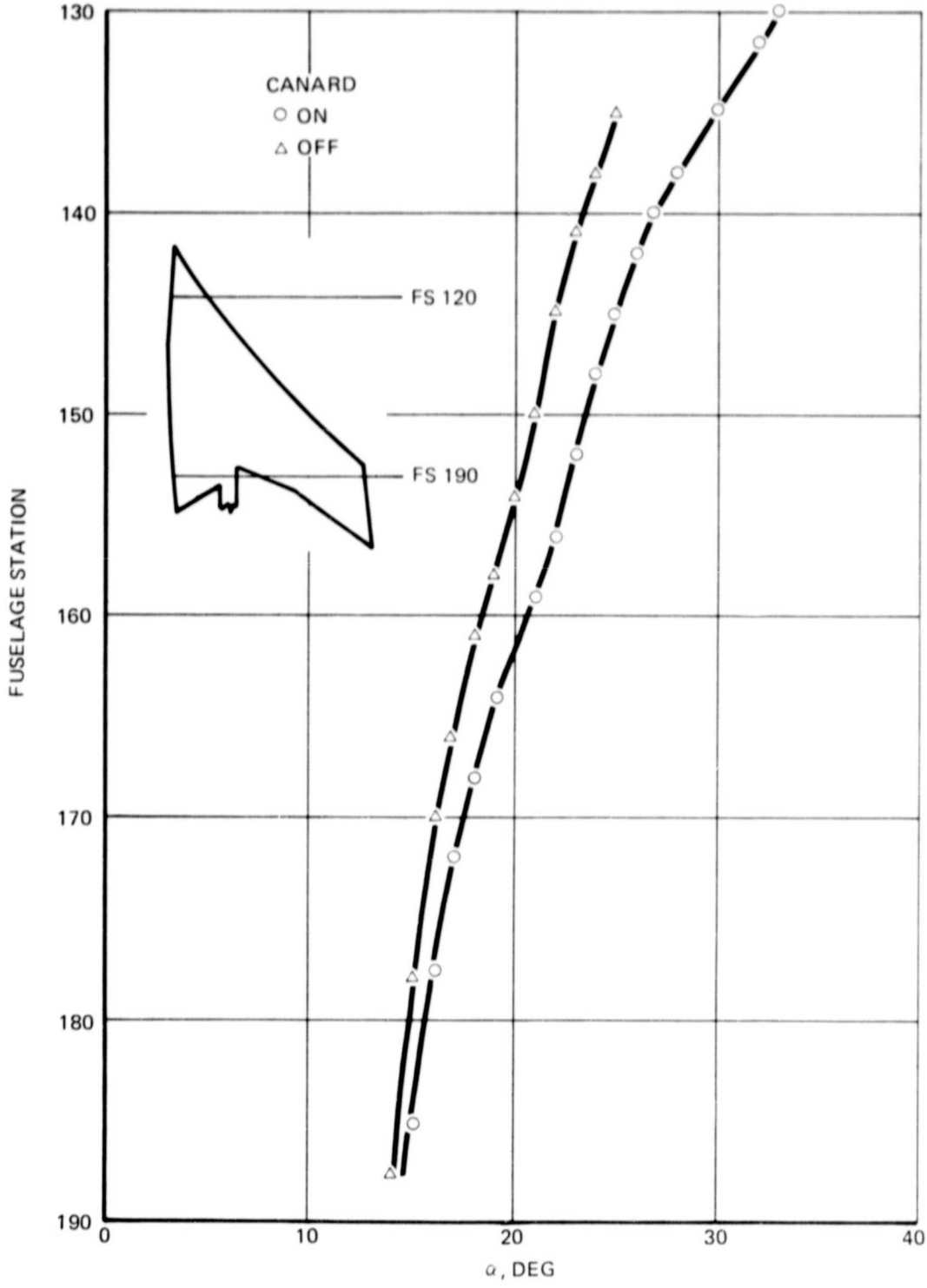

FIGURE 11. EFFECT OF MANEUVER CANARD ON VORTEX BREAKDOWN OF MANEUVER WING

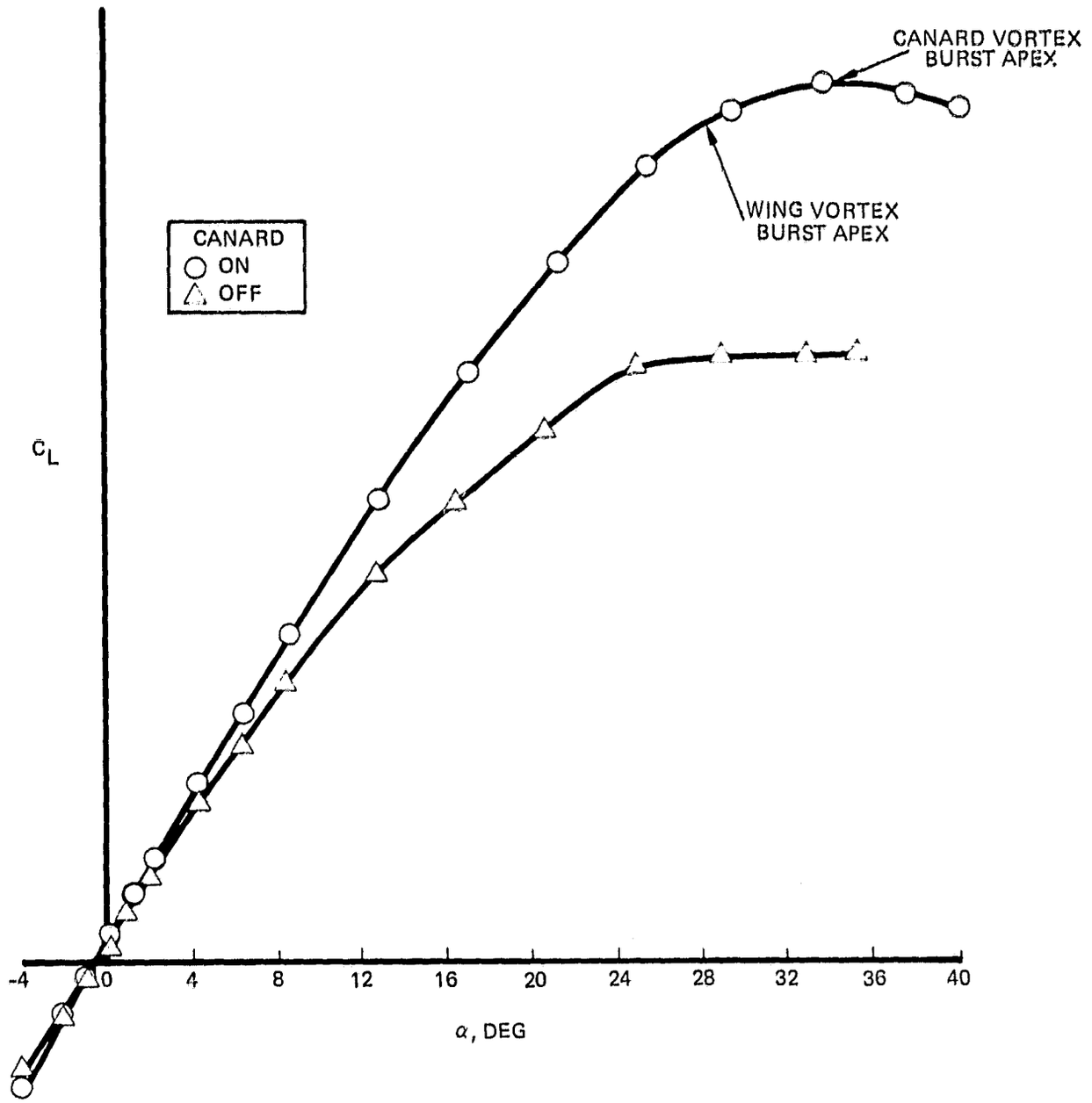

FIGURE 12. EFFECT OF CRUISE CANARD ON LIFT CHARACTERISTICS

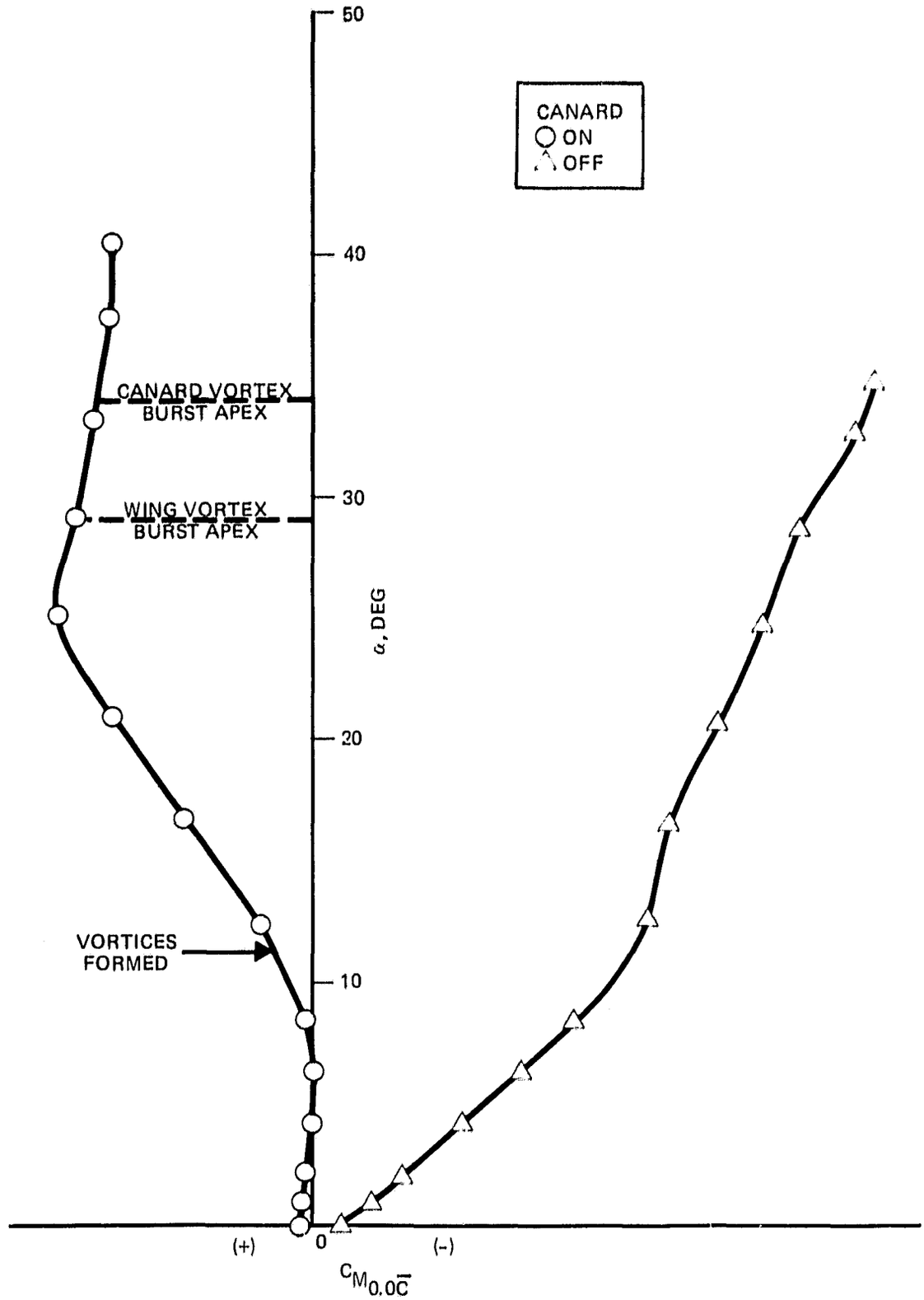

FIGURE 13. EFFECT OF CRUISE CANARD ON PITCHING MOMENT CHARACTERISTICS

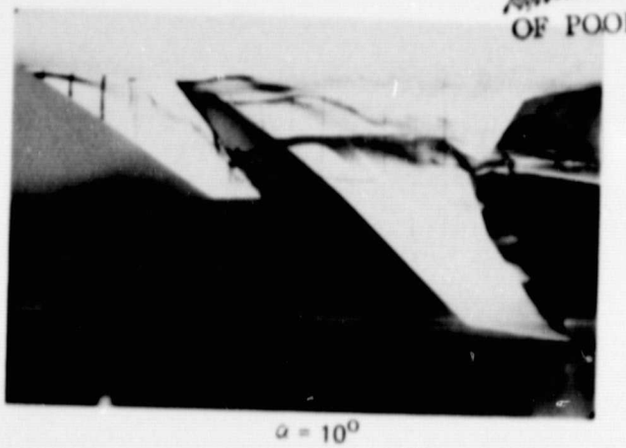

$\alpha = 10^{o}$

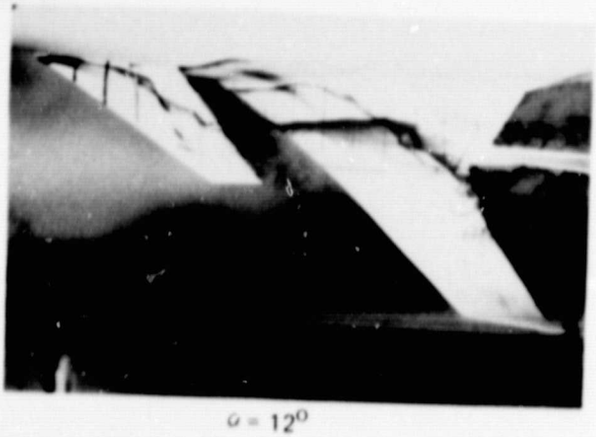

$\alpha = 12^{o}$

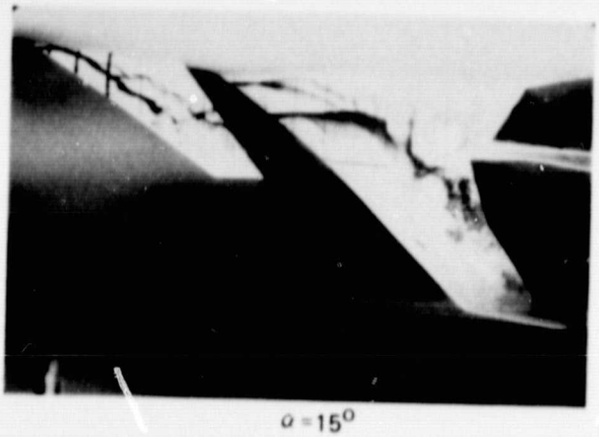

$\alpha = 15^{o}$

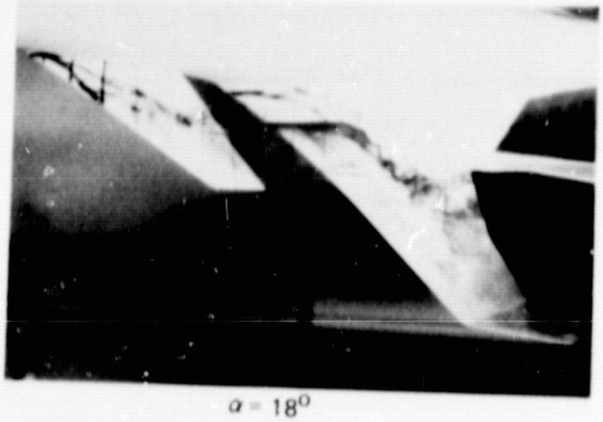

$\alpha = 18^{o}$

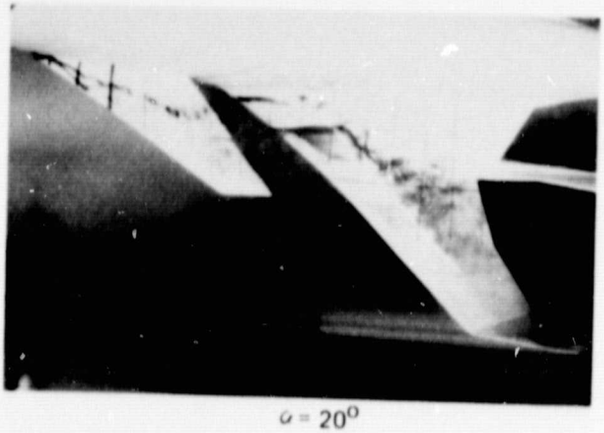

$\alpha = 20^{o}$

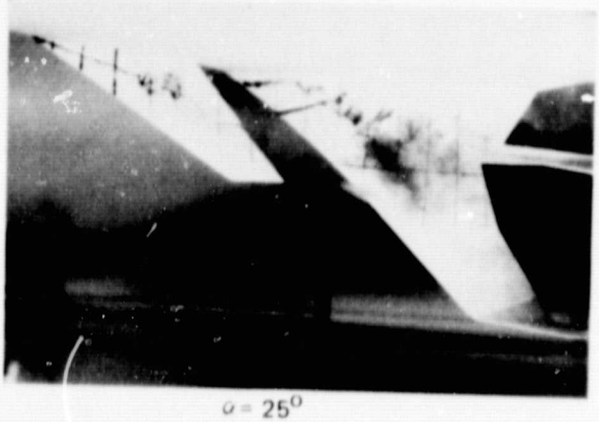

$\alpha = 25^{o}$

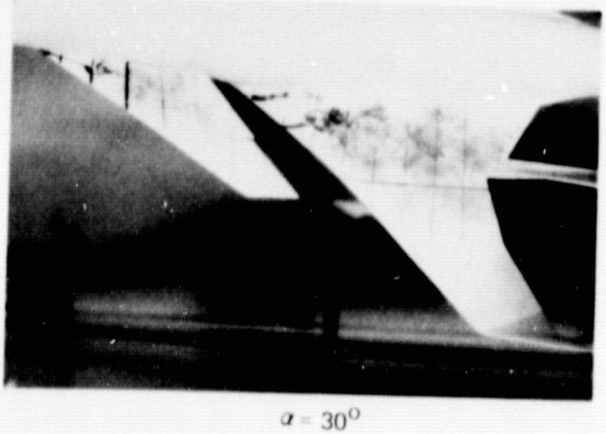

$\alpha = 30^{o}$

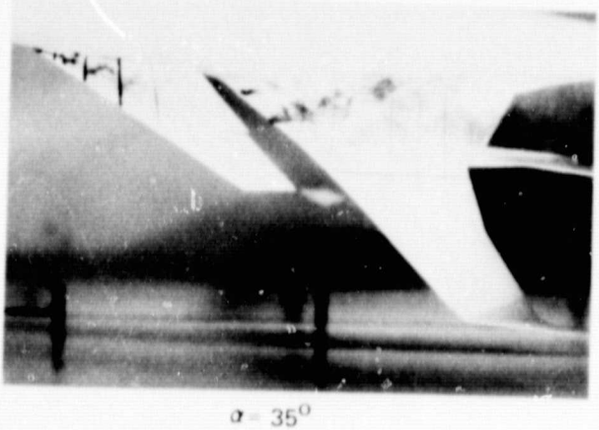

$\alpha = 35^{o}$

FIGURE 14. MANEUVER WING-CANARD FLOW FIELD FOR $\delta_f = -20^{o}$, $\beta = 0^{o}$

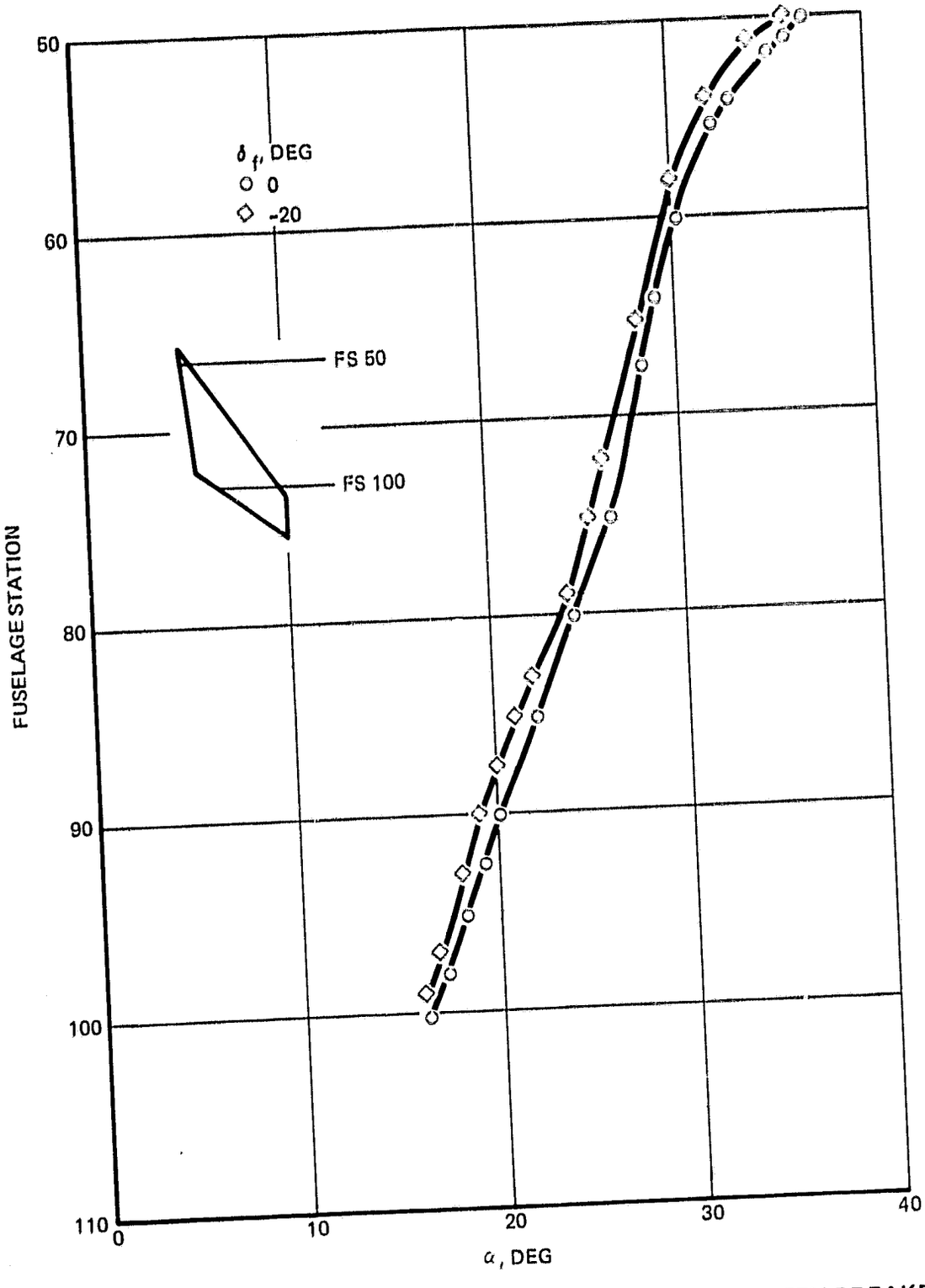

FIGURE 15. EFFECT OF TRAILING-EDGE FLAP DEFLECTION ON VORTEX BREAKDOWN OF MANEUVER CANARD

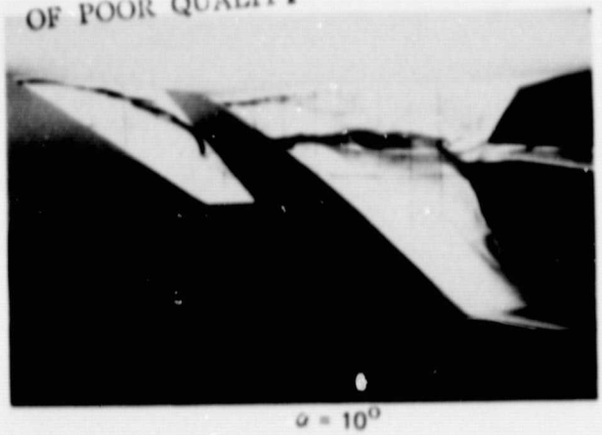

$\alpha = 10^{o}$

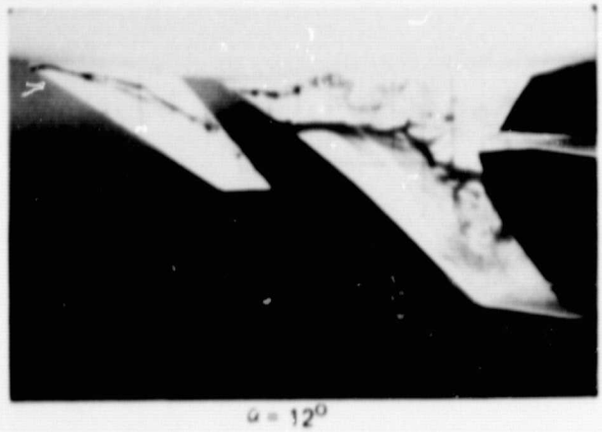

$\alpha = 12^{o}$

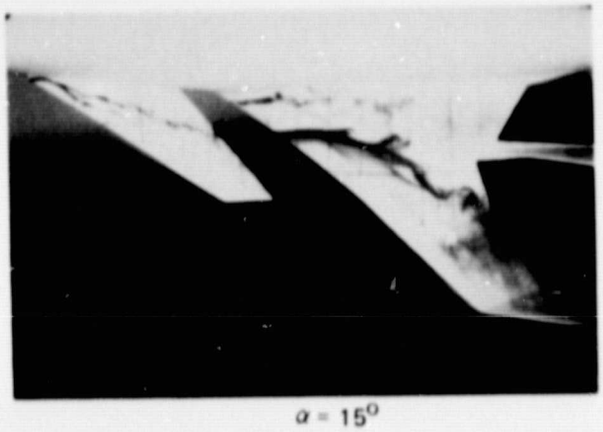

$\alpha = 15^{o}$

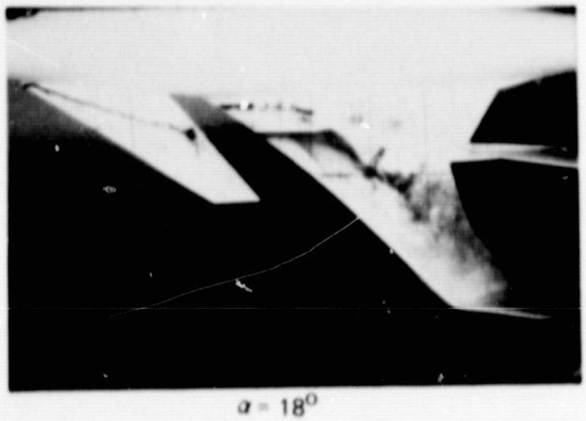

$\alpha = 18^{o}$

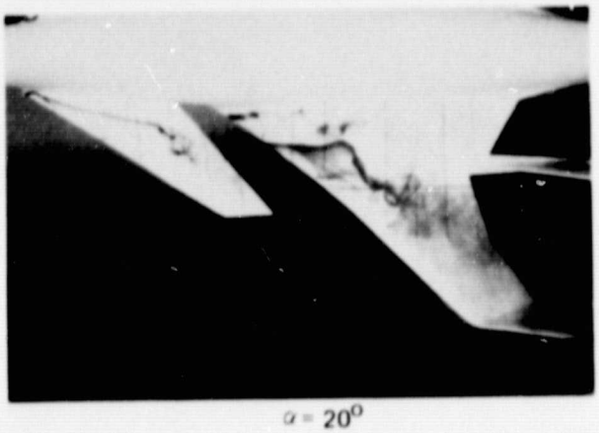

$\alpha = 20^{o}$

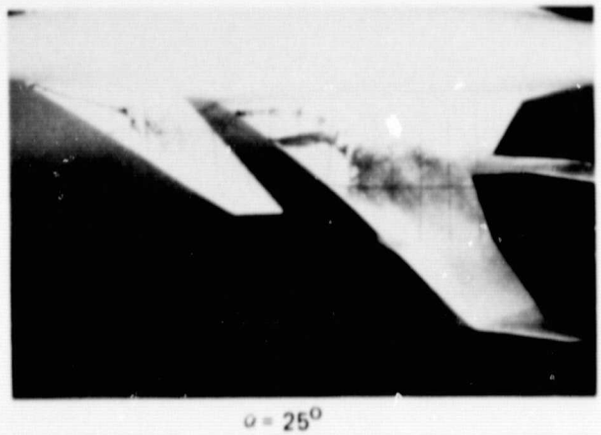

$\alpha = 25^{o}$

$\alpha = 30^{o}$

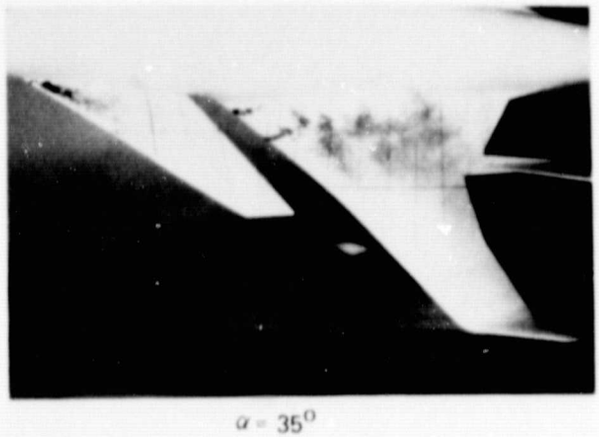

$\alpha = 35^{o}$

FIGURE 16. MANEUVER WING-CANARD FLOW FIELD FOR $\dot{m}_j = 0$, $\beta = 0^{o}$

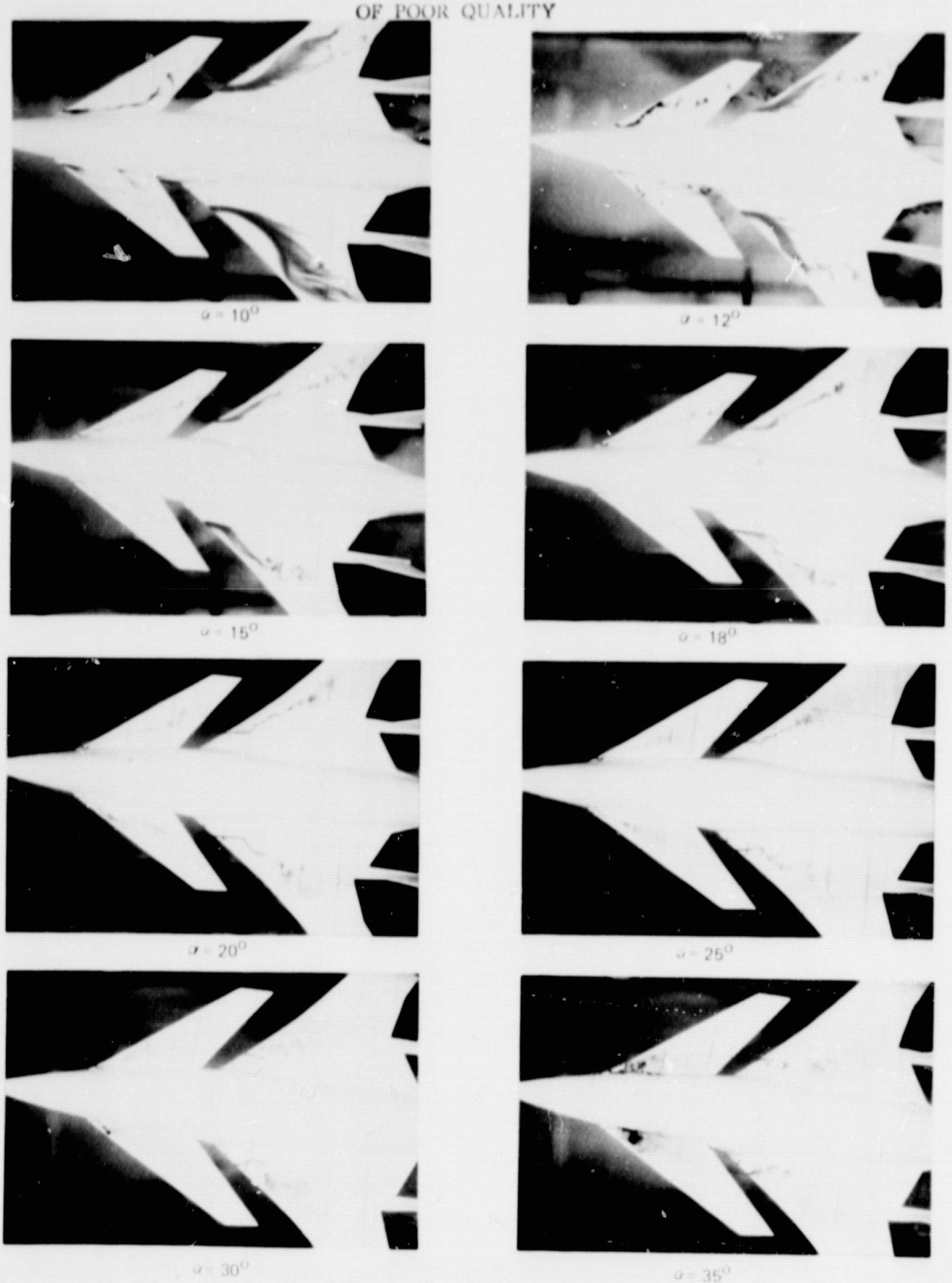

FIGURE 17. EFFECT OF SIDESLIP ON CRUISE WING-CANARD FLOW FIELD, $\beta = -5^{o}$

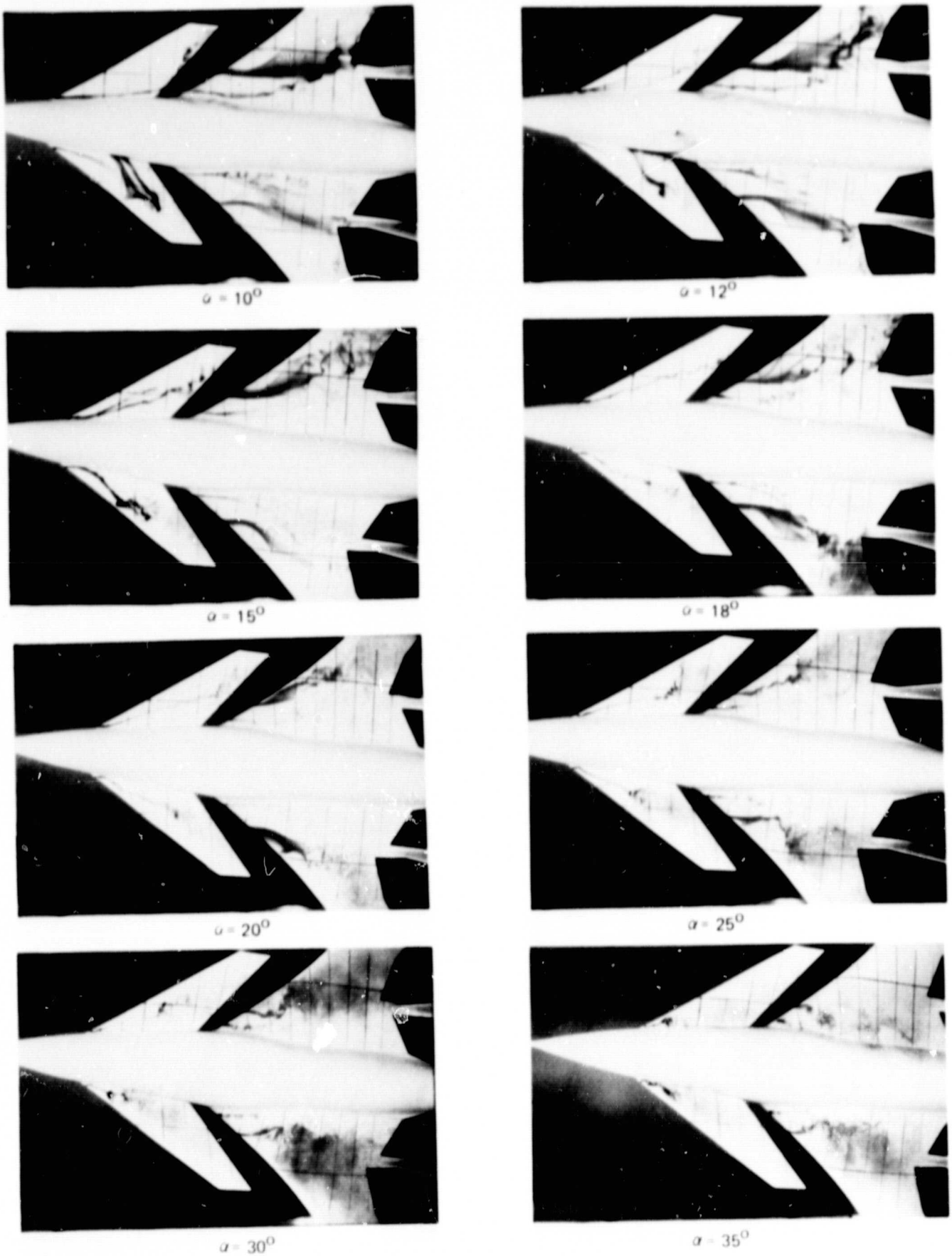

FIGURE 18. EFFECT OF SIDESLIP ON MANEUVER WING-CANARD FLOW FIELD, $\beta = -5^{o}$

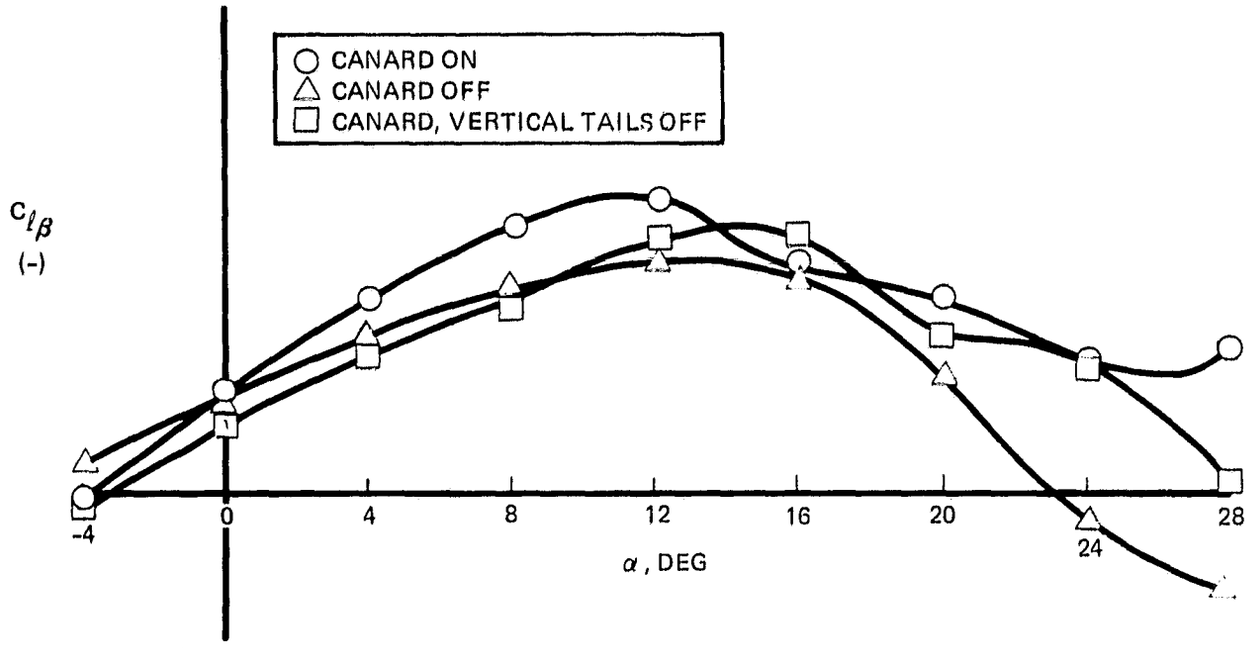

FIGURE 19. CRUISE WING LATERAL STABILITY CHARACTERISTICS

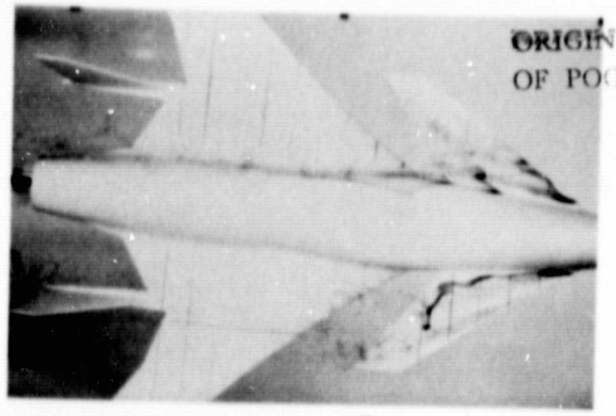

$\alpha = 10^{o}$

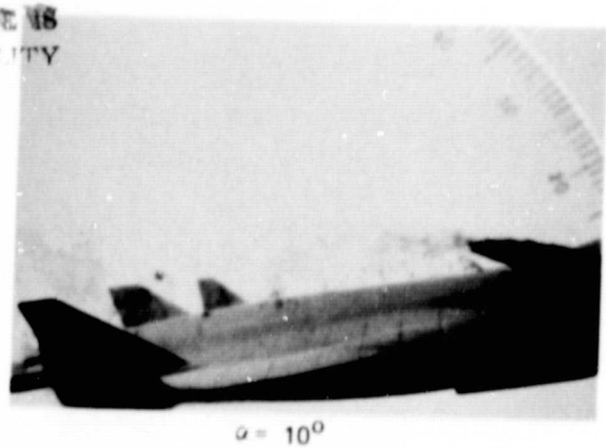

$\alpha = 10^{o}$

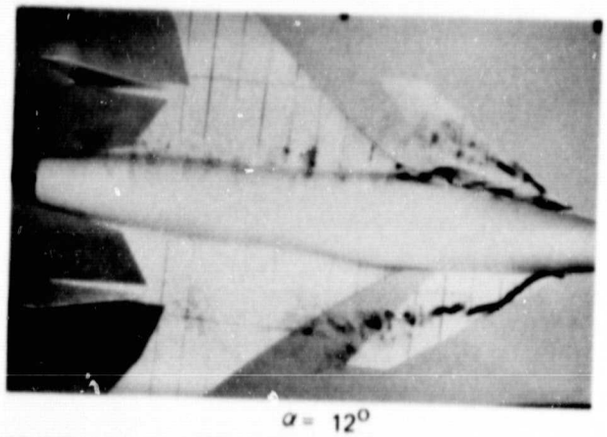

$\alpha = 12^{o}$

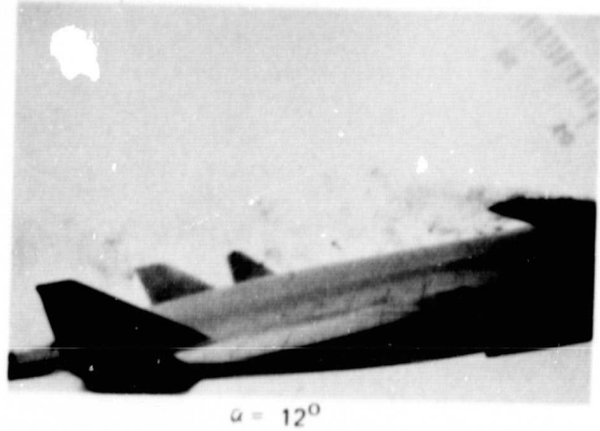

$\alpha = 12^{o}$

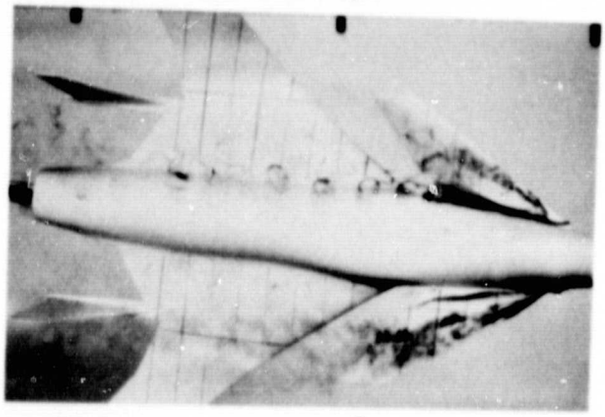

$\alpha = 15^{o}$

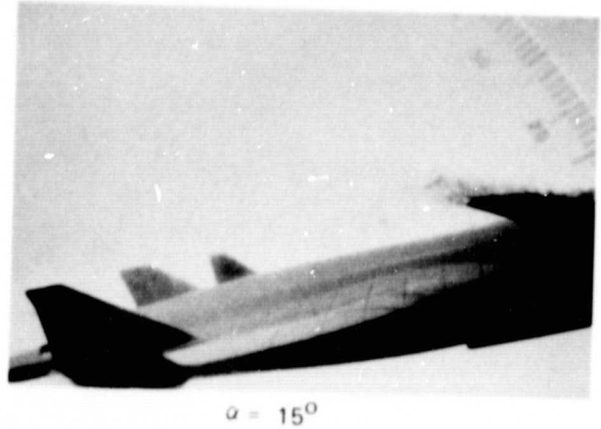

$\alpha = 15^{o}$

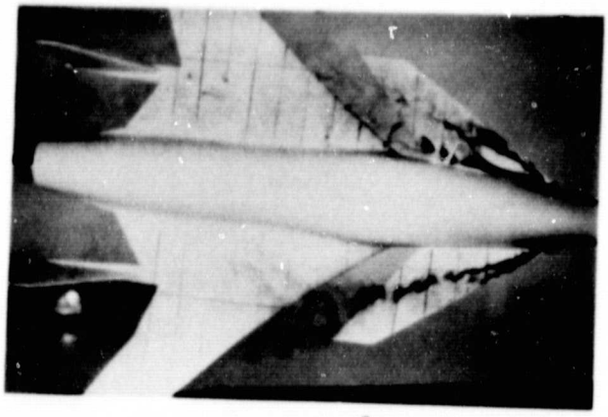

$\alpha = 18^{o}$

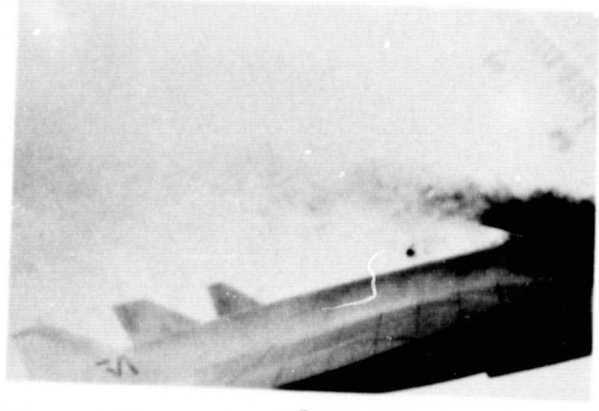

$\alpha = 18^{o}$

FIGURE 20. CRUISE CANARD/VERTICAL TAIL INTERACTION AT $\beta = -5^{o}$

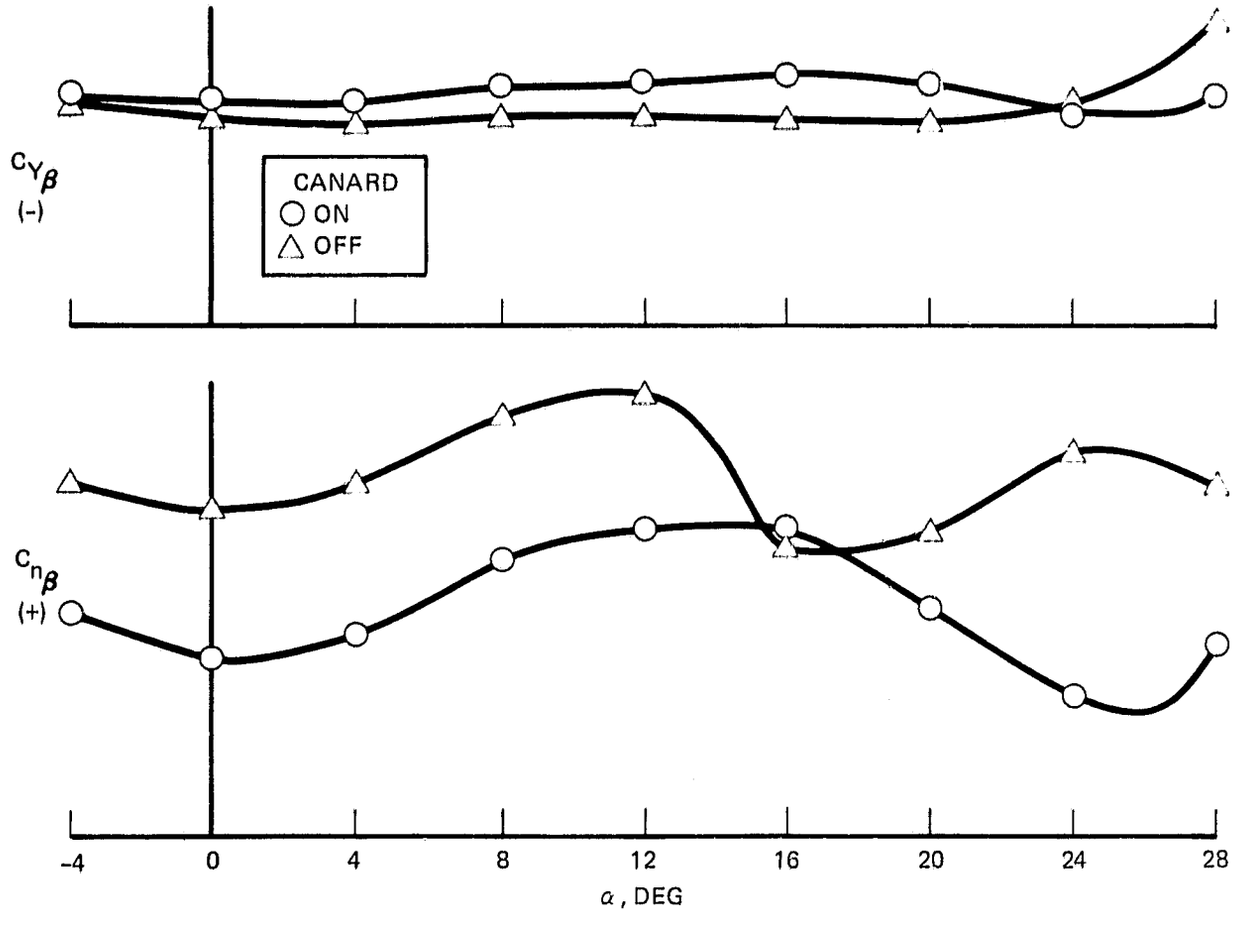

FIGURE 21. EFFECT OF CRUISE CANARD ON DIRECTIONAL STABILITY CHARACTERISTICS

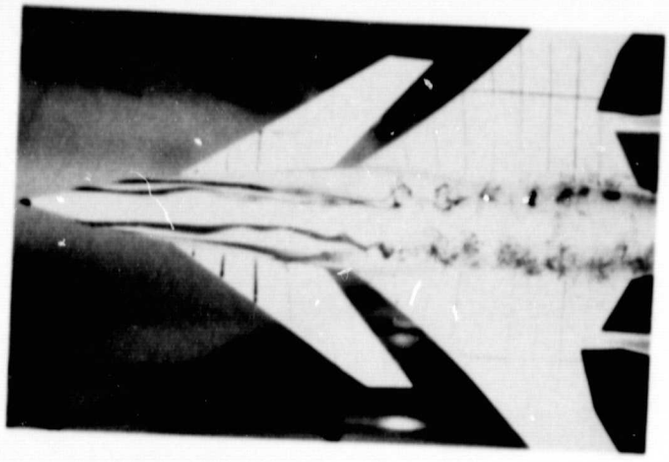

$\alpha = 20^{o}$

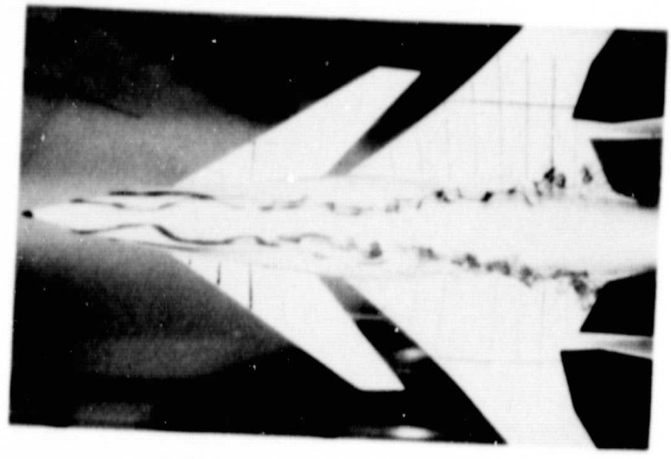

$\alpha = 25^{o}$

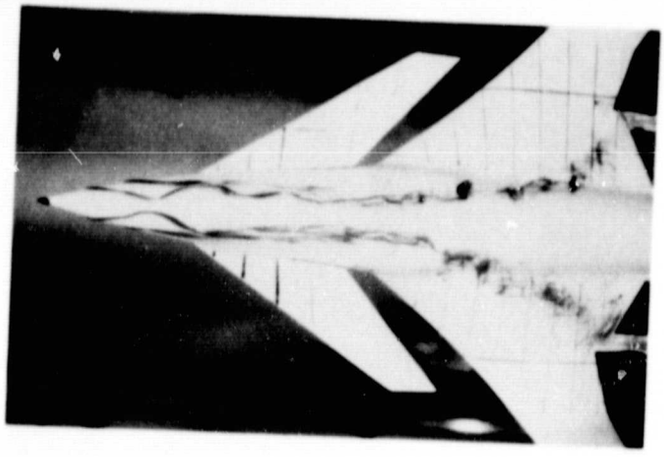

$\alpha = 28^{o}$

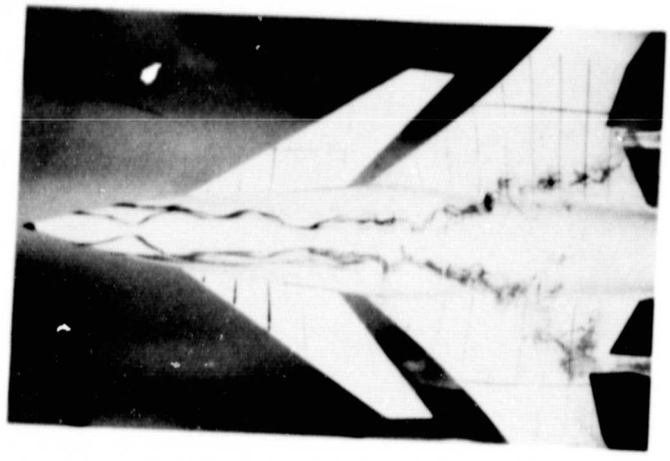

$\alpha = 30^{o}$

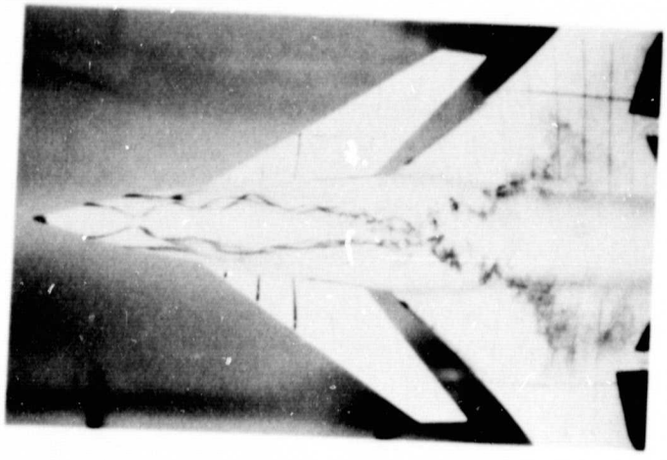

$\alpha = 35^{o}$

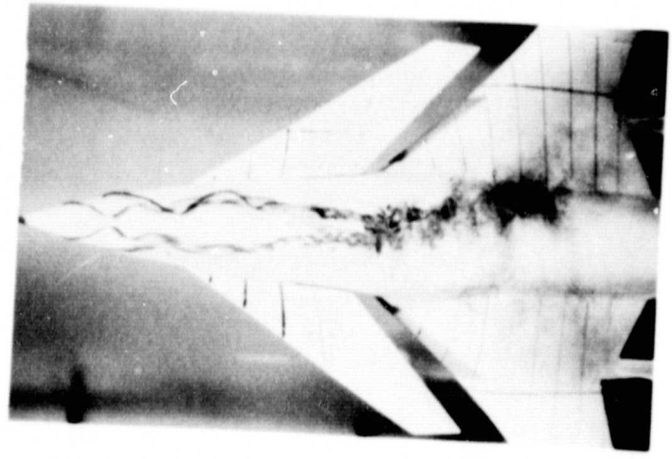

$\alpha = 40^{o}$

(A) PLAN VIEW

FIGURE 22. FOREBODY FLOW FIELD FOR $\beta = 0^{o}$

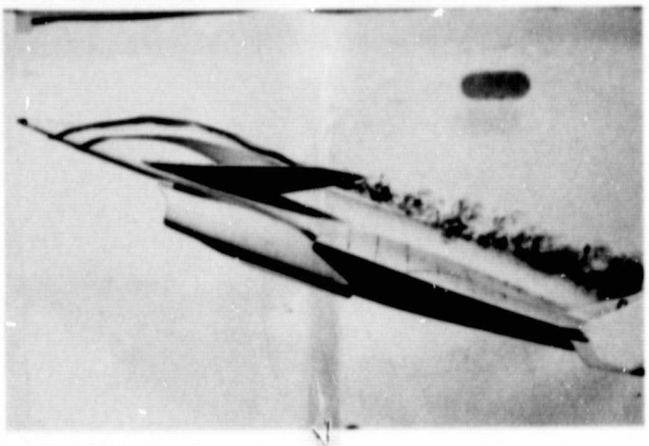

$\alpha = 20^{o}$

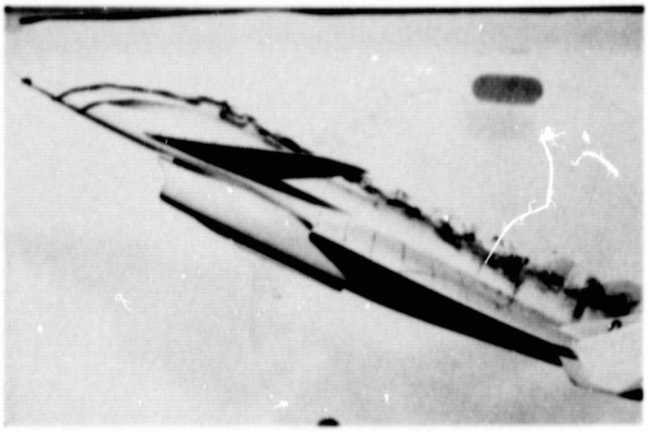

$\alpha = 25^{o}$

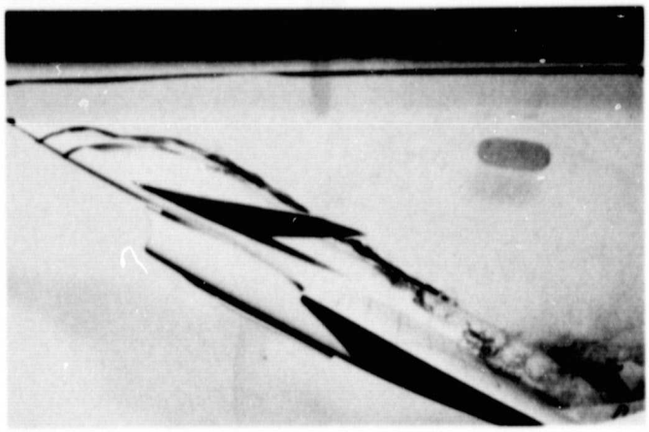

$\alpha = 28^{o}$

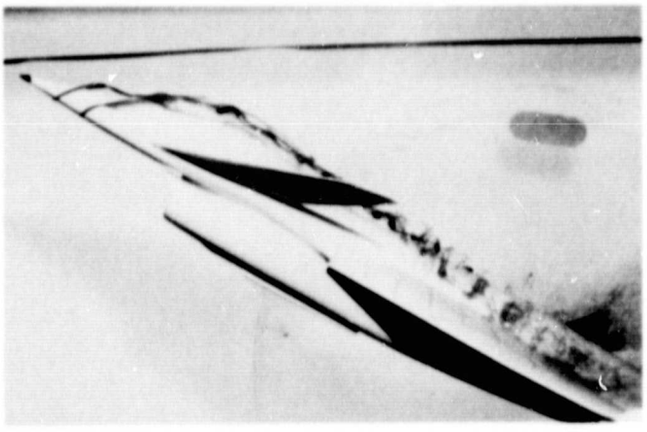

$\alpha = 30^{o}$

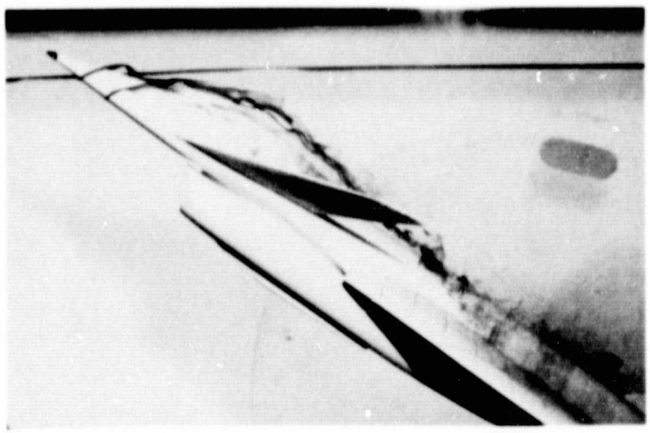

$\alpha = 35^{o}$

(B) PROFILE VIEW

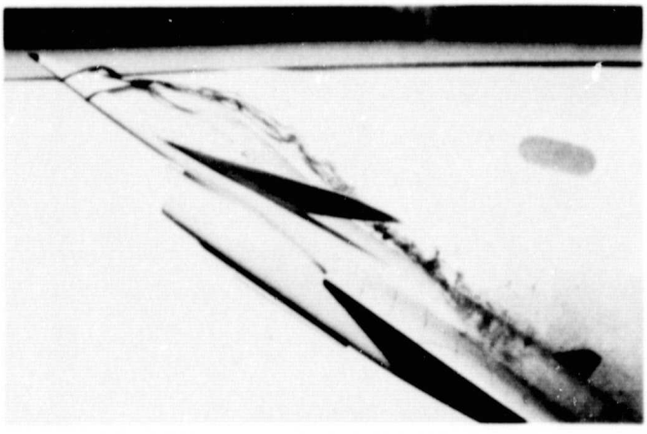

$\alpha = 40^{o}$

FIGURE 22. CONCLUDED

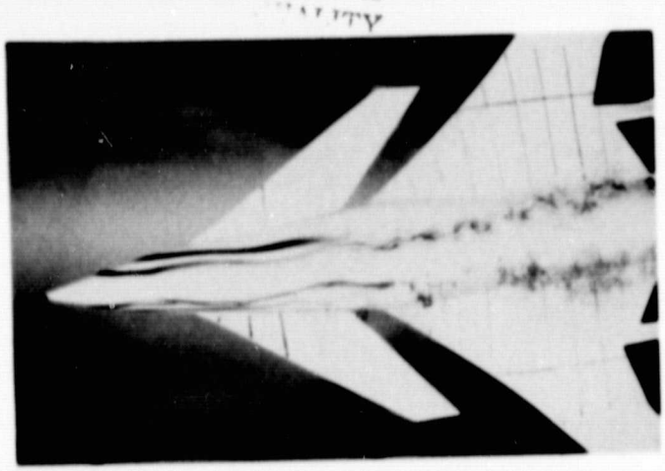

$\alpha = 20^{o}$

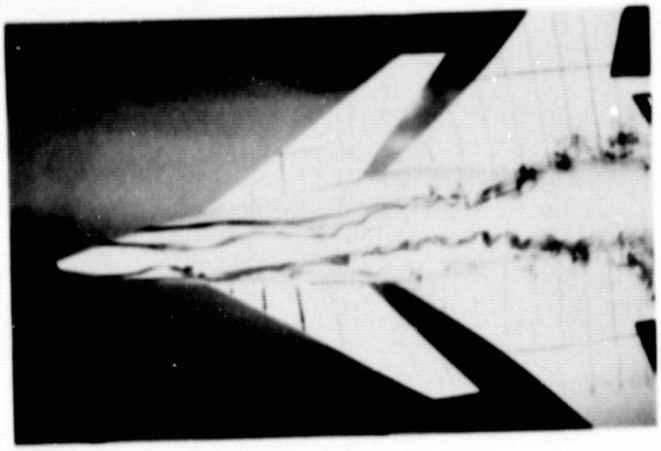

$\alpha = 25^{o}$

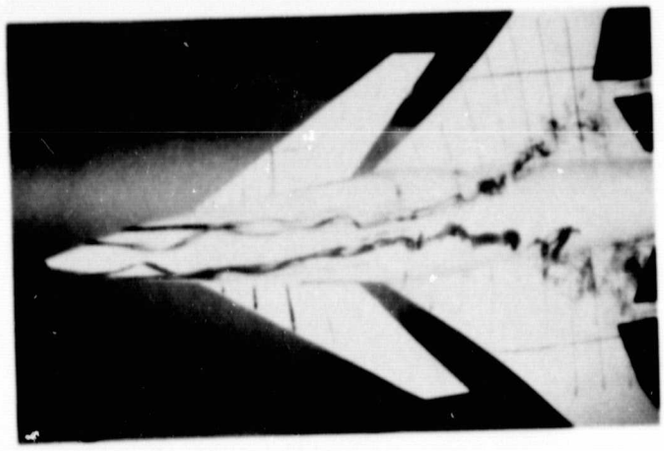

$\alpha = 28^{o}$

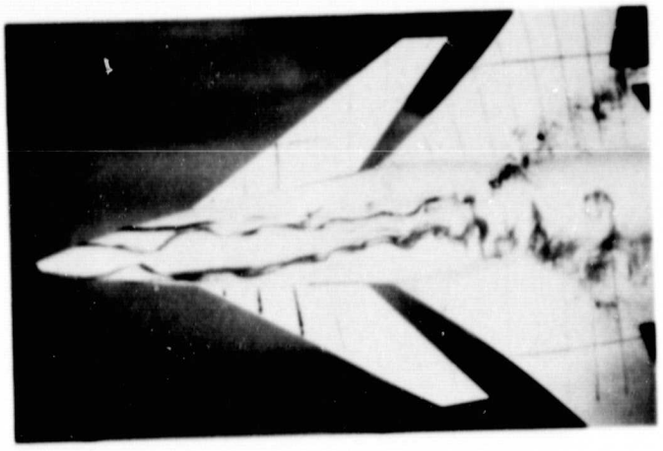

$\alpha = 30^{o}$

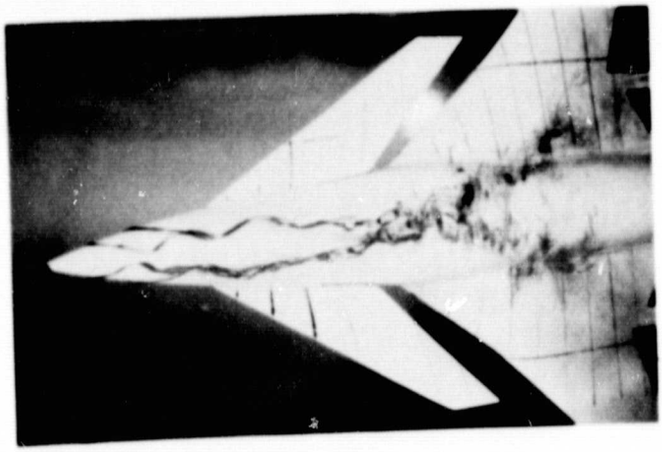

$\alpha = 35^{o}$

(A) PLAN VIEW

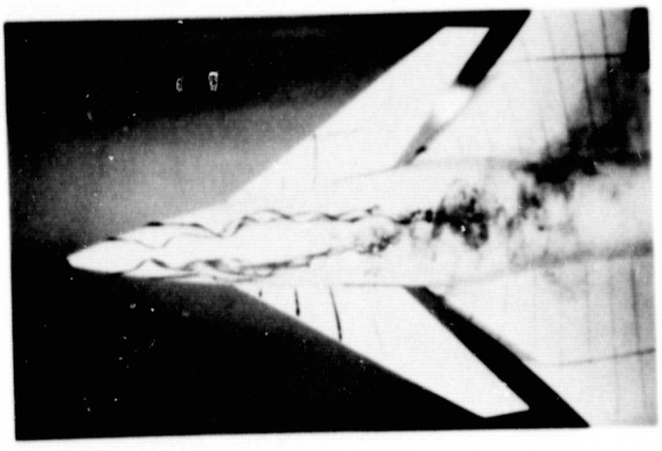

$\alpha = 40^{o}$

FIGURE 23. FOREBODY FLOW FIELD FOR $\beta = 5^{o}$

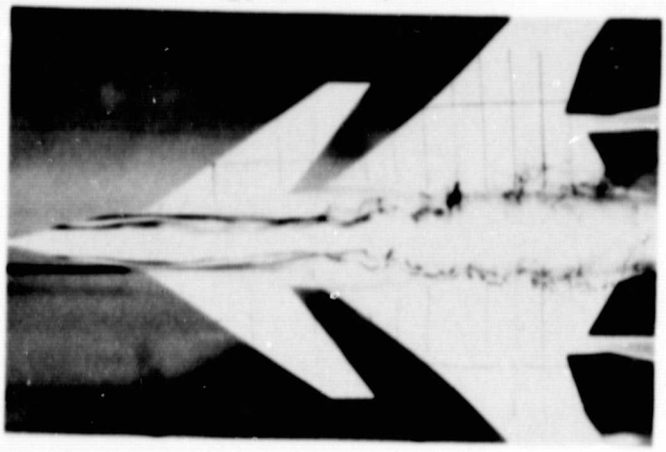

$\alpha = 20^{o}$

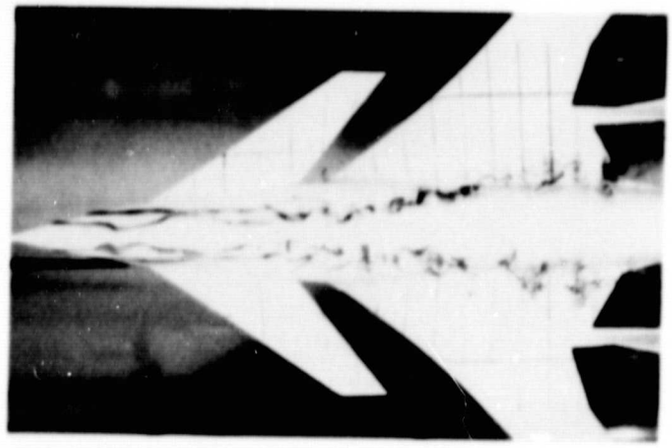

$\alpha = 25^{o}$

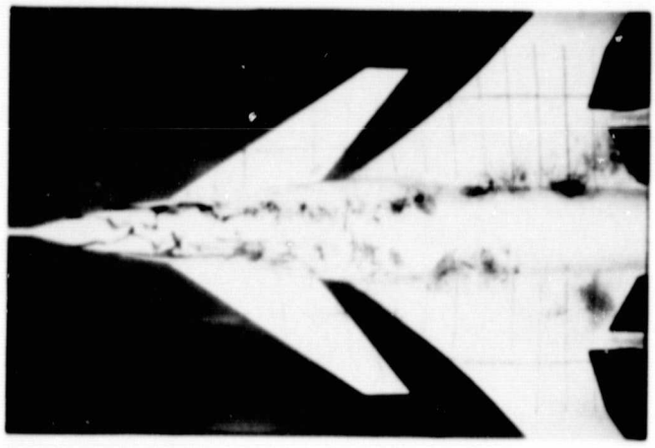

$\alpha = 28^{o}$

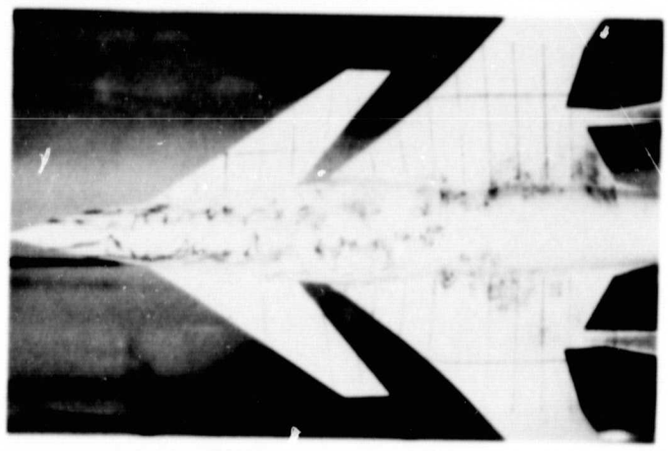

$\alpha = 30^{o}$

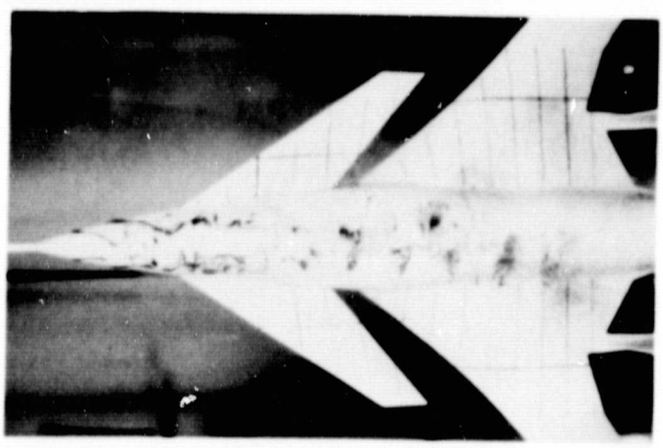

$\alpha = 35^{o}$

(A) PLAN VIEW

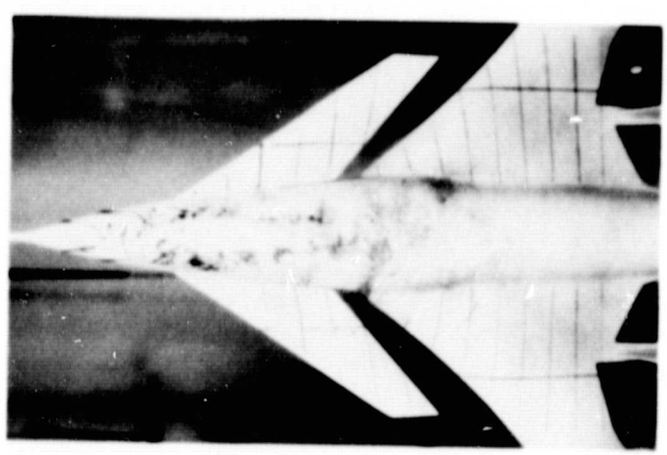

$\alpha = 40^{o}$

FIGURE 24. EFFECT OF NOSE BOOM ON FOREBODY FLOW FIELD FOR $\beta = 0^{o}$

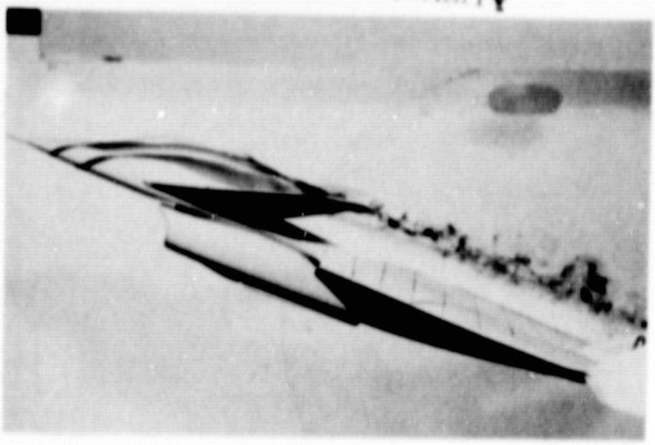

$\alpha = 18^{o}$

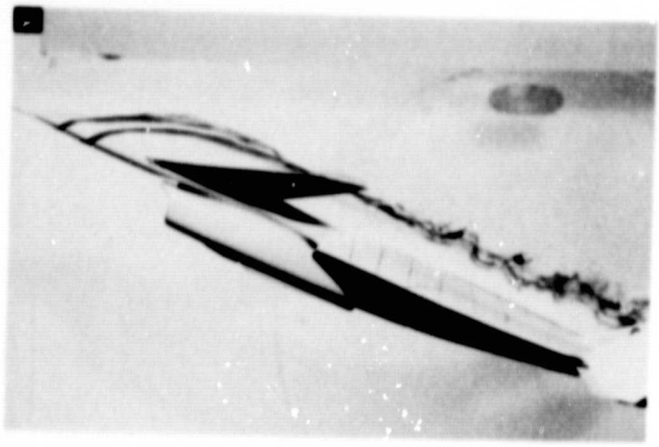

$\alpha = 20^{o}$

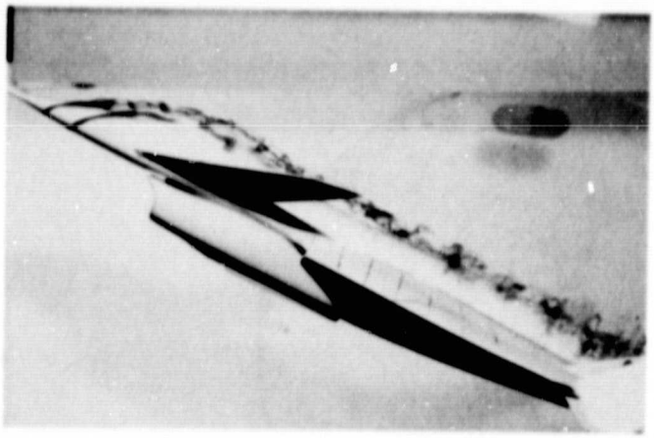

$\alpha = 25^{o}$

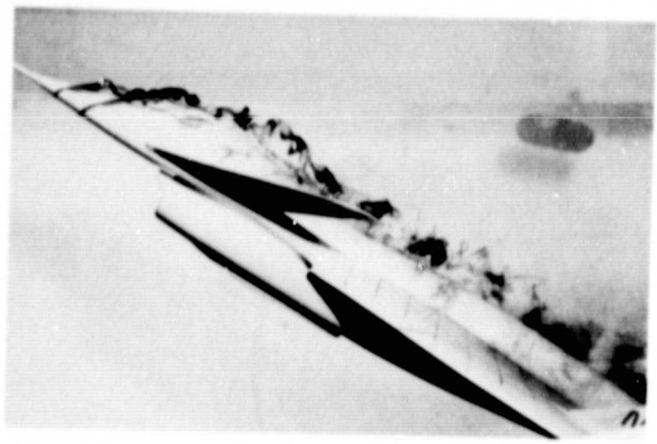

$\alpha = 30^{o}$

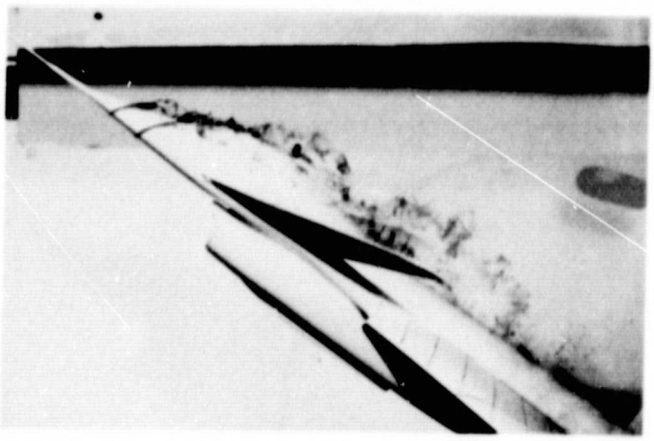

$\alpha = 35^{o}$

(B) PROFILE VIEW

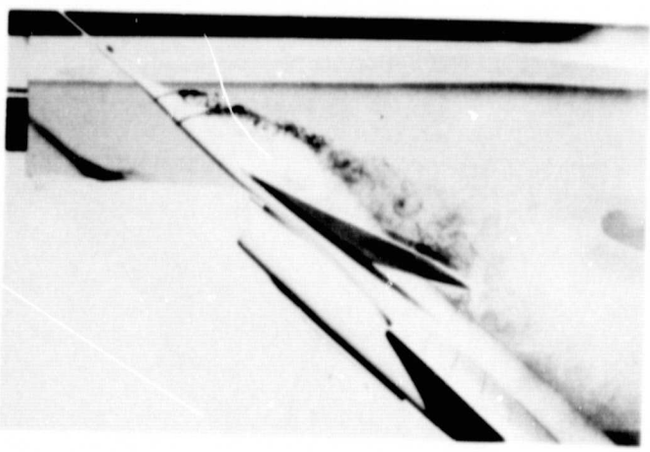

$\alpha = 40^{o}$

FIGURE 24. CONCLUDED

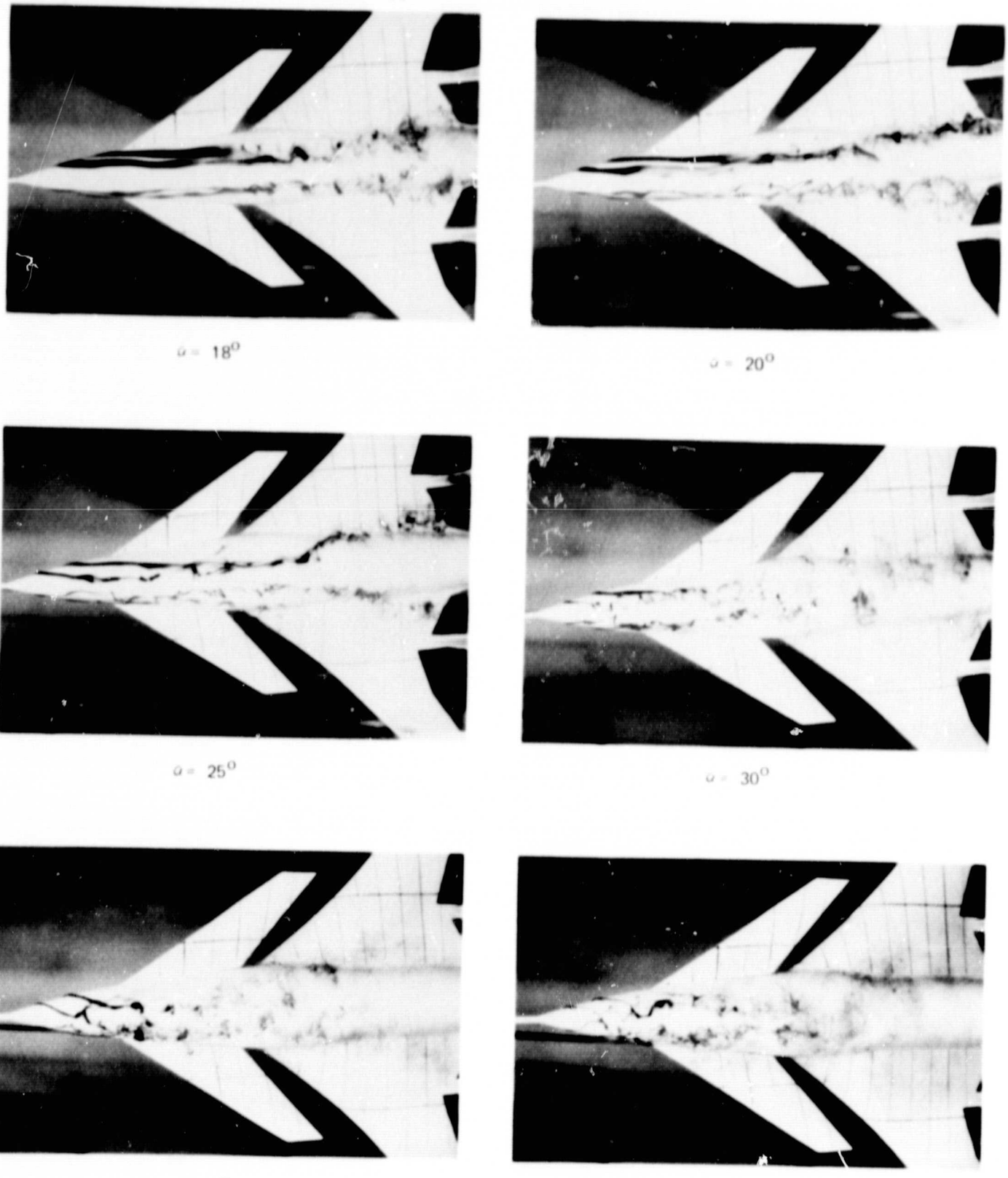

$\alpha = 18^{o}$ $\alpha = 20^{o}$

$\alpha = 25^{o}$ $\alpha = 30^{o}$

$\alpha = 35^{o}$ $\alpha = 40^{o}$

(A) PLAN VIEW

FIGURE 25. EFFECT OF NOSE BOOM ON FOREBODY FLOW FIELD FOR $\beta = 5^{o}$

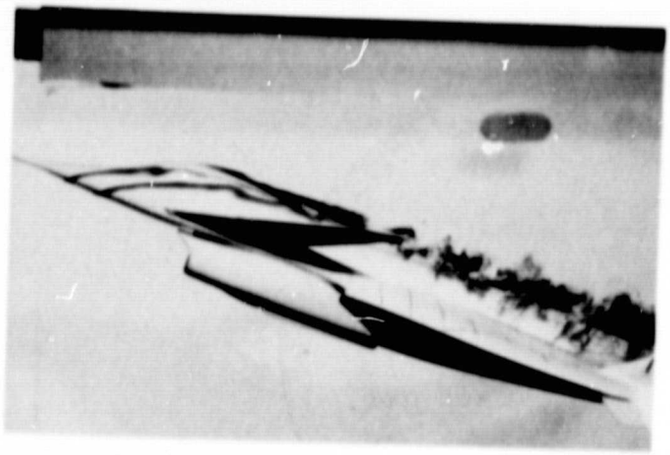

$\alpha = 18^{\circ}$

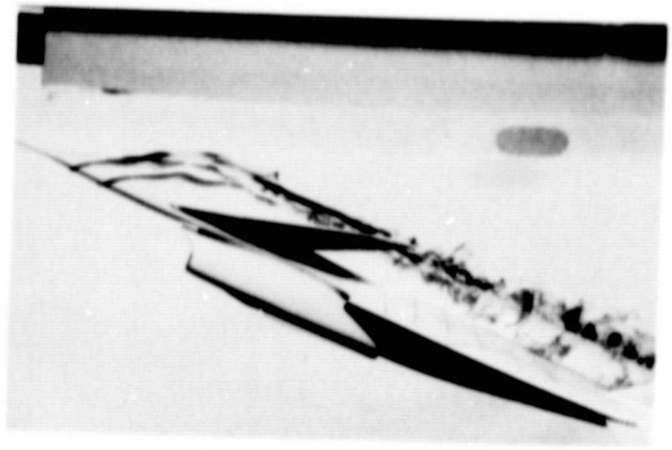

$\alpha = 20^{\circ}$

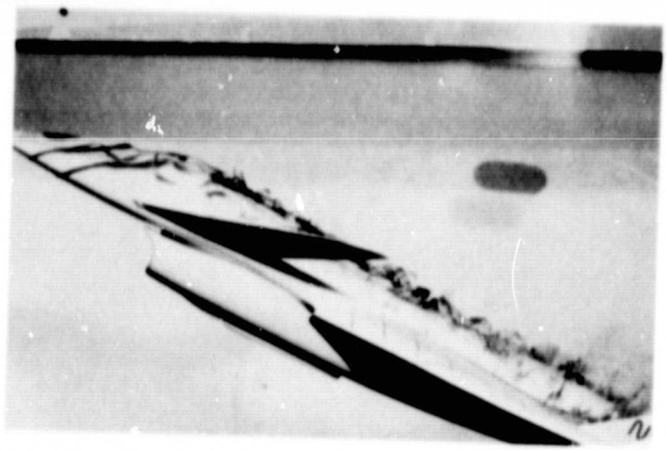

$\alpha = 25^{\circ}$

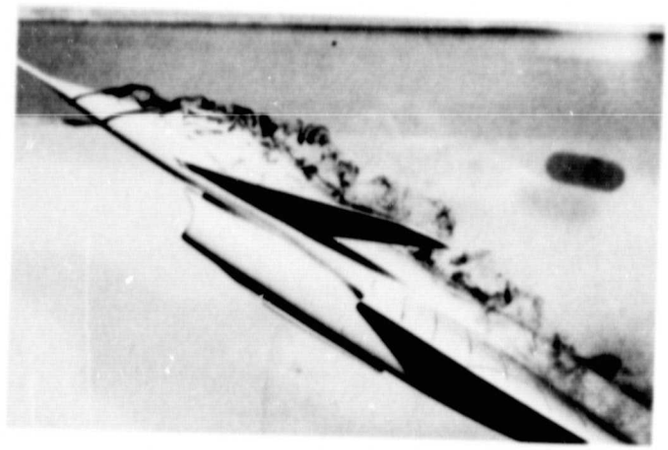

$\alpha = 30^{\circ}$

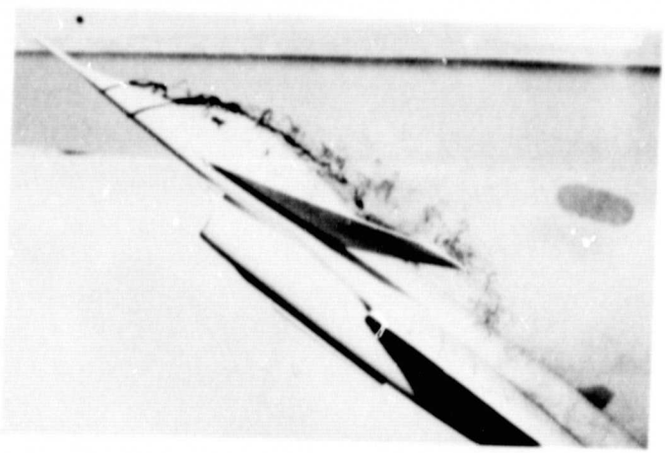

$\alpha = 35^{\circ}$

(B) LEEWARD PROFILE VIEW

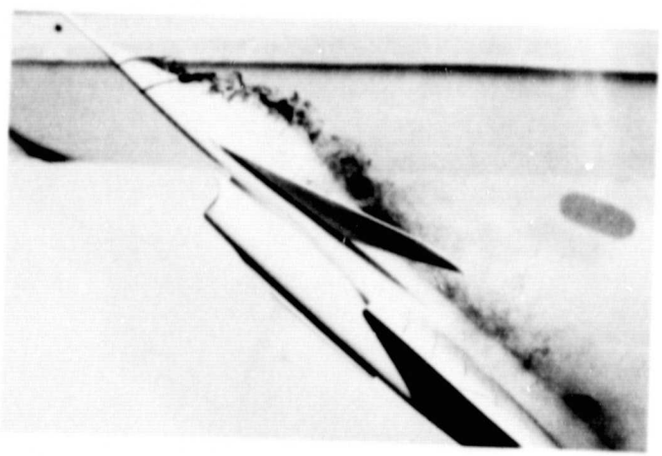

$\alpha = 40^{\circ}$

FIGURE 25. CONCLUDED

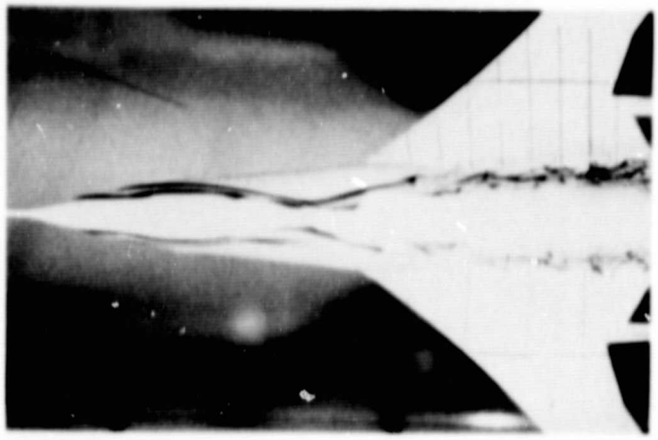

$\alpha = 18^{o}$

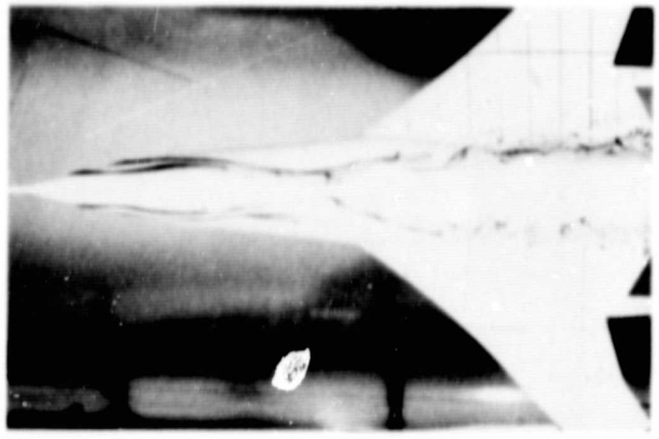

$\alpha = 20^{o}$

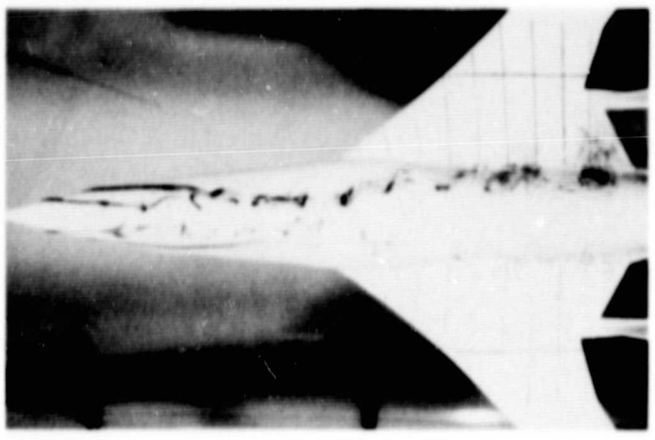

$\alpha = 25^{o}$

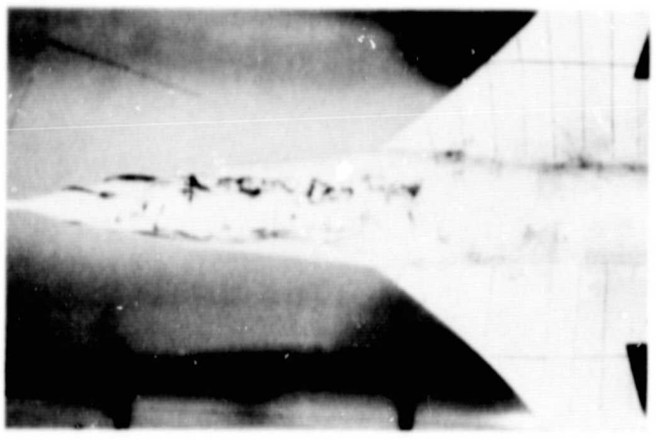

$\alpha = 30^{o}$

$\alpha = 35^{o}$

(A) PLAN VIEW

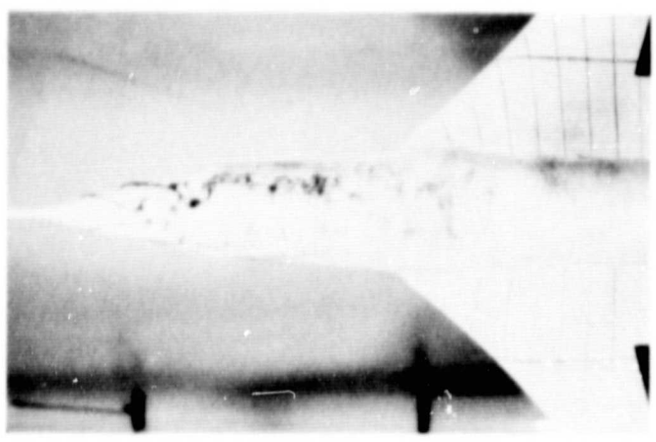

$\alpha = 40^{o}$

FIGURE 26. FOREBODY FLOW FIELD WITHOUT CANARD FOR $\beta = 0^{o}$

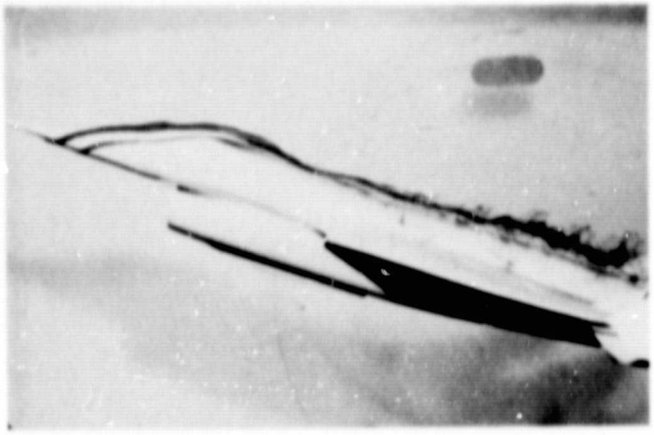

$\alpha = 18^{\circ}$

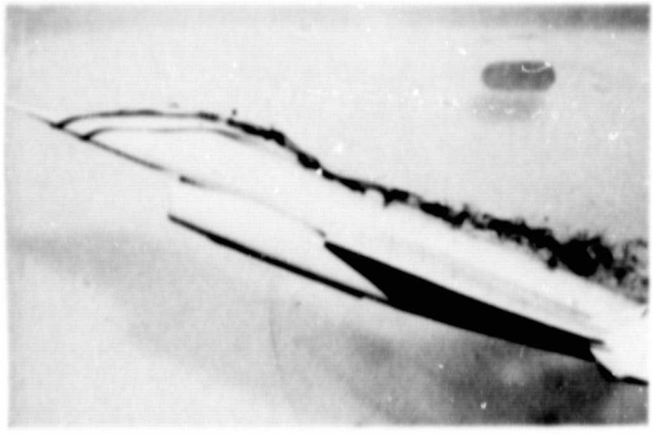

$\alpha = 20^{\circ}$

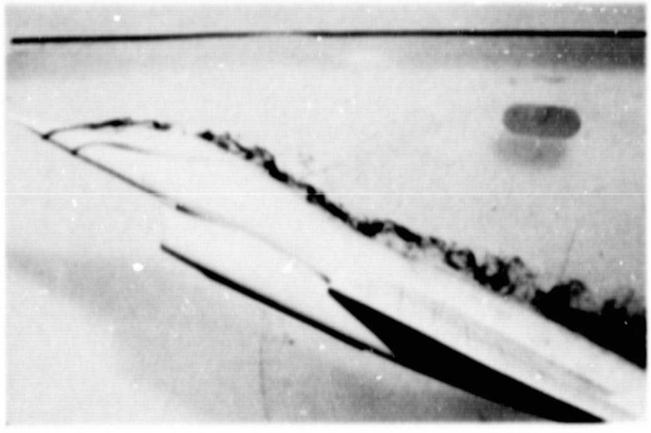

$\alpha = 25^{\circ}$

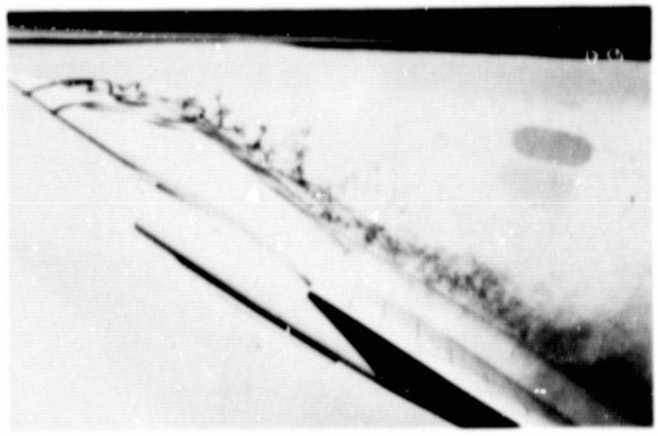

$\alpha = 30^{\circ}$

$\alpha = 35^{\circ}$

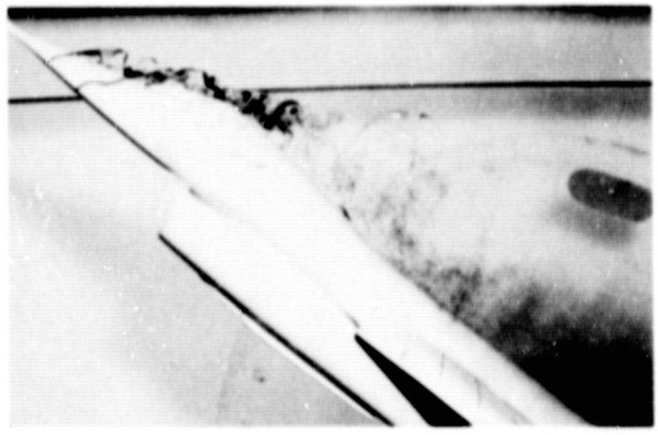

$\alpha = 40^{\circ}$

(B) PROFILE VIEW

FIGURE 26. CONCLUDED

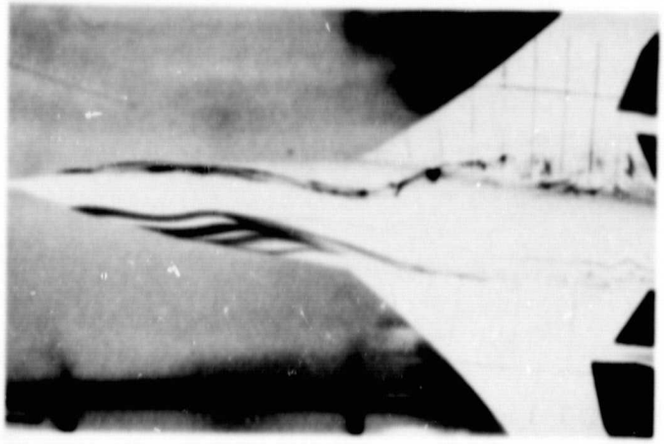

$\alpha = 18^{\circ}$

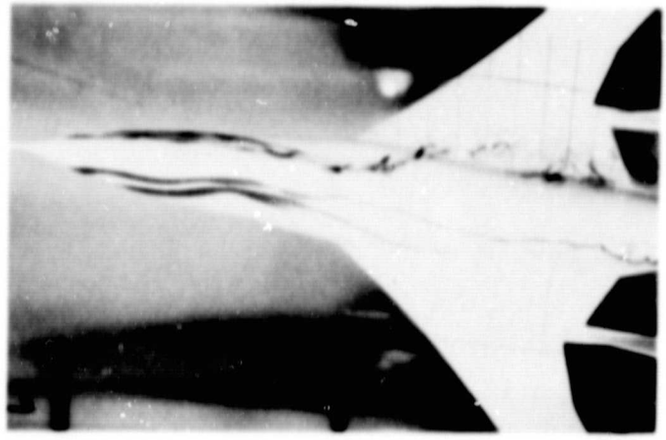

$\alpha = 20^{\circ}$

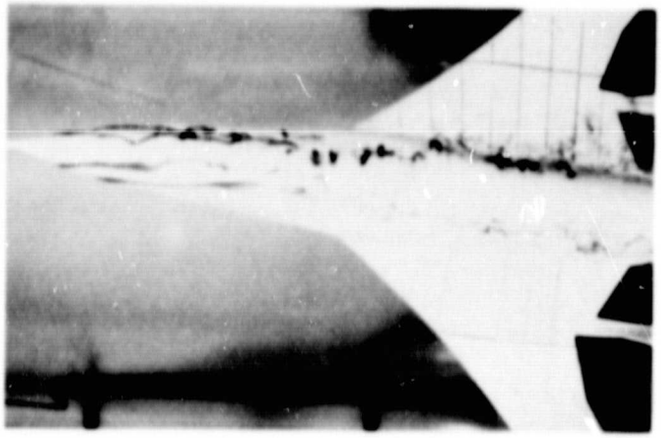

$\alpha = 25^{\circ}$

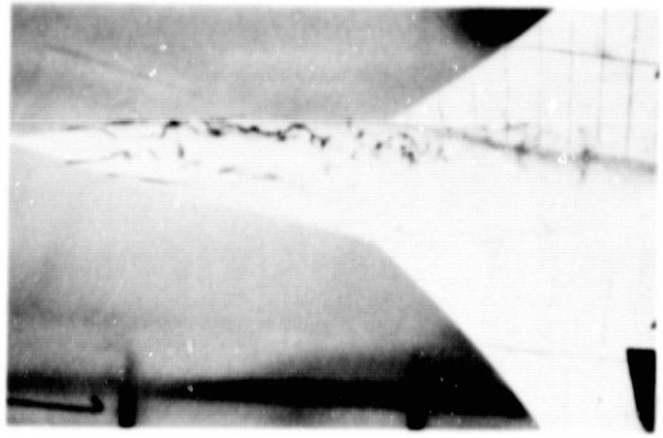

$\alpha = 30^{\circ}$

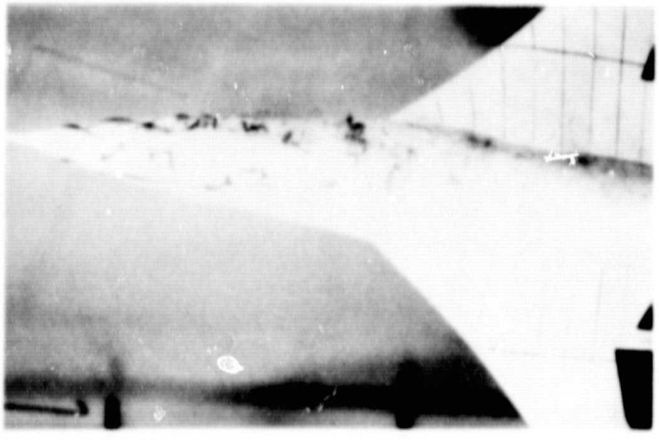

$\alpha = 35^{\circ}$

(A) PLAN VIEW

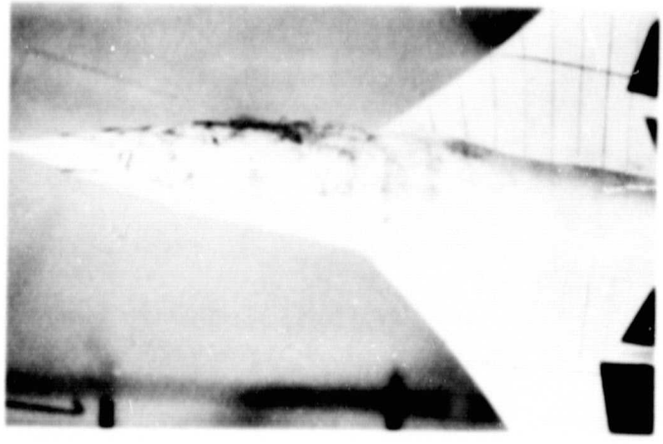

$\alpha = 40^{\circ}$

FIGURE 27. FOREBODY FLOW FIELD WITHOUT CANARD FOR $\beta = 5^{\circ}$

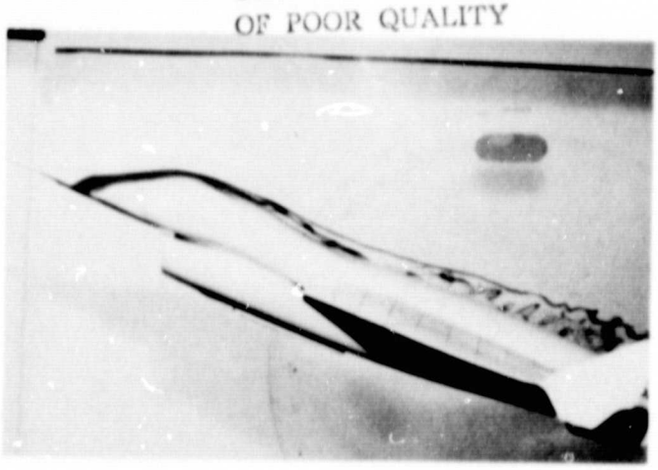

$\alpha = 18^{\circ}$

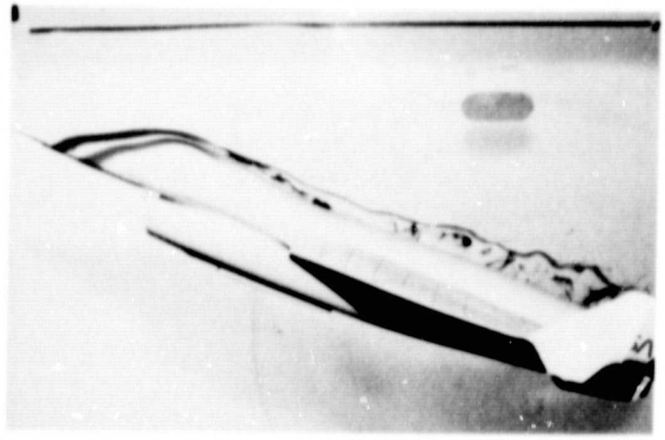

$\alpha = 20^{\circ}$

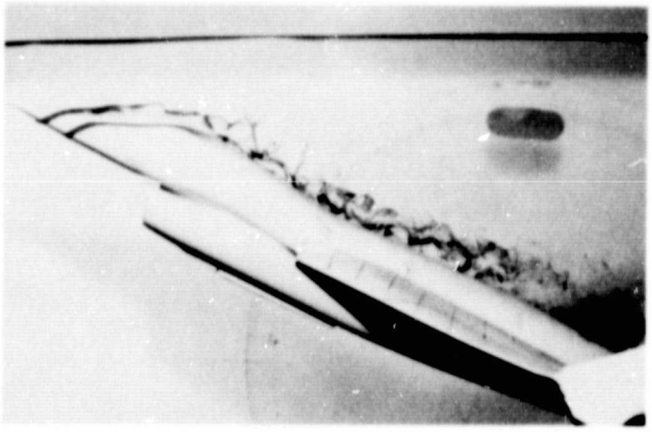

$\alpha = 25^{\circ}$

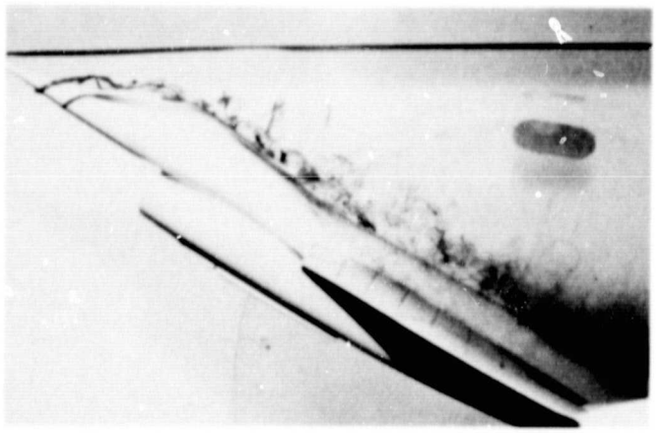

$\alpha = 30^{\circ}$

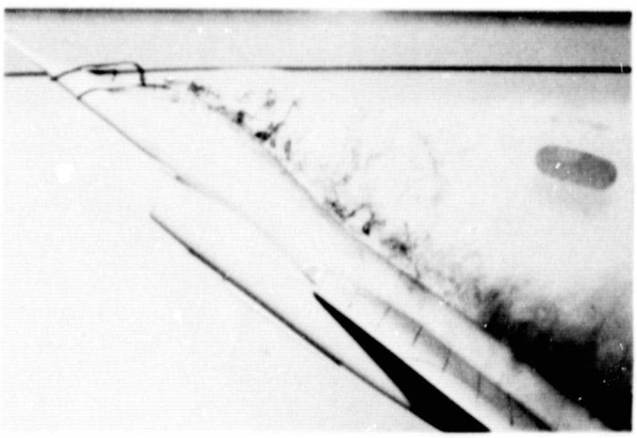

$\alpha = 35^{\circ}$

$\alpha = 40^{\circ}$

(B) WINDWARD PROFILE VIEW

FIGURE 27. CONCLUDED

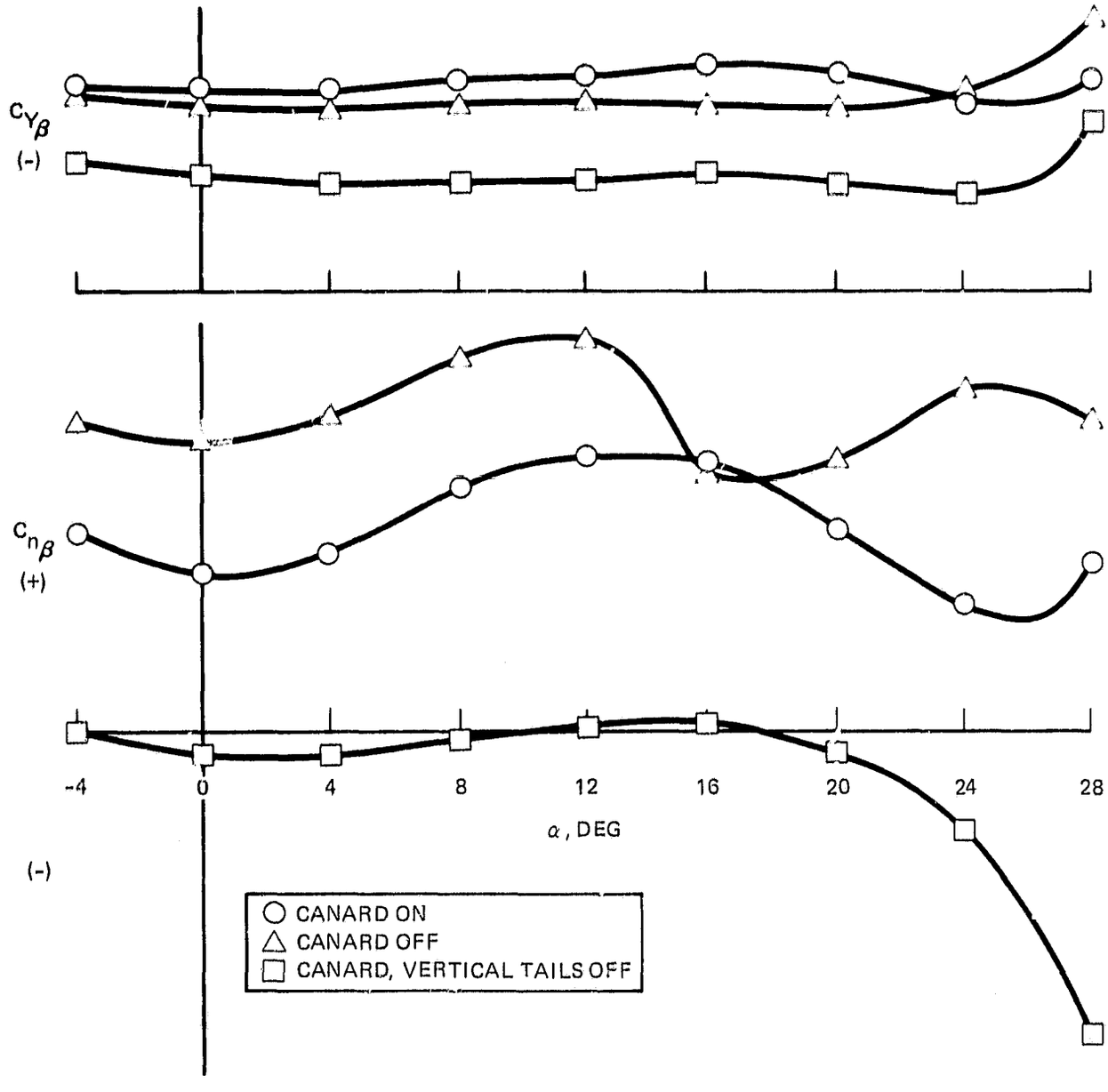

FIGURE 28. DIRECTIONAL STABILITY CHARACTERISTICS OF THE HIMAT

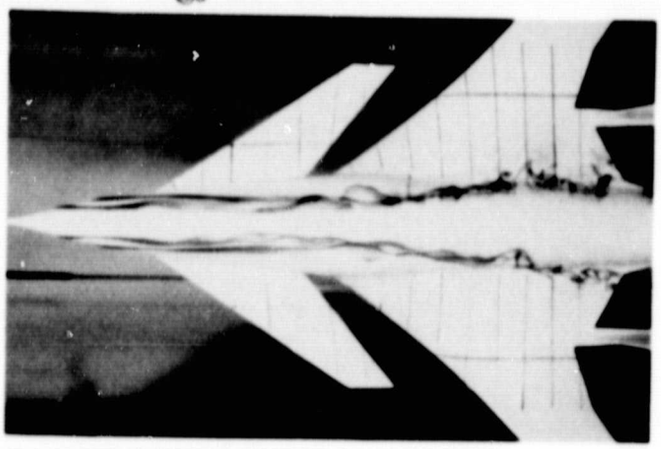

$\alpha = 20^{o}$

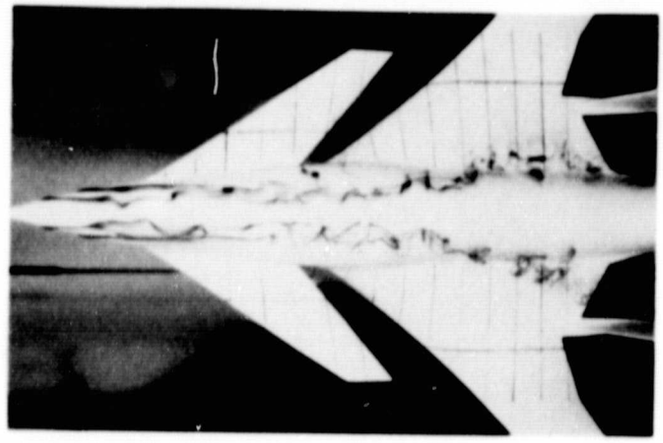

$\alpha = 25^{o}$

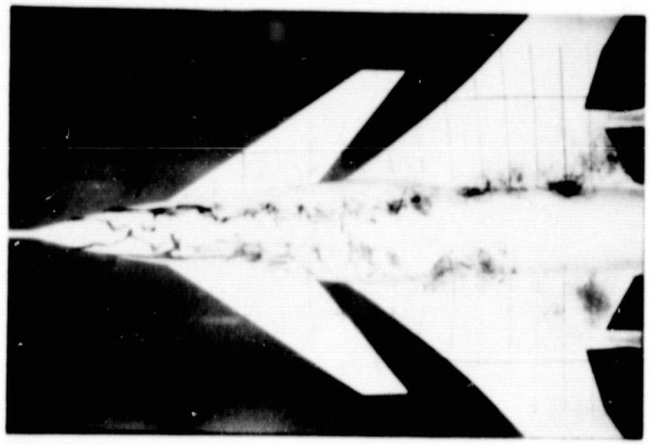

$\alpha = 28^{o}$

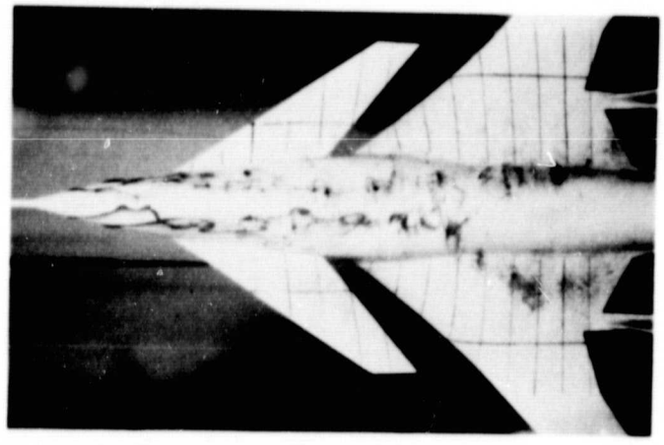

$\alpha = 30^{o}$

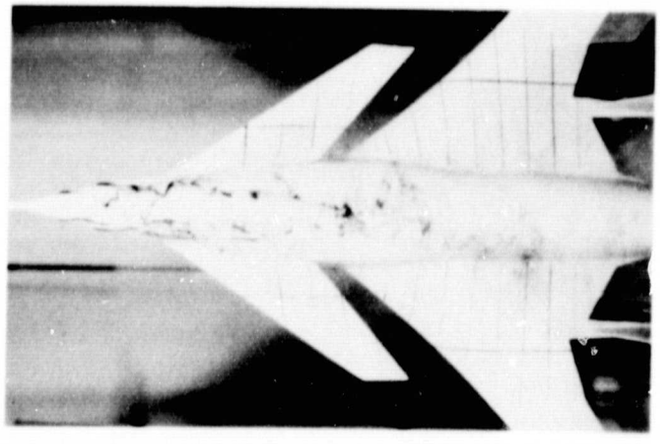

$\alpha = 35^{o}$

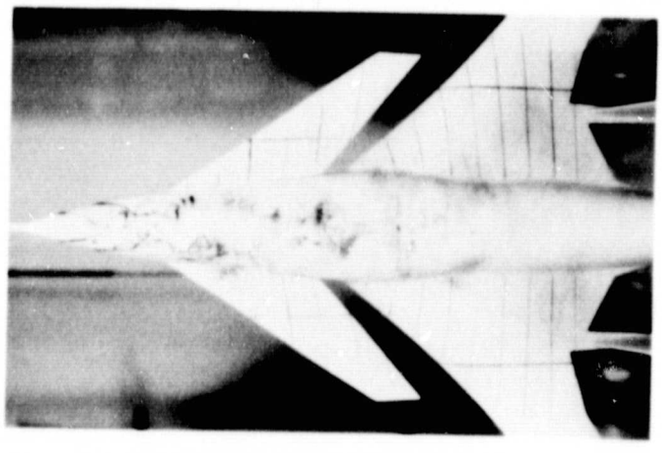

$\alpha = 40^{o}$

FIGURE 29. FOREBODY FLOW FIELD FOR $\dot{m}_I = 0$, $\beta = 0^{o}$

1. Report No.	2. Government Accession No.	3. Recipient's Catalog No.
NASA CR-163094		

4. Title and Subtitle	5. Report Date
FLOW VISUALIZATION STUDY OF THE HiMAT RPRV	July 1980
	6. Performing Organization Code
7. Author(s)	8. Performing Organization Report No.
Dale J. Lorincz	NOR 80-128
	10. Work Unit No.
9. Performing Organization Name and Address	
Northrop Corporation Aircraft Division 3901 West Broadway Hawthorne, California 90250	11. Contract or Grant No. NAS4-2616
	13. Type of Report and Period Covered
12. Sponsoring Agency Name and Address	Contractor Report-Topical
NASA Dryden Flight Research Center Edwards, California 93523	14. Sponsoring Agency Code H-1121

15. Supplementary Notes

NASA Technical Monitor: Edward L. Friend, Dryden Flight Research Center

16. Abstract

Water tunnel studies have been performed to qualitatively define the flow field of the highly maneuverable aircraft technology remotely piloted research vehicle (HiMAT RPRV). Particular emphasis was placed on defining the vortex flows generated at high angles of attack. The flow visualization tests were conducted in the Northrop water tunnel using a 1/15-scale model of the HiMAT RPRV. Flow visualization photographs were obtained for angles of attack up to 40° and sideslip angles up to 5°.

The HiMAT model was investigated in detail to determine the canard and wing vortex flow field development, vortex paths, and vortex breakdown characteristics as a function of angle of attack and sideslip. The presence of the canard caused the wing vortex to form further outboard and delayed the breakdown of the wing vortex to higher angles of attack. An increase in leading-edge camber of the maneuver configuration delayed both the formation and the breakdown of the wing and canard vortices. Additional tests showed that the canard vortex was sensitive to variations in inlet mass flow ratio and canard flap deflection angle.

Asymmetries in the vortex system generated by the forebody were observed in the water tunnel at zero sideslip and high angles of attack. The orientation of the forebody vortex system in sideslip was found to influence the directional stability of the HiMAT at the higher angles of attack. A nose boom was added to the forebody and was seen to shed a turbulent wake which disrupted the forebody vortex pair.

17. Key Words (Suggested by Author(s))	18. Distribution Statement
Canard-wing interference High angle of attack aerodynamics Lateral/directional stability Vortex flow fields	Unclassified - Unlimited STAR Category: 02

19. Security Classif. (of this report)	20. Security Classif. (of this page)	21. No. of Pages	22. Price*
Unclassified	Unclassified	69	

* For sale by the National Technical Information Service, Springfield, Virginia 22161